Politecnico di Milano
Dipartimento di Fisica

Exploring Light Harvesting Systems via Broadband Transient Photoluminescence Spectroscopy

Inorganic, Organic and Biological Perspectives

Doctoral Dissertation of:
Marcelo J. P. Alcocer

Supervisor:
Dr. Annamaria Petrozza

Tutor:
Prof. Guglielmo Lanzani

Doctoral Program Chair:
Prof. Paola Taroni

Doctoral Program in Physics
2014 – XXVI Cycle

EXPLORING LIGHT HARVESTING SYSTEMS VIA BROADBAND TRANSIENT PHOTOLUMINESCENCE SPECTROSCOPY

Marcelo J. P. Alcocer

Dipartimento di Fisica
Politecnico di Milano

Supervisor: Dr. Annamaria Petrozza

This thesis deals with the design, development and application of the ps-resolution broadband transient photoluminescence system at the Center for Nano Science & Technology in Milan. It describes the work performed predominantly by Marcelo J. P. Alcocer in the period 2011–2013 for attainment of his Ph.D.

The design, development and characterisation of the ps-resolution broadband transient photoluminescence system is presented. The system is shown to have almost unbroken spectral coverage in excitation from 280 nm to 1400 nm through the use of a commercial Ti:Al_2O_3 oscillator, second and third harmonic systems, and a custom-built frequency doubled optical parametric oscillator. Acousto-optical modulation permits excitation rates from 80 MHz to tens of kHz, whilst a custom-built confocal microscope allows three-dimensionally spatially resolved measurements to be performed down to a few microns. Separate streak camera and time correlated single photon counting detection systems are employed so as to provide unbroken coverage in the 300 nm to 1400 nm range, with a maximum system temporal resolution of ~1.9 ps for streak based measurements in the visible spectral region. A custom-built open source cross-platform software suite (`trpl`) for data visualisation and post-processing is also introduced.

Subsequently, in-depth investigations into the photo-physics of Rubrene (5,6,11,12-tetraphenyltetracene) single molecular crystals are presented.

The origin of previously observed spurious low-energy emission is shown to arise from an emissive state which is populated from the higher lying first singlet state. This low-energy state has a strong optical coupling to the ground state but exhibits remarkably weak absorption. Nevertheless, direct population from the ground state is demonstrated, thereby ruling out previous attribution to transient excited state species. It is speculated that the low-energy state originates from a low-density crystalline Rubrene-peroxide layer.

Investigations into the nature of the long-lived photogenerated species observed in Rubrene are also presented. Transient absorption and photoluminescence measurements are used to show that long-lived spectroscopic features previously attributed to triplet excitons arise in fact from polaron states. This finding undermines all previous direct spectroscopic observations of triplet excitons in Rubrene crystals, and so calls into question the significance and/or presence of the purported singlet fission and triplet fusion processes in Rubrene single crystals.

Finally, three case-studies are presented demonstrating the application of the developed transient photoluminescence system to investigations of a disparate array of material systems.

Firstly, the workings of a novel ‘dye-doped’ photovoltaic device architecture are elucidated through high temporal resolution transient photoluminescence measurements. A key energy transfer process from light harvesting antenna molecules (Spiro-TBT) to a co-polymer donor (PCPDTBT) is directly observed, and is subsequently shown to significantly improve device performance through spectral broadening.

Secondly, an investigation into the photo-protection mechanisms regulating photosynthesis in higher plants is presented. In this case, global analysis of bi-dimensional high temporal resolution photoluminescence data allows a new non-photochemical quenching mechanism to be identified. This mechanism is shown to take place in the photosystem I super-complex and be mediated by the light-induced accumulation of the xanthophyll zeaxanthin. Most interestingly, it is demonstrated that energy dissipation does not occur in the isolated light harvesting photosystem sub-units as expected, but rather only when they are bound to the corresponding photosystem core complex. This is markedly different to the situation in the better studied photosystem II counterparts.

Thirdly, two brief investigations into the promising new cation exchange route for nanocrystal synthesis are presented. Transient photoluminescence is used to confirm the successful completion of full cation exchange from CdSe/CdS dot/rod nanocrystals into corresponding ZnSe/ZnS nanocrystals. This opens the possibility of uniting the best of both material systems by projecting the good structural qualities of the Cd-based system onto less toxic Zn-based systems. Spectroscopic evidence for partial cation exchange from Cu deficient Cu-In-S nanocrystals to quaternary Cu-In-Zn-S nanocrystals is also presented, showing the potential of this approach for fine stoichiometric tuning of this up-and-coming material system.

"I often imagine meeting a great person from centuries past and explaining modern science. It would be such a thrill to see the face of Galileo or Newton or Faraday or Mendeleev or Curie or Darwin or Archimedes as they learned what we know now.

But then I remember that no one has yet lived long past a century. All those people are dead. Unrecoverable. Beyond the reach of technology, no matter its sophistication.

But you my little one. You are no different from the first human. You aren't 200 *or* 2000 *years old. You are* 200 000 *years old.*

And I will show you everything."

Zach Weinersmith

For MJEA

Ringraziamenti

One thing I haven't learned during the course of my Ph.D. is how to answer the question "Where are you from?" with any degree of certainty or aplomb. Nevertheless, the unquantifiabe British part of me feels the need to begin this section with an apology; to all those who have had to put up with my grumpy, sceptical, stubborn, arrogant, perfectionist, beardy, forgetful, sleep deprived, binary, nerdy self over these last three years, I am truly sorry. It is only because of your patience and tolerance however that any of the work described in these pages was accomplished.

Whilst an exhaustive list of acknowledgements would be exhausting if not impossible to compile, I must surely start by thanking my supervisor, mentor and friend Anna. Thank you for offering me the opportunity to become a 'Petrozzcopist' in the first place, for putting me up at your place whilst I had a look around, for helping me to settle in, for frequently feeding me, for bringing me back porridge from the UK. . . the list goes on. On a more serious note, thank you for your faith in my capabilities and your trust in giving me relative freedom during these last three years. It has been a truly wonderful experience to be able to follow my curiosity once again and learn an innumerable number of things in doing so. I feel I have gained an enormous amount of scientific insight from your diligent supervision and guidance.

There are of course always two parent figures in any relationship, and I don't think I would have survived the emotional trauma of a Ph.D without the continued support and friendship of Egregio Prof. D'Andrea. Thank you Cosimo for your patience in listening to my constant worries over ceaseless gallons of coffee and ice-cream. Thank you too for not only teaching me Italian (sorry again for the ear-scarring first few months) but also all the skills necessary to build a fully functional TPL system without blinding myself. In many ways, it feels fraudulent to describe any of the work on the TPL system as my own given the significant master-plans you essentially handed me.

Thanks are also of course also due to Guglielmo, for establishing a research centre (not center) of international standing which nevertheless has an incredibly relaxed and friendly atmosphere. I am convinced that this open approach fosters more creativity, knowledge-transfer and interdisciplinary research than any number of prescriptive courses or seminars could ever hope to. I think it's fair to say that I was totally unaware of just how much you can learn on a coffee break in Italy. . .

I am hugely grateful to all members of the HIPOP group, both past a present, for their experimental and emotional support over the course of these years. Spending endless days in search of non-existent signal in a blacked out, aggressively air-conditioned lab should not have been in any way enjoyable, and yet you have shown that exceptional company triumphs in the face of adversity. Ajay, thank you for your immeasurable help, wisdom and above all company in the lab. The list of our discussions spanning the finer points of scientific theories, pitfalls and politics of working in academia, publishing practices and Indian culture would certainly fill many books. Thank you also for all your experimental help in performing the infinite permutations of pump-probe measurements I asked of you. I learned a lot from our shared time in the lab, not least that lasers are never stable. . . Vincenzo, you should win a medal for putting up with my arrogant scepticism (sceptical hippo will always be sceptical) and my pernickity* nature. Whilst I would never say it, I am secretly very glad that it is you who will be keeping a close eye on my lab-based baby in the years to come. You'll be grand. Giulia, I apologise if I have ever been terse with you, but if so it is only because I cannot compete with your boundless enthusiasm for research. It has been a delight to work alongside someone so motivated, experienced and yet, somehow, still optimistic. You provided the perfect antidote to my emanating grump. Simo — a man of few words; thanks!

On a more professional side, I would like to thank Adele Sassella and Marcello Campione at Università degli Studi Milano Bicocca for supplying the Rubrene single crystals and for many fruitful discussions. Similarly, many thanks to Robert Bassi's group at Università di Verona for the photosystem samples, and especially to Matteo Ballottari for his frequent all-day trips to Milan and incredible patience in teaching ignorant physicists plant biology. I am also very grateful to i Franceschi and Liberato Manna's group at the IIT for the chance to revisit my old nanocrystal stomping grounds. Ahh the memories. . .

I am indebted to a multitude of people at the Dipartimento di Fisica at the PoliMi, but special mentions go to Giulio and Dario for coordinating the interactions with Verona and giving me the opportunity to get involved in the fascinating world of photosynthesis. Further thanks to Giulio and Francesco for all their expertise and time in developing the OPO, Alessia for her work on the THG system, Daniele for the global analysis of the photosystem data, and Papa Francesco 'Scot'

---

[*] Look it up

Scotognella (and PRIN) for agreeing to fund me for the next eighteen months!

There is of course one glaring omission in these acknowledgements, and that is to my wife Eline. My dear, there is nothing I could possibly write on this page which would come close to expressing my gratitude for accompanying me on this ridiculous journey. I'm sorry for the many tough times and simply look forward to being back at your side. I hope this is the best thanks I can give.

MA

Contents

Contents i

List of Figures v

List of Tables vii

List of Abbreviations x

Preface 1

1 Design & Development of ps-Resolution Broadband Transient Photoluminescence System 3

- 1.1 Background 4
  - 1.1.1 Transient Emission Spectroscopy 4
  - 1.1.2 Transient Absorption Spectroscopy 8
  - 1.1.3 Nonlinear Optics for Transient Spectroscopies 13
    - 1.1.3.1 Nonlinear Optical Media 14
    - 1.1.3.2 Second Harmonic Generation 15
    - 1.1.3.3 Sum Frequency Generation 16
    - 1.1.3.4 Difference Frequency Generation 17
    - 1.1.3.5 Optical Parametric Oscillators 18
    - 1.1.3.6 Birefringent Phase Matching 19
    - 1.1.3.7 Quasi-Phase Matching 22
- 1.2 Transient PL System 23
  - 1.2.1 Motivation & Specification 23
  - 1.2.2 System Description 24
    - 1.2.2.1 Oscillator 24
    - 1.2.2.2 Excitation Repetition Rate Selection 26
    - 1.2.2.3 Excitation Wavelength Selection 27
    - 1.2.2.4 Spatial Resolution 29
    - 1.2.2.5 Detection Systems 30
    - 1.2.2.6 Data Post-processing 32
- 1.3 Transient Absorption Systems 34

1.3.1 fs-Resolution TA System Description 34
1.3.2 ns-Resolution TA System Description 35
References 36

2 Transient Spectroscopic Investigations of Rubrene Single Crystals 39
2.1 Background 40
2.1.1 Molecules 40
2.1.1.1 Conjugated Molecules 40
2.1.1.2 Electronic Structure of Molecules 41
2.1.1.3 Optical Transitions 44
2.1.1.4 Neutral Excited States 46
2.1.1.5 Charged Excited States 49
2.1.2 Molecular Crystals 49
2.1.2.1 Electronic Structure of Dimers 50
2.1.2.2 Electronic Structure of Linear Molecular Crystals 52
2.1.2.3 Electronic Structure of Real Molecular Crystals . 53
2.1.3 Singlet Fission & Triplet Fusion 54
2.1.4 Properties of Rubrene 56
2.1.4.1 Molecular Rubrene 56
2.1.4.2 Crystalline Rubrene 56
2.2 Transient Spectroscopic Investigations of Rubrene Single Crystals 58
2.2.1 Low Energy Photoluminescence 58
2.2.1.1 Experimental Results 59
2.2.1.2 Conclusions 62
2.2.2 Long-lived Photo-generated Carrier Dynamics 62
2.2.2.1 Experimental Results 63
2.2.2.2 Conclusions 68
References 68

3 Broadband Transient Photoluminescence Case Studies 73
3.1 Panchromatic Dye-Doped Polymer Solar Cells 73
3.1.1 Background 73
3.1.2 Experimental Results 75
3.1.3 Conclusions 78
3.2 Regulation of Photosystem I Light Harvesting by Zeaxanthin . . . 78
3.2.1 Background 78
3.2.1.1 Light Dependent Reactions of Photosynthesis . . 79
3.2.1.2 Higher Plant Photosystems 80
3.2.1.3 Non-Photochemical Quenching 82
3.2.2 Experimental Results 82
3.2.3 Conclusions 85

3.3 Cation Exchange in Inorganic Nanocrystals 85
3.3.1 Background 85
3.3.2 Experimental Results 88
3.3.2.1 Blue-UV-Emitting ZnSe(Dot)/ZnS(Rod) Core/Shell Nanocrystals Prepared from CdSe/CdS Nanocrystals by Sequential Cation Exchange 88
3.3.2.2 Strongly Fluorescent Quaternary CuInZnS Nanocrystals Prepared from $Cu_{1-x}InS_2$ Nanocrystals by Partial Cation Exchange 90
3.3.3 Conclusions 91
References 92

Conclusions **97**
References 99

Appendix I — Dissemination **I**

Appendix II — Pulse Parameter Reference **III**

List of Figures

1.1 Einstein model . . . 3
1.2 Typical TPL map . . . 5
1.3 Three level TA model . . . 10
1.4 Typical TA map . . . 11
1.5 OPO spectral mode structure . . . 20
1.6 TPL system optical layout . . . 25
1.7 Ti:Al_2O_3 oscillator power characteristics . . . 26
1.8 Excitation spectrum coverage . . . 27
1.9 SHG and THG tuning plots . . . 28
1.10 OPO tuning plots . . . 29
1.11 Streak voltage sweeps . . . 32
1.12 Streak camera characterisation . . . 33
1.13 fs-TA system optical layout . . . 35
1.14 ns-TA system optical layout . . . 36

2.1 Conjugated molecular structure . . . 41
2.2 Optical transitions in molecules . . . 46
2.3 Molecular ionisation potentials . . . 50
2.4 Electronic structure of organic molecular crystals . . . 52
2.5 Rubrene molecular and crystalline structure . . . 57
2.6 Rubrene CW absorption and PL . . . 58
2.7 Rubrene TPL at 77 K under excitation of S_1 . . . 59
2.8 Rubrene TPL temperature dependence under excitation of S_1 . . . 60
2.9 Rubrene TPL excitation energy dependence at 77 K . . . 61
2.10 Rubrene TPL at 295 K under excitation of S_1 . . . 63
2.11 Rubrene TPL excitation fluence dependence at 295 K under excitation of S_1 . . . 64
2.12 Rubrene TA at 295 K under excitation of S_1 . . . 65
2.13 Rubrene TA spectrum comparison . . . 66
2.14 Rubrene TA at 295 K under excitation of B . . . 67

3.1 Dye-doped polymer cell model . . . 75

3.2 Dye-doped polymer cell CW absorption and emission spectra . . . 76
3.3 Dye-doped polymer cell TPL 76
3.4 Dye-doped polymer cell TA and EQE 77
3.5 Higher plant thylakoid location and structure 80
3.6 Photosystem I structure 81
3.7 Xanthophyll cycle 81
3.8 Photosystem I reaction centre CW photo-bleach 83
3.9 Photosystem I TPL decay associated spectra 84
3.10 Nanocrystal quantum confinement 87
3.11 CdSe/CdS and ZnSe/ZnS nanocrystal TPL 89
3.12 CIS and CIZS nanocrystal TPL 90

List of Tables

1.1 Birefringent phase matching conditions 21

2.1 Exciton wavefunctions 48

3.1 Photosystem I TPL decay associated spectra assignment 85
3.2 CdSe/CdS and ZnSe/ZnS nanocrystal TPL decay parameters . . 88
3.3 CIS and CIZS nanocrystal TPL decay parameters 91

List of Abbreviations

AOM	Acousto-Optical Modulator	26
ATP	Adenosine Triphosphate	73
BBO	β Barium Borate (β-BaB_2O_4)	15
BHJ	Bulk Heterojunction	67
BOA	Born-Oppenheimer Approximation	40
CCD	Charge Coupled Detector	8
CE	Cation Exchange	81
Chl	Chlorophyll	74
CIS	Copper-Indium-Sulphide	82
CIZS	Copper-Indium-Zinc-Sulphide	82
CMS	Charge Modulation Spectroscopy	63
CNST	Center for Nano Science and Technology	4
CW	Continuous Wave	3
DAS	Decay Associated Spectra	77
DFG	Difference Frequency Generation	15
EM	Electromagnetic	14
FC	Franck-Condon	43
FET	Field Effect Transistor	60
FOV	Field of View	30
FRET	Förster Resonant Energy Transfer	68
FWHM	Full Width Half Maximum	24
HOMO	Highest Occupied Molecular Orbital	39
ISC	Intersystem Crossing	46
LHC	Light Harvesting Complex	74
LUMO	Lowest Unoccupied Molecular Orbital	39
NADPH	Nicotinamide Adenine Dinucleotide Phosphate	73
NC	Nanocrystal	80
NPQ	Non-Photochemical Quenching	76
OPA	Optical Parametric Amplifier	18
OPO	Optical Parametric Oscillator	18
PA	Photo-induced Absorption	9
PB	Photo-induced Bleach	9
PL	Photoluminescence	4

PLQY	Photoluminescence Quantum Yield	81
PPLN	Periodically Poled Lithium Niobate (PP-$LiNiO_3$)	28
PSI	Photosystem I	73
PSII	Photosystem II	73
PV	Photovoltaic	37
PVT	Physical Vapour Transport	54
QTH	Quartz-Tungsten-Halogen	12
REDOX	Reduction-Oxidation	73
SE	Stimulated Emission	9
SF	Singlet Fission	52
SFG	Sum Frequency Generation	15
SHG	Second Harmonic Generation	15
SO	Spin-Orbit	46
TA	Transient Absorption	4
TCSPC	Time Correlated Single Photon Counting	7
TF	Triplet Fusion	54
THG	Third Harmonic Generation	27
TPL	Transient Photoluminescence	4
WT	Wild Type	77

Preface

Whilst perhaps not immediately apparent, the interactions between light and matter are fundamental to our everyday lives. From underpinning the optical fibre technology at the heart of our modern global communication networks, to being one of the few tools available to astronomers and cosmologists with which to study the workings of the universe. More pertinently, light-matter interactions also afford a means of harnessing the vast quantities of solar energy bathing our planet and form the basis of the photosynthetic processes which provide almost the energy for life on earth. Viewed through a modern anthropocentric lens, a precise understanding of these interactions may also allow us to solve the enormous challenge of meeting the increasing energy demands of an exponentially growing population in a sustainable way.

Knowledge of the dynamics — i.e. the evolution in time — of light-matter interactions allows the flow of energy in optical systems to be tracked. A good understanding of these dynamics is therefore essential in order to develop novel and more efficient optical systems such as photovoltaic devices, light sources, etc. Many of the key processes governing such interactions take place at very short timescales (fs to ns) and so can only be truly investigated via ultra-fast transient spectroscopic techniques. This text deals with the development of one such experimental transient spectroscopic system and its subsequent application to the investigation of the photo-physics of a variety of light harvesting systems.

Chapter 1 deals with the design and development of a broadband ps-resolution transient photoluminescence system at the Center for Nano Science & Technology. A brief introduction to modern optical transient spectroscopic techniques and the associated non-linear optics they depend on is given. The motivation for the construction of such a transient photoluminescence system is then presented, followed by a detailed description of the system proper. For the sake of completeness, further brief descriptions are given of other transient spectroscopic systems utilised in the investigations which follow.

In Chapter 2, an in-depth investigation is presented into the photo-physics of one particular material system using the transient spectroscopic techniques outlined in Chapter 1. The material in question is the monocrystalline phase of the conjugated organic molecule 5,6,11,12-tetraphenyltetracene — more commonly known as Rubrene. An introduction to the key concepts and theories of the optoelectronic properties of conjugated molecules and molecular crystals is given. This is followed by a brief review of the current understanding of Rubrene photo-physics, including areas where consensus is lacking. Two investigations are subsequently described which deal with the origin of a spurious low-energy emission band and the nature of long-lived photogenerated carriers in Rubrene crystals. In each case, new experimental results and insights are presented and discussed.

Finally, Chapter 3 details three case-studies demonstrating the application of the developed transient photoluminescence system to investigations of a disparate array of material systems. Focus is given to the role of the transient spectroscopic system within the investigations, and the particular specifications which permit such experiments to be performed. Firstly, the workings of a new photovoltaic device architecture is elucidated using transient photoluminescence measurements. More specifically, the key energy transfer process responsible for improved device operation is directly observed and monitored using the high temporal resolution of the spectroscopic system. Secondly, an investigation into the photo-protection mechanisms which regulate photosynthesis in higher plants is presented. In this case, global analysis of bi-dimensional high temporal resolution photoluminescence data allows a new non-photochemical quenching mechanism to be identified. Finally, the use of transient photoluminescence as a tool for material characterisation in nanocrystal systems is described. Time-resolved nanocrystal emission is used confirm the successful completion of a promising new route for non-toxic nanocrystal synthesis.

All the work described herein was performed between 2011 and 213 as a joint collaboration between the Center for Nano Science & Technology and the Physics Department of the Politecnico di Milano with predominant contribution from the author unless otherwise stated.

Marcelo J. P. Alcocer
January 2014

Chapter 1

Design & Development of ps-Resolution Broadband Transient Photoluminescence System

The diverse field of spectroscopy can be most concisely and generally surmised as the study of the interaction of matter with radiated energy. Its theoretical framework is therefore based on the three fundamental interactions of light and matter as described by Einstein, viz. stimulated absorption*, stimulated emission, and spontaneous emission

Whilst steady-state spectroscopies — also referred to as continuous wave (CW) spectroscopies — only resolve these interactions based on the energy of the transitions (spectral resolution), transient spectroscopies also resolve in time and are

---

*This will hereafter simply be referred to as absorption

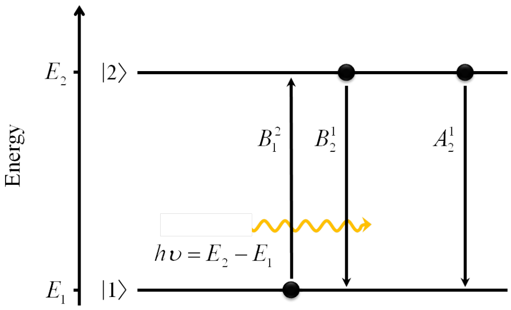

Figure 1.1: Einstein model of light matter interaction showing (stimulated) absorption, stimulated emission and spontaneous emission transitions and their coefficients B_1^2, B_2^1 and A_2^1 respectively.

therefore also known as time-resolved spectroscopies. Their usefulness is derived from the fact that the measured quantity can often be directly related to population of a photo-active species, allowing non-equilibrium population dynamics to be monitored. The most widespread of these transient techniques are transient emission and transient absorption spectroscopies, where the measured interactions are spontaneous emission and induced absorption/emission respectively. Both of these techniques were used extensively in the work presented herein and required the design, construction and development of experimental systems.

In this chapter, the design and development of the transient emission system at the Center for Nano Science and Technology (CNST) is described. The transient absorption (TA) systems were principally developed by others (Srimath Kandada, Raavi, Grancini, Petrozza, Polli, Cerullo, Lanzani) and so shall only be briefly discussed.

1.1 Background

By way of introduction and background to the developmental work performed, a brief recap of transient spectroscopic techniques and related optics is presented in this section. This is by no means comprehensive or mathematically rigorous. Interested readers are instead referred to the excellent texts in references 1–7.

1.1.1 Transient Emission Spectroscopy

Transient emission spectroscopy concerns the measurement of the spontaneous transitions (i.e. emission) of non-equilibrium populations. The phenomenon of spontaneous emission is typically dominant around the visible region of the electromagnetic spectrum [2] where it is often termed luminescence[*] (from the Latin, *lumen*=light) and can be categorised by excitation source.

Despite the multitude of different excitation sources available, photoluminescence (PL) is the overwhelmingly dominant form of luminescence spectroscopy due to the experimental simplicity and technological maturity of light sources. Transient PL (TPL) spectroscopy can therefore be defined most generally as the temporal resolution of the visible and near-visible spontaneous emission of a sample excited through the absorption of light. Given the simplicity of spectral resolution in the (near-)visible regime — a diffraction grating is often the only requirement — practical TPL systems often combine both spectral and temporal resolution. Therefore, the resulting measured quantity in most TPL systems is the PL intensity as a function of wavelength and time after excitation.

---

[*] This terminology is used to distinguish between emission arising from electronic and thermal excitation, the latter being termed incandescence and arising from the radiative redistribution of entropy at elevated temperatures

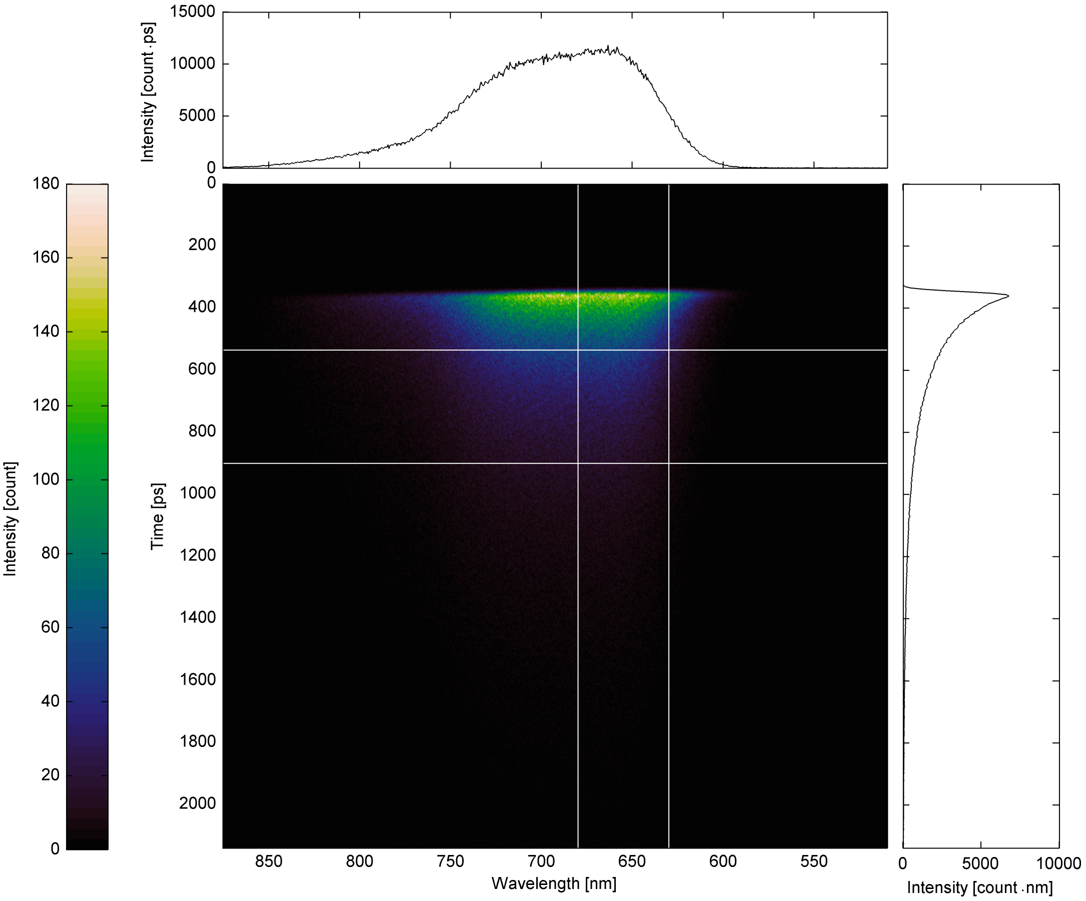

Figure 1.2: Typical TPL map showing temporally and spectrally resolved PL intensity. Profiles corresponding to integrated spectra (upper panel) and dynamics (right panel) within the depicted limits are also shown.

As alluded to previously, the defining utility of TPL spectroscopy is the ability to link the measured quantity to non-equilibrium state populations. Time-resolved PL intensity is simply a measure of the number of photons emitted via spontaneous emission at a certain time after excitation. Spontaneous emission is an inherently stochastic process, with individual chromophores remaining in the excited state for a certain amount of time after excitation before emitting a photon. The time spent in the excited state for any given chromophore is randomly distributed over a well defined temporal probability distribution. Time-resolved observation of photon emission from an ensemble of excited chromophores therefore yields a measure of this distribution. Whilst the actual process of photon emission is extremely fast (sub-fs timescale), the probability distribution typically spans much longer intervals (fs–µs). In 1917, Einstein formulated these concepts mathematically through the introduction of A and B coefficients describing the basic light-matter interactions [8] (Figure 1.1). For a single ideal two level system in the excited state, the probability, dW, of de-excitation in a time interval dt via spontaneous photon emission is governed by the A_2^1 coefficient,

$$dW = A_2^1 dt \; . \tag{1.1}$$

In an ensemble of such identical systems with a total excited state population n, the photon emission probability distribution is therefore given by

$$\begin{aligned} dW &= \sum_{i=1}^{n} A_2^1 dt \qquad (1.2)\\ &= A_2^1 n dt \; . \qquad (1.3) \end{aligned}$$

Given that de-excitation necessarily implies excited state depopulation, the probability is trivially related to the excited state population by $dn = -dW$, and so the evolution of the ensemble excited state population — and therefore PL intensity — can be described by

$$dn = -A_2^1 n dt \; . \tag{1.4}$$

In the absence of further decay channels (which can be described via additional decay coefficients), the excited state population and PL dynamics therefore follow a simple mono-exponential form,

$$n(t) = n(0) e^{-A_2^1 t} \; . \tag{1.5}$$

Transient PL measurements are typically performed in the time domain by exciting the sample using a short pulse of light and measuring the subsequent spontaneous emission as a function of time after excitation using a suitable detection system. Regardless of the detection system, the measured quantity will be at least a convolution of the temporal profiles of the excitation pulse and true sample emission. Deconvolution is therefore necessary to recover the true emission profile. For this reason, extremely short excitation pulses are desirable in transient spectroscopies so as to limit the need for deconvolution. This has led to a rich overlap between the fields of spectroscopy and laser physics, with the advances and demands of one field fuelling the other.

The spectral content of the excitation source must also be carefully controlled so as to match the absorption bands of the sample. Short-pulse sources are also useful in this respect as their elevated instantaneous powers can induce non-linear optical interactions in some materials, allowing for efficient spectral conversion (see § 1.1.3).

A variety of different detection systems are available for the temporal resolution of photoluminescence and broadly fall into two categories; electronic and optical. The temporal resolution of electronic detection systems are limited by the frequency bandwidth of their constituent electronic components, resulting in typical resolutions of ∼100 ps. In contrast, optical detection systems are limited only by the temporal width of optical pulses employed, and so can reach resolutions of <100 fs. Briefly:

Electronic detection

Fast photo-diode and oscilloscope The current/voltage from an illuminated fast photo-diode is measured as a function of time using an oscilloscope.
Typical resolution: ∼1 ns

Time correlated single photon counting (TCSPC) A high gain detector (e.g. photomultiplier tube) is used to detect attenuated sample emission in the single photon regime. The time between the arrival of the excitation pulse — as detected by an external fast photo-diode — and the detection of a single photon is measured electronically through the use of constant fraction discriminating and time to amplitude converting circuits [1]. A histogram of arrival times is built up over the course of multiple single photon detection events. This is directly equivalent to the temporal evolution of the sample PL.
Typical resolution: ∼100 ps

Streak camera Sample emission emission is converted into photo-electrons by a photo-cathode situated in a vacuum tube. The electrons are accelerated along the length of the tube towards a phosphor screen. A time-varying electric field is applied perpendicular to the electron trajectory so as to induce a time-dependent deflection. The deflection is measured by the position of the electron impact on the phosphor screen, yielding temporal to spatial conversion. The resulting cathodoluminescence of the phosphor screen is recorded by a charge coupled detector

(CCD) and imaging system.
Typical resolution: ∼1 ps

Optical detection

Upconversion The output of an ultrafast source, such as a fs laser system, is split into excitation and gate pulses by a thin beam-splitter. The excitation pulse is used to excite the sample, and the resulting PL is spatially and temporally overlapped with the gate pulse within a non-linear medium. Upon fulfilment of suitable phase-matching conditions, a signal at a frequency equal to the sum of gate and PL frequencies is generated (see § 1.1.3). The sum-frequency signal is spectrally selected and detected, yielding a measure of the PL intensity within the temporal window of the gate pulse. Full TPL maps are built up by scanning of the phase matching conditions (spectral scan) and gate-PL temporal overlap (temporal scan).
Typical resolution: ∼100 fs

Whilst time domain measurements are now more commonplace, it should be noted that Fourier relations also permit TPL spectroscopy to be performed in the frequency domain. In these systems, the excitation beam is modulated at varying frequencies and the relative amplitude and phase of the resulting PL is measured. The evolution of the PL in the time domain can subsequently be inferred from these frequency domain parameters. A full description of all the available time and frequency domain TPL detection systems is outside the scope of this text, and interested readers are instead referred to 1–3.

1.1.2 Transient Absorption Spectroscopy

Transient absorption spectroscopy concerns the measurement of the stimulated transitions of non-equilibrium populations. In contrast to TPL where spontaneous transitions are monitored, the detection of stimulated transitions necessarily implies a two field experiment — viz. one involving both an excitation and a stimulating field. These fields are often referred to as pump[*] and probe fields respectively, and so TA techniques are also widely known by the alternative monikers of pump & probe or simply pump-probe techniques. The wavelength of the pump field is typically determined by the ground state absorption band of the sample to be studied whilst the probe wavelength is dictated by the stimulated transitions to be monitored. As such, TA techniques can be categorised according to the spectral regimes of pump and probe fields, with a wide variety of permutations possible — e.g. optical-pump optical-probe, optical-pump IR-probe, optical-pump THz-probe, optical-pump x-ray-probe, UV-pump optical-probe, etc.

---

[*] N.b. The terms pump and excitation field will be used interchangeably in this text

In contrast to TPL, the requirement of a probe field for detection implies that TA measurements are not background free and as such, differential measurements must be performed in order to remove probe field features. The quantity of interest in TA is therefore the relative change in probe signal in the presence and absence of the pump field. This is most simply performed in a transmission geometry where the change in the probe field transmitted through the sample is measured, however alternative geometries — such as reflection — are also trivial.

In order to understand the relevance of the differential signal measured, it is instructive to consider an idealised three level system consisting of a ground state, a first excited state and a higher excited state (Figure 1.3). Within this framework, upon sample excitation two possible stimulated transitions are available from the first excited state; absorption to the higher lying excited state, and stimulated emission back to the ground state. In the former, sample excitation induces a new absorption transition not present in the unexcited sample. Such a transition is therefore termed photo-induced absorption (PA). In the latter case, stimulated emission (SE) occurs back to the ground state in an analogous manner to spontaneous emission, however governed by the Einstein B_2^1 coefficient rather than the A_2^1 coefficient (see Figure 1.1). Further to these excited state transitions, the differential nature of the measurement also results in a signal from the reduction in absorption from the ground state to both excited states due to ground state depopulation. Such a signal is known as a photo-induced bleach (PB). Being differential signals, PB and SE will be of the same sign, whilst PA signals will be of opposing sign. For example, in transmission geometry, PB and SE result in an increase in the amount of probe signal transmitted whilst PA leads to a decrease. As such, the difference in transmitted probe intensity in the presence of the pump radiation compared to in the absence of pump radiation, $T_{\text{pump on}} - T_{\text{pump off}} = \Delta T$, will be positive for PB and SE and negative for PA.

Transient absorption can be therefore be simply defined as the temporal resolution of these differential absorption signals. Its most general definition is perhaps the temporal resolution of the stimulated transitions of non-equilibrium populations. As with spontaneous emission measurements, spectral resolution of the probed transition energies is very straightforward and leads to the formation of differential spectra. The final output of most TA measurements is therefore the differential signal (transmission, reflection, etc.) as a function of wavelength and time.

It should be noted that discrete transition energies are naturally broadened by homogeneous and inhomogeneous effects [6], resulting in the broadening of the differential features into bands. These bands are often broad and can overlap, leading to differential spectra comprised of the superposition of many PA, PB and SE bands. Interpretation of such spectra can therefore be challenging and additional information of the population dynamics — e.g. from TPL measurements — is required in order to gain a physical insight into the behaviour of the

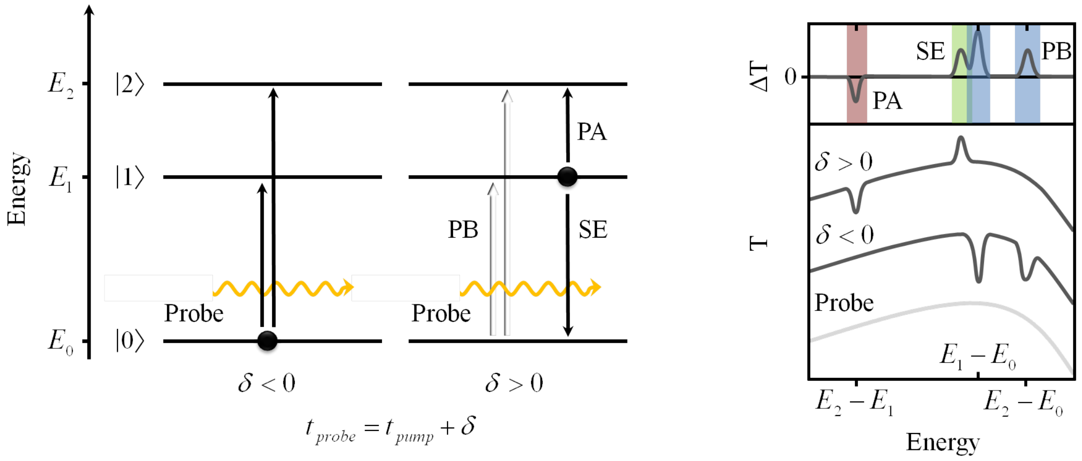

Figure 1.3: *Left panel:* An idealised three-level model system showing probe-induced transitions (black arrows) before and after sample excitation (left and right respectively). The absence of ground state transitions upon sample excitation is also depicted (recessed arrows). *Right panel:* Corresponding transmission (bottom) and differential transmission (top) spectra showing the formation of photo-induced absorption, photo-induced bleach and stimulated emission bands. The probe spectrum is also shown in grey for reference

system. Spectral resolution of both probe and pump energies can also aid interpretation in what is frequently termed bi-dimensional or 2D spectroscopy [9, 10]. This can incur significant increases in experimental complexity however due to the spectrally broad nature of short optical pulses, and as such is a current area of spectroscopic research.

As with TPL, the utility of TA measurements lies in being able to link the measured quantities to state populations. In the context of negligible temporal overlap between pump and probe pulses, a linear formulation based on Beer-Lambert absorption can be adopted*. In such a scenario, transitions between states are modelled as the product of energy dependent absorption cross sections, $\sigma(\lambda)$, representing transitions probabilities, and time dependent concentrations, $n(t)$, representing state populations. Application of the Beer-Lambert law yields and absorbance A, for a sample of thickness L, of

$$A = \sigma(\lambda) n(t) L \; . \tag{1.6}$$

Pump-induced changes in absorbance, $\Delta A = A_{\text{pump on}} - A_{\text{pump off}}$, are therefore

---

*In reality, TA is most fully described by a third order nonlinear interaction between three fields — viz. pump, pump-induced nonlinear sample polarisation and probe [6, 10]. This can lead to a multitude of nonlinear interactions in addition to the linear population interactions described by Einstein. Most of these interactions occur only for the duration of the pump and probe pulse overlap however, and so linear formulations are generally more than adequate for long (>∼100 fs) delay measurements

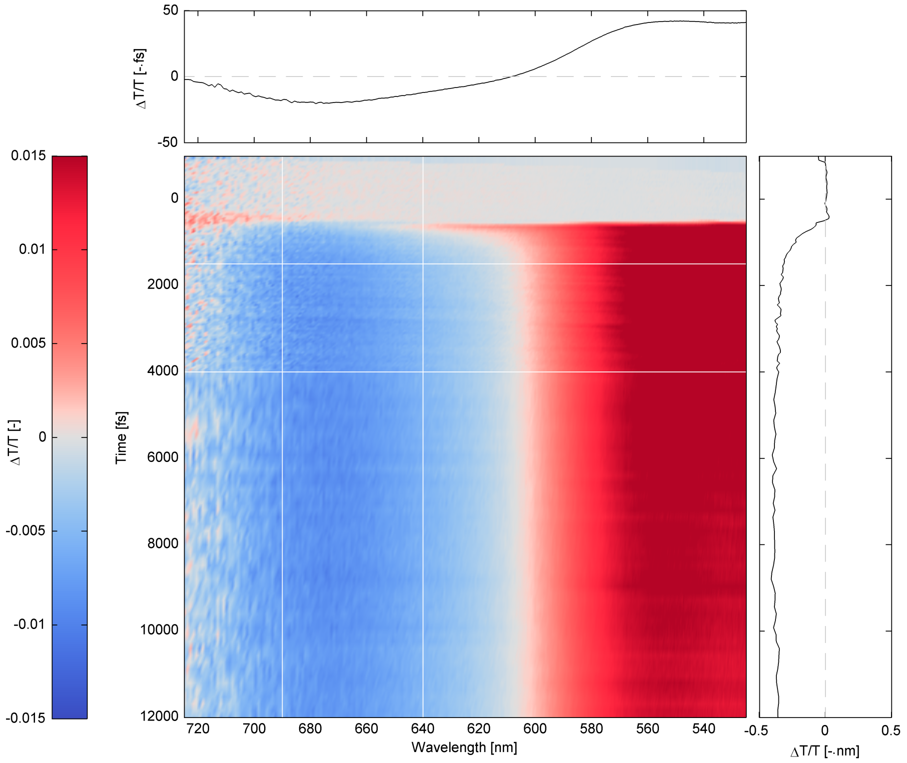

Figure 1.4: Typical TA map showing temporally and spectrally resolved differential transmission. Profiles corresponding to integrated spectra (upper panel) and dynamics (right panel) within the depicted limits are also shown.

related to changes in individual state populations, $\Delta n = n_{\text{pump on}} - n_{\text{pump off}}$, by

$$\Delta A = \sum_i \sigma_i(\lambda)\Delta n_i(t)L \ , \tag{1.7}$$

where the summation is over all states and $n_{\text{pump off}}$ is generally equal to zero for all states except the ground state. A corresponding expression in terms of probe transmission T can be obtained via the relation $A = -\ln(T)$,

$$\begin{align} \Delta A &= -\ln(T_{\text{pump on}}) + \ln(T_{\text{pump off}}) \tag{1.8}\\ &= -\ln\left(\frac{T_{\text{pump on}}}{T_{\text{pump off}}}\right) \tag{1.9}\\ &\approx -\left(\frac{T_{\text{pump on}}}{T_{\text{pump off}}} - 1\right) \tag{1.10}\\ &= -\frac{\Delta T}{T_{\text{pump off}}} \ , \tag{1.11} \end{align}$$

where the approximation $\ln(x) \approx x - 1$ was used.

Similarly to TPL, temporal resolution in TA measurements is typically achieved in the time domain utilising a short excitation pulse followed by subsequent detection of incident probe radiation. Regardless of the detection system, the measured quantity will be at least a convolution of the temporal profiles of excitation pulse and sample response, and so deconvolution is necessary in order to recover true sample responses. As such TA measurements are typically performed with short excitation pulses. A variety of detection schemes are available for temporal resolution and include electronic and optical systems. Regardless of scheme, careful control of spectral content of both excitation and probe sources are required in order to match steady-state and induced transition energies. Briefly:

Electronic detection

Flash-photolysis A continuous wave (i.e. time invariant) light source — typically a broadband incandescent source such as a Xenon or Quartz-Tungsten-Halogen (QTH) lamp — is used as the probe field, providing constant sample illumination. A pulsed tunable source, such as a ps/ns laser and nonlinear optical systems, is used as the excitation field. The signal arising from the probe beam (e.g. transmission, reflection, etc.) is detected at a given delay time before/after excitation by fast electronic detectors. In the simplest case, a fast photo-diode coupled to a oscilloscope is used to detect the probe signal as a function of time. The change in signal intensity is calculated by comparing the signal before and after sample excitation. Alternatively, a fast gating detector array such as an intensified CCD can be used to detect multiple channels — typically mapped to different wavelengths by a spectrograph — at given

times before/after excitation. In this case, a second reference measurement without/before excitation must be performed in order to determine the change in signal intensity. In both cases, the temporal resolution is typically limited by the response time of the detection system.
Typical resolution: ~10 ns

Optical detection

fs pump-probe The output of an ultrafast source, such as a fs laser system, is split into pump and probe pulses by a thin beam-splitter. Both pulses can be used to seed nonlinear optical systems in order to match their spectral content to the steady state and induced absorption bands of the sample. For broadband detection, the probe pulse is often used for super-continuum generation so as to provide spectrally broadening and allow the simultaneous probing of many different transitions. The pump and probe pulses are spatially overlapped on the sample, with the temporal delay between the two pulses being given by an optical delay line. The resulting probe signal (e.g. transmission, reflection, etc.) is detected by a slow detector. The change in probe intensity is achieved by modulating the pump pulses so as to have one pump pulse for every two probe pulses. In this way, the difference in intensity between alternate probe pulses yields the differential signal at the given pump-probe delay. Full dynamics are built up by scanning of the optical delay line.
Typical resolution: ~100 fs

As with TPL, it should be noted that TA measurements can also be performed in the frequency domain through application of Fourier relations. Once again, these are outside the scope of this text and so interested readers are referred to 1–3.

1.1.3 Nonlinear Optics for Transient Spectroscopies

As described in § 1.1.1 and § 1.1.2, pulsed sources are a necessity for transient measurements in the time-domain, with shorter pulses enabling higher temporal resolutions. Pulsed lasers have therefore become popular excitation sources for transient spectroscopic systems due to their very short pulse durations, high repetition rates, high stabilities and technological maturity. Furthermore, as good spectral control of the excitation source is often of importance, the tunability offered by the wide gain band materials found in many pulsed laser systems makes them even more attractive. Whilst these gain bands can span several hundred nanometres, they often remain insufficiently broad to probe the wide range of transition energies which are of interest in many samples. As such, further optical systems are frequently utilised in spectroscopic systems to increase the spectral breadth of a pulsed source.

Predominant amongst such optical systems are those exploiting nonlinear optical effects induced in certain media at very high optical powers. Whilst such powers are difficult to achieve in the continuous wave (CW) regime due to the unfeasibly high sustained energies required, they can be relatively easily obtained in pulsed regimes due to the increase in instantaneous peak power with decreasing pulse duration. With current technology, even unamplified optical oscillators are capable of reaching peak powers in the MW regime — more than sufficient for induction of nonlinear optical effects.

Given their ubiquitous use in the developed TPL system, a brief introduction to the nonlinear optical effects exploited is presented in this section. Once again, this is not to be considered comprehensive and interested readers are referred to further texts such as 4, 5, 11.

1.1.3.1 Nonlinear Optical Media

Maxwell's equations in vacuum are linear and support the occurrence of propagating electromagnetic (EM) waves as solutions of the linear wave equation

$$\nabla^2\mathbf{E} - \mu\epsilon\frac{\partial^2\mathbf{E}}{\partial t^2} = 0\ , \tag{1.12}$$

where $\mathbf{E}$ is the electric field and μ, ϵ are the permeability and permittivity respectively. Nonlinear effects therefore only arise in media, where there can be a material response to the electric field of the wave[*]. More specifically, the oscillating electric field of the travelling wave can induce a dipole moment in the medium, whose spatial density is known as the induced polarisation. At low field amplitudes, the induced polarisation is generally considered to be directly proportional to the applied electric field, with the proportionally constant known as the linear susceptibility, $\chi^{(1)}$. This approximation does not however accurately represent the medium response at high field amplitudes, where instead the complex medium response is better approximated perturbatively as a power series in electric field amplitude. Thus, the induced polarisation, $\mathbf{P}$, is related to the electric field, $\mathbf{E}$, by

$$\begin{aligned}\mathbf{P} &= \chi^{(1)}\mathbf{E} + \chi^{(2)}\mathbf{E}^2 + \chi^{(3)}\mathbf{E}^3 + \ldots &\quad (1.13a)\\ &= \sum_{j=1}^{\infty}\chi^{(j)}\mathbf{E}^j\ , &\quad (1.13b)\end{aligned}$$

where $\chi^{(j>1)}$ are known as the nonlinear susceptibilities. To account for interactions between the induced polarisation and the travelling wave, an additional contribution to the electric flux from the polarisation must be introduced into the wave equation. Splitting the induced polarisation into linear ($\mathbf{P}^{(1)} = \chi^{(1)}$) and non-linear ($\mathbf{P}^{NL} = \chi^{(j>1)}$) components, this nonlinear wave equation can be shown to be [4, 5]

---

[*] N.b. Only optical nonlinear effects based on the electric field of the EM wave will be considered here due to its significantly higher amplitude as compared to the magnetic field

$$\nabla^2\mathbf{E} - \mu\epsilon^{(1)}\frac{\partial^2\mathbf{E}}{\partial t^2} = \mu\frac{\partial^2\mathbf{P^{NL}}}{\partial t^2} \,. \tag{1.14}$$

Equation 1.14 shows how the nonlinear induced polarisation acts as a source term, thereby enabling interaction between travelling waves and induced polarisations.

The nonlinear susceptibilities of most materials decrease rapidly above third order, and so second and third order nonlinear effects dominate most nonlinear optical interactions. Third order nonlinear effects were not utilised in the TPL system however, and so the discussion presented here will be limited to second order interactions where only the magnitude of $\chi^{(2)}$ is significant.

By consideration of symmetry conditions [5], it can be shown that $\chi^{(2)}$ is only non-zero for crystalline material systems whose lattices lack inversion symmetry. As such, second order nonlinear effects are most commonly observed in unixaial crystalline systems such as β-BaB$_2$O$_4$ (BBO), LiB$_3$O$_5$, LiNbO$_3$, etc. Application of Equation 1.13 to the specific case of two monochromatic plane waves of different frequencies co-propagating within a second order nonlinear medium allows identification of three second order nonlinear effects with propagating solutions; second harmonic generation (SHG), sum frequency generation (SFG) and difference frequency generation (DFG). All these second order effects were exploited in building the TPL system.

1.1.3.2 Second Harmonic Generation

Under certain conditions, the frequency of an input wave can be doubled in a second order nonlinear medium via a process known as second harmonic generation. Assuming an input wave at frequency ω and expecting an additional travelling wave output at frequency 2ω, the electric field of the travelling waves within the medium can be written as[*]

$$E(z,t) = \frac{1}{2}\left[\tilde{E}_\omega(z)e^{i(\omega t - k_\omega z)} + \tilde{E}_{2\omega}(z)e^{i(2\omega t - k_{2\omega}z)} + \text{c.c.}\right] \,, \tag{1.15}$$

where $\tilde{E}$ and c.c. represent complex amplitudes and conjugates respectively. Calculation of the induced polarisation caused by such fields via Equation 1.13 requires evaluation of their tensor products with $\chi^{(2)}$. Subsumption of these products into an effective nonlinear coefficient, d_eff, yields an induced nonlinear polarisation

$$P^{NL}(z,t) = \frac{\epsilon_0 d_\text{eff}}{2}\left[\tilde{E}^2_\omega(z)e^{2i(\omega t - k_\omega z)} + 2\tilde{E}_{2\omega}(z)\tilde{E}^*_\omega(z)e^{i(\omega t - [k_{2\omega}-k_\omega]z)} + \text{c.c}\right] \,. \tag{1.16}$$

---

[*] Whilst a scalar model is presented for simplicity, it should be noted that all fields are in fact vector quantities. Therefore, the nonlinear susceptibilities are only fully described as tensors of rank $j + 1$

Substitution of this polarisation into the nonlinear wave equation (1.14) results in a pair of coupled differential equations describing the SHG process,

$$\frac{\partial \tilde{E}_{\omega}}{\partial z} = \frac{-i\omega d_{\text{eff}}}{n_{\omega} c} \tilde{E}_{2\omega} \tilde{E}_{\omega}^{*} e^{-i\Delta k z} \tag{1.17a}$$

$$\frac{\partial \tilde{E}_{2\omega}}{\partial z} = \frac{-i\omega d_{\text{eff}}}{n_{2\omega} c} \tilde{E}_{\omega}^{2} e^{i\Delta k z} \ , \tag{1.17b}$$

where $\Delta k = k_{2\omega} - 2k_{\omega}$ is known as the phase mismatch, and n_{ω}, $n_{2\omega}$ are the medium refractive indices at frequencies ω and 2ω respectively. The phase mismatch can be seen to strongly modulate the SHG process. Assuming perfect phase matching, no input second harmonic wave and a high intensity fundamental wave,

$$\Delta k = 0, \quad \tilde{E}_{2\omega}(0) = 0, \quad \tilde{E}_{\omega}(z) \approx \tilde{E}_{\omega}(0) \ , \tag{1.18}$$

the solution of Equations 1.17 in terms of electric field intensities, I, can be shown to be

$$I_{2\omega}(z) = \frac{2\kappa^2}{\epsilon_0 c n} I_{\omega}^2 z^2 \ , \tag{1.19}$$

with,

$$\kappa = \frac{\omega d_{\text{eff}}}{cn}, \quad n = n_{\omega} = n_{2\omega} \ , \tag{1.20}$$

as required for phase matching (see § 1.1.3.6). In this manner, the input wave at frequency ω us converted into a wave of frequency 2ω during propagation through the nonlinear medium.

1.1.3.3 Sum Frequency Generation

If two waves of different frequencies ω_1 and ω_2 are co-incident on a second order nonlinear medium, an output travelling wave of frequency $\omega_1+\omega_2$ can be generated in a process referred to as sum frequency generation*. In an analogous approach to that presented for SHG, assuming input waves of frequencies ω_1, ω_2 and expecting an additional output wave of frequency $\omega_3 = \omega_1 + \omega_2$, the electric fields of the travelling waves can be written as

$$E(z,t) = \frac{1}{2}\left[\sum_{j=1}^{3} \tilde{E}_j(z) e^{i(\omega_j t - k_j z)} + \text{c.c.}\right] \ . \tag{1.21}$$

Application of Equation 1.13 yields the induced nonlinear polarisation,

$$P^{NL}(z,t) = \epsilon_0 d_{\text{eff}} \Big[\tilde{E}_1 \tilde{E}_2 e^{i(\omega_3 t - [k_1+k_2]z)} + \tilde{E}_3 \tilde{E}_1^{*} e^{i(\omega_2 t - [k_3-k_1]z)} + \tilde{E}_3 \tilde{E}_2^{*} e^{i(\omega_1 t - [k_3-k_2]z)} + \text{c.c.} \Big] \ , \tag{1.22}$$

---

*Indeed, it can be seen that SHG is just a specific case of SFG which upon substitution into the nonlinear wave equation (1.14) yields three coupled differential equations,

$$\frac{\partial \tilde{E}_1}{\partial z} = -i\kappa_1 \tilde{E}_3 \tilde{E}_2^* e^{-i\Delta k z} \tag{1.23a}$$

$$\frac{\partial \tilde{E}_2}{\partial z} = -i\kappa_2 \tilde{E}_3 \tilde{E}_1^* e^{-i\Delta k z} \tag{1.23b}$$

$$\frac{\partial \tilde{E}_3}{\partial z} = -i\kappa_3 \tilde{E}_1 \tilde{E}_2 e^{i\Delta k z} \ , \tag{1.23c}$$

where,

$$\kappa_j = \frac{\omega_j d_{\text{eff}}}{2n_j c}, \quad \Delta k = k_3 - k_2 - k_1 \ . \tag{1.24}$$

Once again, assuming perfect phase matching, no input wave at ω_3 and high intensity ω_1 and ω_2 waves,

$$\Delta k = 0, \quad \tilde{E}_3(0) = 0, \quad \tilde{E}_{1,2}(z) \approx \tilde{E}_{1,2}(0) \ , \tag{1.25}$$

the solution of Equation 1.23 in terms of intensities can be shown to be

$$I_3(z) = \frac{\omega_3^2 d_{\text{eff}}^2}{2c^3 \epsilon_0 n_1 n_2 n_3} I_1 I_2 z^2 \ . \tag{1.26}$$

In this manner, the input waves at ω_1 and ω_2 are converted into a wave of frequency $\omega_3 = \omega_1 + \omega_2$ during propagation through the nonlinear medium. Within a quantum framework, sum frequency generation can be thought of as the creation of a photon of energy $\hbar\omega_3$ via the annihilation of a pair of photons of energies $\hbar\omega_1$ and $\hbar\omega_2$.

1.1.3.4 Difference Frequency Generation

The inverse of SFG can also occur — viz. the generation of a wave at a frequency equal to the difference of the input frequencies, $\omega_2 = \omega_3 - \omega_1$ — and is termed difference frequency generation. Being the inverse process, the same three field equations (1.23) governing SFG are valid for DFG. Under perfect phase matching, no input wave at ω_2 and high intensity ω_3 and ω_1 waves,

$$\Delta k = 0, \quad \tilde{E}_2(0) = 0, \quad \tilde{E}_{1,3}(z) \approx \tilde{E}_{1,3}(0) \ , \tag{1.27}$$

it is therefore trivial to show that the corresponding solution of Equation 1.23 is simply given by

$$I_2(z) = \frac{\omega_2^2 d_{\text{eff}}^2}{2c^3 \epsilon_0 n_1 n_2 n_3} I_1 I_3 z^2 \ . \tag{1.28}$$

In this manner, the input waves at ω_1 and ω_3 are converted into a wave of frequency $\omega_2 = \omega_3 - \omega_1$ during propagation through the nonlinear medium. Within a quantum framework, different frequency generation can be thought of as the creation of a pair of photons of energies $\hbar\omega_2$ and $\hbar\omega_1$ via the annihilation of a single photon of energy $\hbar\omega_3$.

1.1.3.5 Optical Parametric Oscillators

Inspection of DFG reveals that the ω_1 photons are not being annihilated themselves, but are instead only acting as a stimulus for the creation of the ω_2 photon. As such, the intensities of both the ω_2 *and* ω_1 waves increase during propagation through the nonlinear medium. Difference frequency generation therefore presents an interesting scenario in which the energy of the high frequency incident wave can be transmitted to the pair of lower frequency waves. In particular, the incident low frequency wave (ω_1) can be thought to be amplified through this interaction. Systems exploiting DFG in this manner are known as optical parametric amplifiers (OPAs) and are widespread in transient spectroscopic systems as they allow weak pulses at desired wavelengths to be amplified by stronger pulses at easily generated wavelengths (e.g. laser fundamentals). Given this amplification process, the different frequency waves in OPAs are frequently termed pump (ω_3), signal (ω_1) and idler (ω_2) waves.

Whilst very efficient amplification can be achieved by OPAs, high pump powers only attainable with amplified laser systems are typically required. In order to exploit the amplification afforded by DFG using lower pump powers, multiple passes of the nonlinear medium can instead be employed by locating the OPA within an optical cavity. Such systems are termed optical parametric oscillators (OPOs) and permit signal amplification at the lower pump energies attainable by unamplified laser systems. Optical parametric oscillators can be classified according to the waves which their cavities support, with singly resonant OPOs circulating only the signal waves, doubly resonant OPOs circulating both signal and idler waves, and triply resonant OPOs circulating signal, idler and pump waves*.

In order for amplification to take place, the gain acquired by the signal wave on propagation through the nonlinear medium must exceed any cavity losses (e.g. partially transmissive/absorbing cavity mirrors, absorption within the nonlinear medium, etc.) for each round trip. As such, a minimum threshold gain — typically manifested as a minimum pump intensity — is required for OPO operation. The material properties of the nonlinear medium and the cavity finesse are therefore critical parameters for achieving low-threshold operation. Due to the greater energy circulated within the cavity, it can be shown that a doubly resonant OPO always has an inherently lower threshold gain than its singly resonant counterpart.

---

*The practical uses of triply resonant OPOs are limited however due to their complexity and relative instability

Despite this obvious advantage, it is often preferable to configure an OPO to be singly resonant so as to facilitate spectral tuning. In close analogy to laser cavities, the OPO spectral mode structure is given by the product of the OPO gain spectrum and the cavity mode structure (Figure 1.5). The cavity mode structure is determined by the cavity length, finesse and dispersion, and is typically in the 10 MHz to 1000 MHz range for lab-scale cavities. The gain spectrum on the other hand is predominantly defined by the phase matching conditions (see § 1.1.3.6 below) and so can be tuned over a very wide spectral range (typically >1000 GHz)[*]. As such, oscillation can potentially occur at many different cavity modes, however singly resonant OPOs tend to oscillate at the cavity mode closest to the gain maximum (Figure 1.5). Two practical parameters therefore exist for tuning the output wavelength of a singly resonant OPO; the phase matching conditions (position of the gain spectrum maximum), and the cavity length (form of the cavity mode structure). For doubly resonant OPOs on the other hand, dispersion within the cavity medium leads to slightly different signal and idler mode structures. Oscillation is therefore greatly favoured at a frequency supported by both mode structures, which need not necessarily be coincident with the gain spectrum maximum (Figure 1.5). As such, cavity length tuning of doubly resonant OPOs is not very smooth, with small length fluctuations capable of causing significant changes in the output wavelength. The greater stability afforded by singly resonant OPOs as compared to doubly resonant OPOs is usually considered to outweigh their slightly higher operating thresholds.

1.1.3.6 Birefringent Phase Matching

It the preceding discussions, perfect phase matching was assumed and resulted in derivations for second order nonlinear processes at ideal efficiencies. All the coupled differential equations obtained can however be integrated directly to yield solutions under phase mismatched conditions which show large reductions in nonlinear process efficiency when $\Delta k \neq 0$. Good phase matching requires careful consideration of the nonlinear medium refractive indices at the frequencies of the wave involved. More specifically, it is simple to show that perfect phase matching for SHG is achieved when,

$$\Delta k = 0 \quad \Rightarrow \quad n_{2\omega} - n_{\omega} = 0 \ , \tag{1.29a}$$

whilst for SFG and DFG,

$$\Delta k = 0 \quad \Rightarrow \quad n_3\omega_3 - n_2\omega_2 - n_1\omega_1 = 0 \ . \tag{1.29b}$$

---

[*] Whilst OPOs are in many ways analogous to lasers, a key benefit is that their gain band is not tied to fixed transition energies of the gain medium, but is instead only limited by the tunable phase matching conditions. Very broadband amplification can therefore be achieved by OPOs, making them very useful and versatile spectroscopic tools. In particular, OPAs are frequently used in the generation of ultra-short (<10 fs) and therefore ultra-broadband pulses [12]

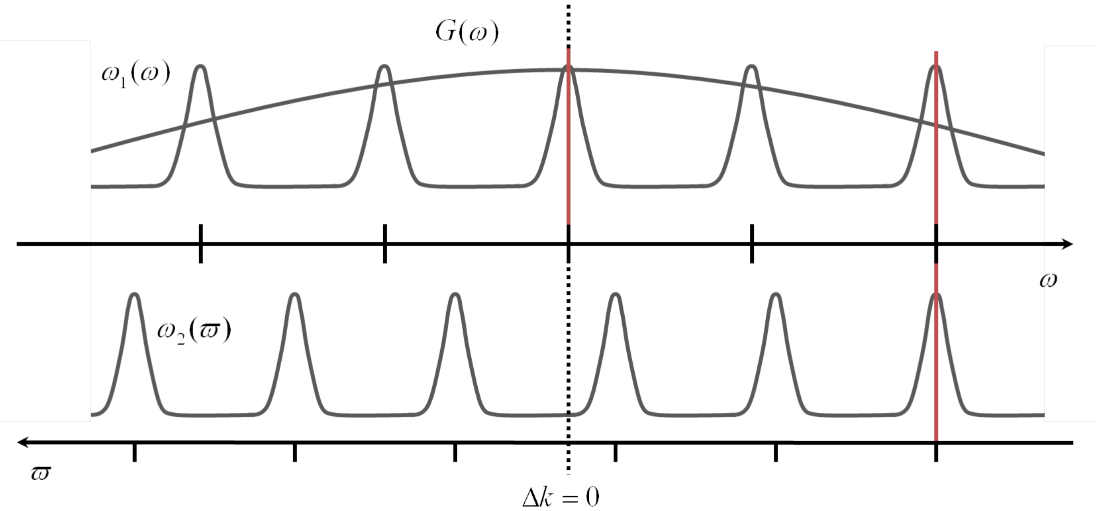

Figure 1.5: Spectral mode structures of singly (top) and doubly (top and bottom) resonant OPOs. The OPO gain spectrum ($G(\omega)$) and cavity mode structures for signal and idler fields ($\omega_1(\omega)$ and $\omega_2(\bar{\omega})$) are also shown. The OPO operational frequency in each case is depicted by the solid red line [adapted from 5]

The optical dispersion, $n = n(\omega)$, of most materials is however a non-analytical function of frequency, with n typically increasing with increasing frequency. As such, phase matching cannot generally be achieved at arbitrary wavelengths without some effort.

One of the most common techniques for overcoming this hurdle is birefringent phase matching, where the anisotropy of the (linear) refractive index of a medium is exploited to give an extra degree of freedom which can be used for phase matching. It is therefore fortuitous that many media with high nonlinear susceptibilities also exhibit birefringence. Indeed, for second order nonlinear processes, the required lack of inversion symmetry often means that the nonlinear media are uniaxial, with one crystal axis exhibiting a different refractive index to the others. This exceptional refractive index is denoted the extraordinary index, n_e, whilst the other is denoted the ordinary index, n_o.

Whilst the solution of the wave equation in isotropic media necessarily implies $(\mathbf{E} \times \mathbf{H}) \cdot \mathbf{k} = 1$, they same is not true for solutions in anisotropic media, where $\mathbf{E} \cdot \mathbf{k}$ need not equal 0. For the specific case of uniaxial media, it can be shown that for any one propagation direction, two related solutions of the wave equation — denoted the ordinary (o) and extraordinary (e) waves — coexist. The o- and e-waves are differentiated by the orientation of their electric fields with respect to the anisotropic axis, and so experience different refractive indices. As

	Interaction		PM condition
Polarity	Nomenclature	Polarisations	SFG/DFG
Positive	Type I	$e + e \to o$	$\omega_2 n_e(\omega_2, \theta) + \omega_1 n_e(\omega_1, \theta) = \omega_3 n_o(\omega_3)$
	Type II	$o + e \to o$	$\omega_2 n_o(\omega_2) + \omega_1 n_e(\omega_1, \theta) = \omega_3 n_o(\omega_3)$
Negative	Type I	$o + o \to e$	$\omega_2 n_o(\omega_2) + \omega_1 n_o(\omega_1) = \omega_3 n_e(\omega_3, \theta)$
	Type II	$o + e \to e$	$\omega_2 n_o(\omega_2) + \omega_1 n_e(\omega_1, \theta) = \omega_3 n_e(\omega_3, \theta)$

Table 1.1: Birefringent phase matching nomenclature, polarisation configurations and conditions for positively and negatively birefringent uniaxial media [adapted from 4, Ch. 5]

a consequence, their wavevectors, k_o and k_e, are given by

$$k_o = \frac{\omega n_o}{c} \tag{1.30a}$$

$$k_e = \frac{\omega n_e(\theta)}{c} \ , \tag{1.30b}$$

with,

$$\frac{1}{n_e^2(\theta)} = \frac{\cos^2(\theta)}{n_o^2} + \frac{\sin^2(\theta)}{n_e^2} \ . \tag{1.31}$$

These relations show that whilst the wavevector of an o-wave is fixed by material parameters, the wavevector of an e-wave is a function of the angle, θ, between the direction of propagation and the anisotropic axis. The wavevector of an e-wave can therefore be easily tuned by rotation of the nonlinear medium with respect to the impinging e-wave. This extra degree of freedom allows phase matching to be achieved in uniaxial media at arbitrary wavelengths as long as one of the interacting waves is e-polarised. The exact polarisation configuration required for phase matching can be derived from solution of the full nonlinear wave equation in a uniaxial medium. It can be shown that solutions exist for both parallel and orthogonally polarised input waves, with the polarisation determined by the material birefringence polarity*. The four resulting configurations are summarised in Table 1.1.

By way of example, for Type-I phase matched SFG in a negative uniaxial medium such as BBO, the interaction is mediated by an $o + o \to e$ configuration and thus the phase matching condition becomes

$$\omega_3 n_e(\omega_3, \theta) - \omega_2 n_o(\omega_2) - \omega_1 n_o(\omega_1) = 0 \ . \tag{1.32}$$

Knowledge of the ordinary and extraordinary medium dispersions allow solution of this equation, yielding the required phase matching angle.

---

*Uniaxial materials with $n_e > n_o$ are denoted positively birefringent, whilst those with $n_e < n_o$ negatively birefringent

1.1.3.7 Quasi-Phase Matching

An alternative approach to phase matching — often utilised when birefringent phase matching is not possible or desirable — is quasi-phase matching. This involves periodic spatial modulation of the nonlinear properties of a medium, and is most easily achieved in media with anisotropic nonlinear susceptibilities where the direction of the nonlinearity can be varied*. Mathematically, such a periodic modulation can be described as the product of the effective nonlinear coefficient, d_{eff} with a Fourier series of unit amplitude,

$$d_{\text{eff}}(z) = d_{\text{eff}} \sum_{p=1}^{\infty} A_p e^{ip2\pi\left(\frac{1}{\Lambda}\right)z} \ , \tag{1.33}$$

where Λ is the modulation period and A_p are the Fourier amplitudes. Substitution of this expression into the coupled differential equations for second order interactions (e.g. Equations 1.17, 1.23), followed by their subsequent integration yields expressions describing the evolution of the interacting fields in such a periodic nonlinear medium†. Inspection of these solutions show that the periodicity introduces new phase matching conditions involving the modulation period, Λ. For the specific case of square periodic modulation — i.e. periodic inversion of the nonlinear coefficient — the new SHG phase matching condition can be shown to be

$$\Delta k = 0 \quad \Rightarrow \quad n_{2\omega} - n_{\omega} - \frac{\pi c}{\Lambda \omega} = 0 \ , \tag{1.34a}$$

whilst for SFG and DFG,

$$\Delta k = 0 \quad \Rightarrow \quad n_3\omega_3 - n_2\omega_2 - n_1\omega_1 - \frac{2\pi c}{\Lambda} = 0 \ . \tag{1.34b}$$

In this manner, the periodicity of the nonlinear coefficient can be seen to act as a grating, imparting an additional contribution to the wavevector sum and thereby an additional degree of freedom. Intrinsic phase mismatch in the medium can therefore be compensated by the correct choice of grating period.

In practice, such stepped nonlinear media are fabricated by application of a strong electric field during crystal growth so as to orient its dielectric properties. In this way, periodic inversion of the field — known as poling — yields in periodic inversion of the nonlinear properties, resulting in what are aptly named periodically poled non linear crystals. Perhaps the most common example of such a crystal is periodically poled lithium niobate (PPLN or PP-LiNiO_3). Several different discrete grating periods can be fabricated along the transversal length of the crystal, allowing facile selection of Λ by appropriate positioning of the incident beam on the crystal facet. Advanced fabrication techniques also allow the grating period to be varied continuously along the transversal length of the crystal — a geometry known as fan-out poling — thereby allowing continuous tuning of Λ.

---

* Recall that χ is a tensor quantity

† See reference [4] for a full derivation

1.2 Transient PL System

1.2.1 Motivation & Specification

The areas of research at the CNST are wide and varied and currently include organic materials for biological applications and biomimetic devices, third generation photovoltaics, and nanostructured materials and interfaces for energy applications [13]. The development of the TPL system at the CNST was born out of the requirement for a general purpose system for investigation of the wide range of materials and phenomena associated with these research fields. Given this, the following system specifications and accompanying motivations were given at the outset of the project:

Spectral range and resolution Broadband excitation and detection spanning UV-Visible-NIR spectral regions (260 nm to 1400 nm) with resolution of a few nm

- **Visible band (**400 nm **to** 750 nm**)** Provides coverage of most low energy transitions in the most common conjugated systems (see § 2.1.1.1) currently under study. It also covers the peak intensities of the solar spectrum which is of key importance for solar energy research
- **UV band (**260 nm **to** 400 nm**)** Provides coverage of the peak absorption band of DNA for investigation of biological systems
- **NIR band (**750 nm **to** 1400 nm**)** Provides coverage of spectral region of key interest for research into complementary absorbers for PV applications. This is due to the fact that a significant fraction of solar energy outside of the visible range is located in the NIR

Temporal range and resolution Detection resolved from a few ps to ms

- ps–ns **range** Allows detection of fast radiative phenomena (i.e. fluorescence) and the indirect observation of competition between decay channels (e.g. radiative decay vs. energy transfer, electron transfer, vibrational relaxation, etc.). Furthermore, provides temporal overlap with fs-resolved TA systems - typically operating in the <2 ns time range - for assistance in interpretation of complex TA spectra[*]

---

[*] It should be noted that for true overlap with fs-resolved TA systems, the possibility of an optically resolved transient emission system such as upconversion or Kerr gating (see § 1.1.1) was also considered. The complexity of excitation source, challenges of achieving broadband operation, short temporal range and specific sample requirements were however considered too great to proceed with this approach. As such, it was decided that a separate fs-resolved transient PL system would be pursued at a later date.

µs–ms **range** Allows detection of slow radiative phenomena such as phosphorescence and delayed fluorescence (see § 2.1.1.4, § 2.1.3). Furthermore, provides temporal overlap with ns-resolved TA systems for assistance in interpretation of complex TA spectra.

Spatial resolution Three-dimensional spatial resolution of excitation/emission down to few µm

Enables resolution of local photophysics in micro-ordered systems, such as the intra-cellular structure of biological cells, large donor/acceptor domains in bulk heterojunction solar cells and the exclusion of defect emission in locally defective samples. Also allows investigation of emission from single isolated microscopic components such as molecules, quantum dots, etc.

Sample compatibility Accommodation of wide variety of sample architectures and environments including inert atmosphere and low-temperatures conditions

Avoids deleterious effects arising from photo-induced sample oxidation, most notably in organic conjugated systems. Cryogenic sample cooling facilitates spectral and temporal resolution in samples with overlapping spectral emission bands and/or very fast dynamics, as well as allowing investigation of phonon mediated processes.

1.2.2 System Description

In this section, the TPL system developed at the CNST is described. The overall optical layout of the system is shown in Figure 1.6 for reference.

1.2.2.1 Oscillator

A commercial Ti:Al_2O_3 oscillator (Coherent Chameleon Ultra II) was chosen as the fundamental excitation source so as to provide a tunable, broadband source approximately centred in the spectral range of interest (gain band 680 nm to 1080 nm). Intra-cavity passive Kerr-lens mode-locking of the oscillator yielded sech^2 pulses with a temporal full width half maximum (FWHM) of ∼140 fs. This enabled high temporal resolution of resulting PL across all specified temporal ranges without the need for significant deconvolution. The elevated pulse peak-powers (∼MW) also provided for nonlinear spectral conversion, allowing extension of the spectral coverage on either side of the oscillator gain band. A high repetition rate cavity (80 MHz) was selected so as to yield fast data collection and high signal-to-noise ratios. The location of both pump and cavity mirrors on piezo mounts allowed for real-time monitoring and oscillator adjustment via

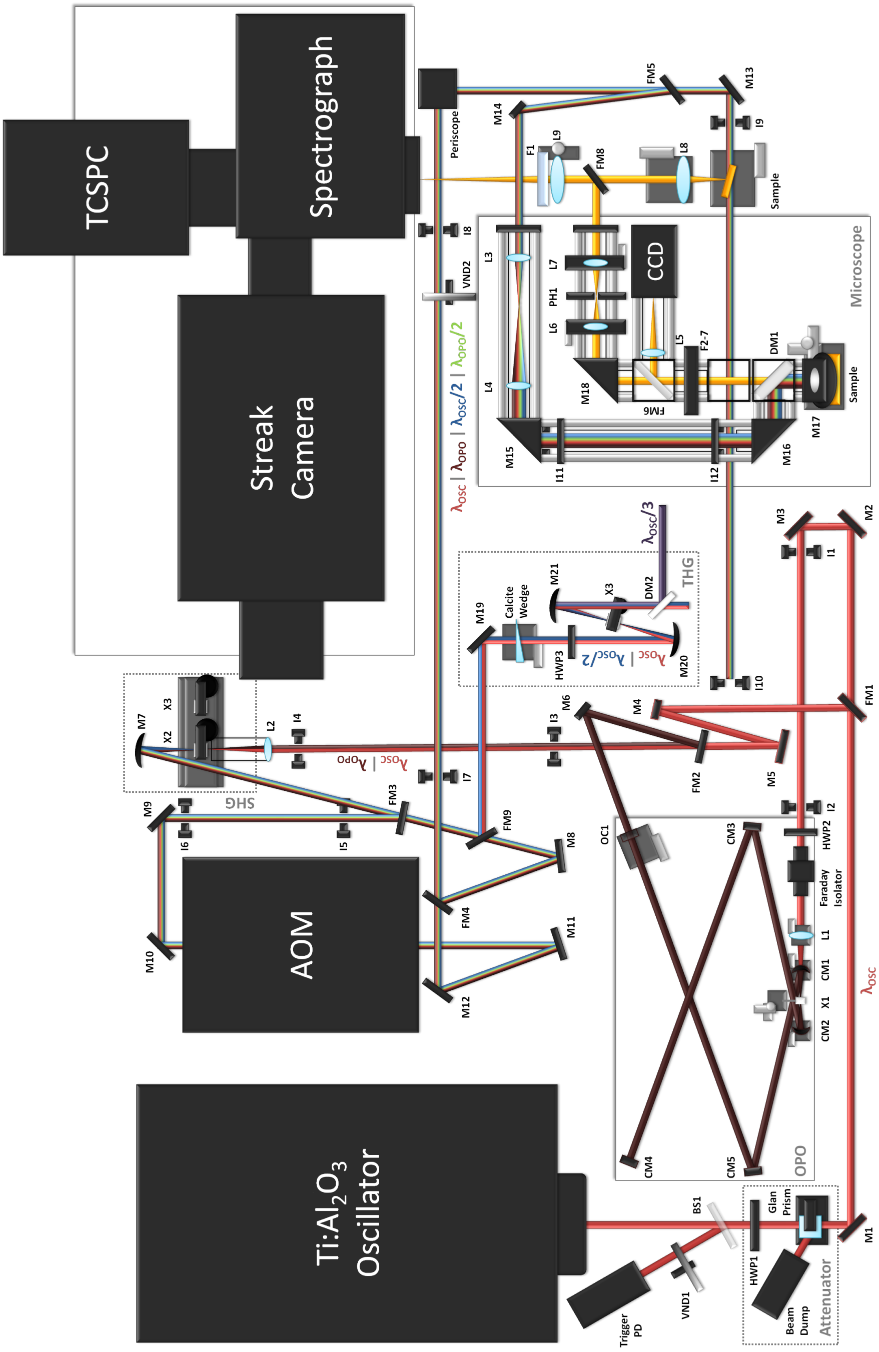
TCSPC
Spectrograph
Streak Camera
AOM
Ti:Al_2O_3 Oscillator
Periscope
M14
FM5
M13
I9
F1
L9
FM8
L8
Sample
I8
L3
L7
PH1
L6
CCD
Microscope
VND2
L4
M18
L5
F2-7
DM1
FM6
Sample
M15
I11
I12
M16
M17
λ_{OSC} | λ_{OPO} | $\lambda_{OSC}/2$ | $\lambda_{OPO}/2$
$\lambda_{OSC}/3$
M19
Calcite Wedge
M21
X3
DM2
THG
HWP3
λ_{OSC} | $\lambda_{OSC}/2$
M20
I10
M3
I1
M2
M6
M4
FM1
I3
FM2
M5
I2
M7
X2
X3
L2
I4
λ_{OSC} | λ_{OPO}
I7
SHG
M9
I6
I5
FM3
FM9
M8
OC1
CM3
HWP2
Faraday Isolator
L1
CM1
X1
CM2
λ_{OSC}
M10
FM4
M11
M12
CM4
CM5
OPO
BS1
Glan Prism
HWP1
M1
Trigger PD
VND1
Beam Dump
Attenuator

Figure 1.6: TPL system optical layout. Abbreviated optical components; steering mirror (M), flip mirror (FM), dichroic mirror (DM), high reflectance cavity mirror (CM), cavity output coupler (OC), beam splitter (BS), absorbing filter (F), variable neutral density filter (VND), half-wave plate (HWP), alignment iris (I), nonlinear crystal (X), lens (L)

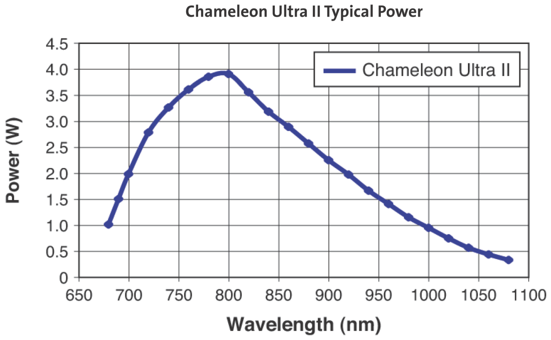

Figure 1.7: Ti:Al_2O_3 oscillator (Coherent Chameleon Ultra II) output power characteristics [adapted from the Coherent Ultrafast Laser Systems 2012/2013 Product Catalog]

a feedback loop incorporating a cavity photo-diode. This yielded very high stability output which was further enhanced by hermetic sealing of the cavity so as to avoid dust ingress. In addition, this setup permitted remote and automated tuning of the cavity mode via an intuitive software interface.

Aside from installation, confirmation of correct operation and periodic maintenance, no significant development of the oscillator was required.

Given the fixed oscillator output power — being determined only by the spectral properties of the Ti:Al_2O_3 gain band and cavity reflectivity — a high power variable attenuator was constructed immediately after the output to allow for power regulation. This was comprised of a broadband half-wave ($\lambda/2$) plate, air-spaced Glan-Taylor prism and beam dump. The prism was configured so as to reject vertical (with respect to the optical table plane) and pass horizontal polarisations, with a Malus law [14] transmission dependency.

1.2.2.2 Excitation Repetition Rate Selection

Whilst an 80 MHz oscillator repetition rate yields a small cavity footprint, the resulting 12.5 ns pulse-pulse interval can be too short for many emissive species. For samples with emission lifetimes greater than $(1/5) \cdot 12.5 \approx 2.5$ ns, such a short pulse-pulse interval results in sample re-excitation before a return to equilibrium conditions. This can affect the system population dynamics due to non-equilibrium initial conditions and can distort the decay profiles due to the 'pile-up' of successive decays. To avoid these problems, an acousto-optical modulator (AOM) was installed (APE pulseSelect) to enable selective transmission of individual pulses in the pulse-train, thereby elongating the pulse-pulse interval. Within this scheme, modulation was achieved via diffraction in a SiO_2 crystal by a transient pressure grating induced by a pulsed radio-frequency transducer. Electronic control of the radio-frequency signal allowed reduction of the pulse-train by an arbitrary division ratio, resulting in pulse-pulse intervals variable by integer multiples of 12.5 ns.

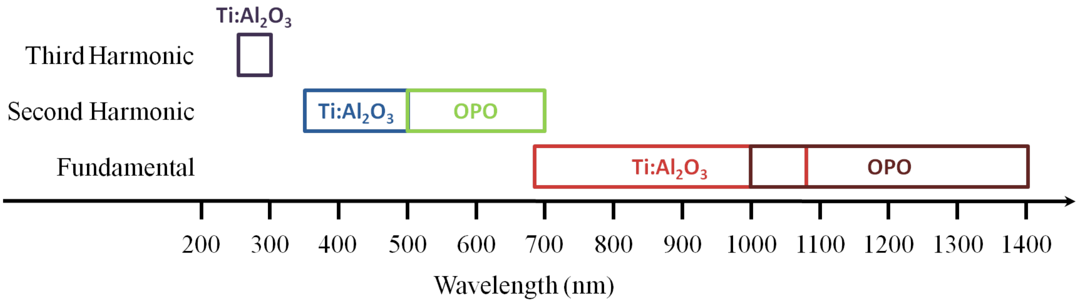

Figure 1.8: Excitation spectrum coverage

Once again, aside from installation, confirmation of correct operation and periodic alignment, no significant development of the modulator was required.

1.2.2.3 Excitation Wavelength Selection

Despite Ti:Al_2O_3 exhibiting the widest gain band available amongst common laser gain media, the extremely broadband excitation specifications imposed precluded the use of a single gain medium for excitation. As such, the high peak powers of the ultra-short oscillator pulses were instead exploited for spectral conversion via the nonlinear interactions described in section 1.1.3. In order to cover the entirety of the specified excitation band, multiple separate nonlinear optical sub-systems were developed (Figure 1.8).

The high-energy portion of visible excitation band was covered via SHG of the Ti:Al_2O_3 oscillator output by focussing onto a BBO crystal — a birefringent optical material with a high $\chi^{(2)}$ nonlinear coefficient. Broadband type-I birefringent phase matching was achieved by rotation of the crystal axis with respect to the impinging beam and residual fundamental was removed by a thin absorbing filter. A crystal cut at 29.3° — corresponding to SHG at 800 nm at normal incidence — was chosen so as to be approximately centred within the oscillator output band. A crystal thickness of 1 mm was chosen to minimise pulse broadening due to chirp [4]. Within this scheme, SHG was achieved from 350 nm to 500 nm with efficiencies exceeding 10 %. The temporal width of the output pulses was not fully characterised, but was shown to be below the highest temporal resolutions of the detection system (<2 ps).

The UV excitation band was covered by type-I birefringent phase matched, angle tuned SFG of the oscillator fundamental with its second harmonic, thereby yielding the third harmonic*. Given the specific excitation wavelengths required within the UVC band — viz. DNA absorption peaks — the third harmonic generation (THG) system was optimised for fundamental wavelengths between 800 and 900 nm. The output of the SHG system was used as the input of the

---

*This work was mainly conducted by Dr. A. Candeo

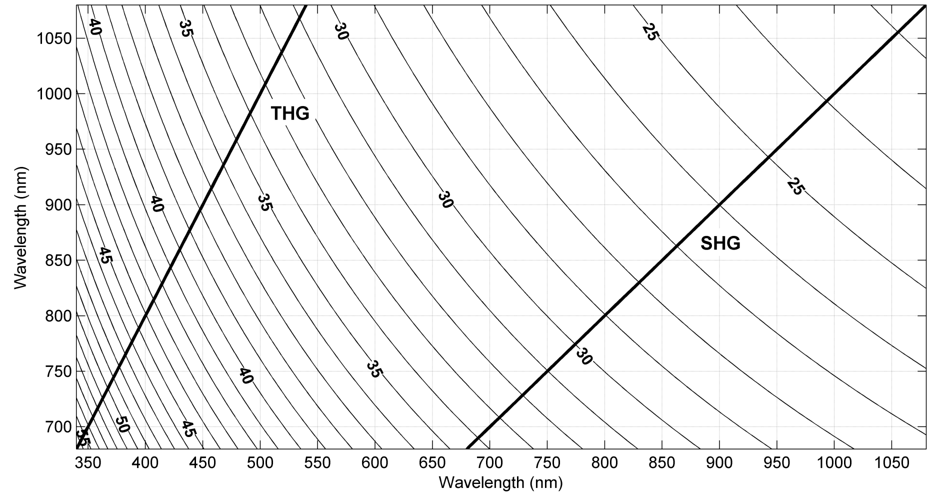

Figure 1.9: Type-I birefringent phase-matching angle (degrees) for SFG in BBO within the Ti:Al_2O_3 oscillator fundamental and second harmonic bands. The solid lines show the specific cases of SHG and THG

THG system, with access to both fundamental and second harmonic wavelengths provided by removal of the absorbing filter. A calcite retarding wedge was used to delay the fundamental pulse with respect to its second harmonic so as to compensate for retardation within the SHG BBO. The orthogonal polarisations of fundamental and second harmonic pulses arising from type-I phase matched SHG were realigned using a wavelength selective half-wave plate so as to allow subsequent type-I phase matched SFG. The pulses were spatially and temporally overlapped within a 1 mm thick BBO crystal cut at 41° — corresponding to THG at 850 nm at normal incidence — and were phase matched by angle tuning. The thickness and cut of the BBO were chosen so as to minimise pulse chirp and be centred in the THG range specified. Residual fundamental and second harmonic pulses were removed using narrow-band dichroic filters. Development of the THG system is still ongoing and so full characterisation is yet to be performed.

The low-energy portion of the visible excitation band and the NIR region not within the Ti:Al_2O_3 gain band were simultaneously covered by the construction of a singly resonant NIR optical parametric oscillator (OPO)[*]. In this scheme, periodically poled lithium niobate (PPLN) was used as a non-linear medium for quasi-phase matched DFG within a linear NIR optical cavity. Nine discrete grating periods were chosen so as generate signal and idler wavelengths in the 1000 nm to 1400 nm and 3545 nm to 1760 nm ranges respectively from 760 nm to 800 nm pump pulses provided by the Ti:Al_2O_3 oscillator. To maximise operational stability, the OPO cavity was designed to be singly resonant, circulating only

---

[*] The experimental part of this work was mainly conducted by Francesco Crisafi and Dr. V. D'Innocenzo

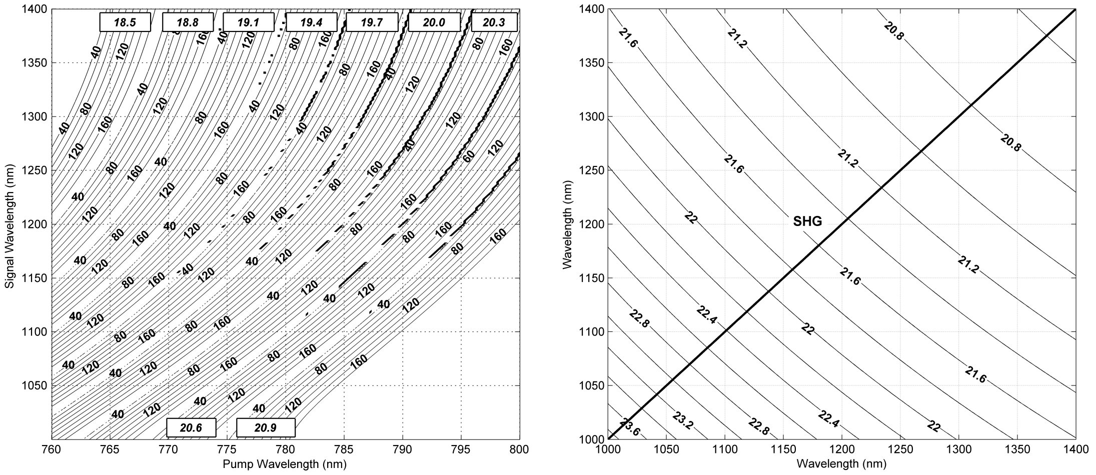

Figure 1.10: *Left panel:* OPO tuning plot showing PPLN temperature (contours, degrees Celsius) required for QPM as a function of PPLN grating period (boxed values, µm) and pump and signal wavelengths. *Right panel:* Type-I birefringent phase-matching angle (degrees) for SFG in BBO within the OPO output band. The solid line shows the specific case of SHG

signal pulses whilst rejecting pump and idler pulses. The cavity length was chosen for operation around 80MHz, with significant tunability to allow exact matching of the Ti:Al_2O_3 oscillator repetition rate. Variation of the pump wavelength, PPLN grating, PPLN temperature and cavity length allowed precise tuning of the signal wavelength across the whole 1000 nm to 1400 nm NIR band as specified. Signal pulses were extracted from the cavity through a 2.5 %T2.5 %T output coupler, and could be optionally frequency doubled by type-I phase-matched, angle-tuned SHG in a BBO crystal cut at 21.4° — corresponding to SHG at 1200 nm at normal incidence — to achieve pulses in the second specified range of 500 nm to 700 nm[*]. The length of the PPLN crystal was carefully chosen to be 5 mm, so as to yield the highest possible DFG efficiency whilst maintaining the signal pulse temporal width below the temporal resolutions of the selected detection systems (<2 ps).

1.2.2.4 Spatial Resolution

Spatial resolution of TPL was achieved through the construction of a confocal microscope. The excitation beam was first expanded by a variable telescope lens system to allow fine control of subsequent focussed spot size. The expanded beam was reflected off a suitably chosen dichroic mirror — typically long-pass — before being coupled into the objective and focussed onto the sample. Sample emission was collected by the same objective and transmitted through the dichroic mirror. At this stage, further absorbing filters could be used to remove residual pump scatter. Focal plane resolution was achieved by focussing the emission beam through a pinhole (typically 50 µm) before subsequent coupling into the detection systems for spectral and temporal resolution. In this manner, diffraction limited in-plane and ~5 µm perpendicular spatial resolution of TPL signals could be achieved.

---

[*] Whilst this configuration yielded highly stable and intense pulses, it should be noted that unintentional phase matching between pump & signal, pump & idler, signal & idler, etc. could also be used to achieve somewhat weaker and less stable output within this wavelength range.

The microscope field of view (FOV) was sampled by a flip mirror and CCD system located before the pinhole, allowing accurate positioning of the sample relative to the excitation beam via sample translation using an XYZ differential micrometer stage. Alternatively, the excitation beam could be positioned relative to the sample by adjustment of the final pump mirror. Both such adjustments were performed manually, but addition of suitable actuator and piezo mounts/stages is planned so as to enable positional automation and FOV scanning.

The incorporation of an such imaging system also enabled facile collection of steady-state fluorescence images by defocussing the pump to achieve full FOV excitation and collecting the resulting emission with the CCD.

In addition to spatial resolution, the microscope system also permitted excitation conditions otherwise difficult to achieve in free space configurations. The normal or near-normal excitation geometry greatly facilitates polarisation dependent measurements such as emission anisotropy. Furthermore, the large objective numerical aperture allows high excitation densities to be achieved, and so the investigation of nonlinear effects such as emission arising from two-photon absorption.

1.2.2.5 Detection Systems

In order to cover the broadband detection specifications, two separate detection systems were selected. Ultraviolet and visible coverage (300 nm to 850 nm) was provided by a streak camera system, yielding the highest possible temporal resolution by electronic means and fast parallel collection of whole TPL maps (e.g. Figure 1.2). Due to the thicker photocathodes required for NIR photoelectric conversion, the temporal resolution of streak camera systems in NIR is significantly lower than in visible wavelength range. The benefits of NIR streak detection were therefore considered insufficient to warrent their complexity and expense, and as such a separate NIR (300 nm to 1400 nm) TCSPC system was selected instead.

With exception of microscopic measurements, sample excitation was generally performed by focussing the excitation beam on the sample so as to obtain an excitation spot diameter of ~100 µm and corresponding maximum photon density of approximately $5 \times 10^{17}\,\mathrm{cm}^{-3}$. The resulting sample emission was collected through a lens-based telescope system with collection solid angle of 0.14π sr. This was designed so as to permit optical cryostats, optical vacuum chambers, cuvettes and various other sample mounting configurations to be used within the sample space. Excitation was generally performed at ∼90° to collection so as to minimise pump collection, however absorbing filters — typically long-pass — were also incorporated into the collection system for further pump scatter elimination. The collected emission was coupled into an Acton SP2300i imaging spectrograph equipped with two visible and one NIR reflecting gratings (150 l mm^{-1}, blaze 300 nm; 150 l mm^{-1}, blaze 1200 nm; 50 l mm^{-1}, blaze 600 nm) to provide broadband spectral resolution. A motorized flip mirror enabled the spectrograph output to be sent to either the streak or TCSPC detection systems. In the case of streak detection, the dispersed emission was imaged onto the streak camera photocathode, providing parallel collection of multiple wavelengths. Conversely, for TCSPC detection, a mechanical slit was used to select a variable bandpass of the dispersed emission for subsequent detection. Full spectra were obtained by automated rotation of the active grating.

Streak-based detection was performed by a Hamamatsu C5680 universal streak camera equipped with both slow (Hamamatsu M5677) and sychroscan (Hamamatsu M5675) sweep units. Sweep triggering was provided by sampling of the Ti:Al_2O_3 oscillator output by a stabilised silicon fast photodiode coupled to variable electronic delays. Two sweep units were chosen so as to have maximum flexibility in temporal resolutions and windows. The principal difference between the units is the form of time-varying voltage applied to the deflection electrodes.

The slow sweep unit provides an approximately linear voltage ramp, leading to simple linear electron deflection (Figure 1.11). The temporal resolution in this modality is mainly limited by the electronic jitter in the trigger signal from one sweep to the next, and accordingly a maximum resolution of ∼50 ps is attainable on any integrated measurement[*]. As such, the slow sweep unit was typically used in conjunction with the AOM for measurement of samples with decay lifetimes greater than ∼2 ns.

In contrast to the slow sweep unit, the voltage sweep provided by the synchroscan unit is sinusoidal with quasi-linear electron deflection being measured around the maximum voltage gradient (Figure 1.11). The benefit of such a scheme is that accurate control of the sinusoid frequency effectively eliminates sweep-to-sweep trigger jitter, thereby increasing the maximum attainable temporal resolution in integrated measurements to ∼1.9 ps (Figure 1.12). This increase in resolution comes at the reduction of the usable temporal window to ∼2 ns however due to the sweep non-linearity. Furthermore, the return-sweep arising from the oscillating voltage is typically not discarded and results in signal overlap. Therefore, PL decays with components significantly greater than 2 ns introduce return-sweep distortions. These can however be effectively compensated for in data post processing (see § 1.2.2.6).

Aside from installation, confirmation of correct operation and periodic main-

---

[*] It should be noted that in true single-shot measurements this can decrease to ∼20 ps

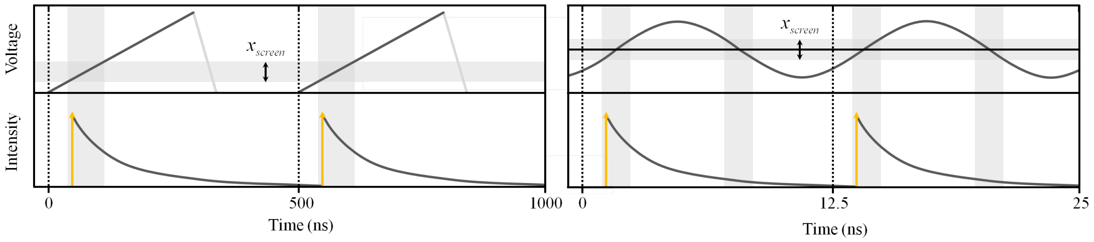

Figure 1.11: *Left panel:* Depiction of a typical linear voltage sweep provided by the streak camera slow sweep module (top), its relation to the sample excitation and fluorescence decay (bottom), and the phosphor screen dimension, x_{screen}. The time scales are slow enough to permit electronic deflection of the return-sweep (shown in light grey). *Right panel:* Corresponding typical sinusoidal voltage sweep provided by the streak camera synchroscan module. The time scales are too fast to permit return-sweep deflection and so cause signal overlap.

tenance, no significant development of the streak camera system was required.

Time correlated single photon counting detection was provided by a liquid nitrogen cooled Hamamatsu C9940-02 NIR fast PMT coupled to an Edinburgh Instruments TC11 TCSPC card. Triggering was once again provided by sampling of the Ti:Al_2O_3 oscillator output via the same stabilised photo-diode used for streak triggering. The high speed TCSPC card chosen permitted acquisition up to 80 MHz with maximum temporal resolutions of ∼100 ps. Aside from installation, confirmation of correct operation and periodic maintenance, no significant development of the TCSPC system was required.

1.2.2.6 Data Post-processing

To allow convenient and flexible post-processing of the multi-dimensional maps obtained using the TPL system, a custom software suite was developed for the MATLAB computing environment. Development in MATLAB was chosen so as to provide an inherently open source and cross-platform (Windows, Mac, Linux) compatible design, as well as allowing the significant graphical visualisation and interface strengths of the MATLAB environment to be leveraged. Furthermore, the unified interface provided by MATLAB to a multitude of existing numerical toolboxes makes future extension of processing and analysis features trivial. The software suite is entitled `trpl` and can currently be downloaded from http://code.google.com/p/ma-code/downloads/list. It it comprised of several command line modules so as to facilitate scripting for processing automation. Current features include;

- Import/Export
    - Load/save Hamamatsu ITEX file format (`*.img`), allowing full access to Streak camera measurement parameters and meta-data

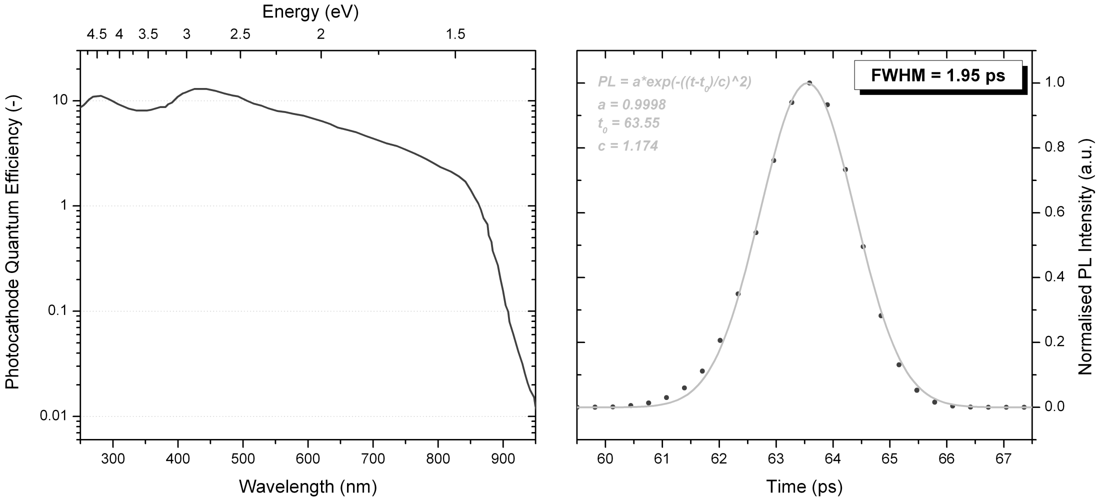

Figure 1.12: *Left panel:* Streak camera photo-cathode quantum efficiency [adapted from Hamamatsu test report] *Right panel:* Typical high resolution synchroscan integrated measurement instrument response

  - Load/save Edinburgh Instruments file formats (`*.fs`,`*.fl`), allowing full access to TCSPC measurement parameters and meta-data [under development]
  - Load/save ASCII formats (`*.txt`,`*.dat`, etc.), allowing analysis of generic data maps (e.g. TA data)
  - Export of integrated or single spectra/dynamics to ASCII files or Matlab workspace
  - Tools to facilitate automated export of integrated or single spectra/dynamics

- Correction
  - Correction of temporal dispersion arising from streak camera photo-electron collimation at high temporal resolutions
  - Automated rising edge detection and temporal scaling via an adaptive local regression fitting algorithm
  - Correction of background signals via reference image subtraction
- Fitting
  - Tight integration with the MATLAB `cftool` graphical fitting utility
  - Instrument temporal response function (experimental/theoretical) compensation via convolution with dynamics
  - Synchroscan return-sweep distortion compensation (see Figure 1.11 and discussion)

  - Signal ‘pile-up’ compensation (see § 1.2.2.2)

- Visualisation
  - Interactive data visualisation, exploration and manipulation via a user friendly GUI

Future development will be aimed at broader integration with the TA systems at the CNST to create a single common data processing and analysis platform.

1.3 Transient Absorption Systems

As mentioned previously, the transient absorption systems were principally developed by others (Srimath Kandada, Raavi, Grancini, Petrozza, Polli, Cerullo, Lanzani) and so shall not be discussed in detail. For the sake of completeness however, a brief description of the specific systems used in the investigations presented in this manuscript is given below. More detailed descriptions can be found in references 15, 16.

1.3.1 fs-Resolution TA System Description

An intra-cavity passive Kerr-lens mode-locked Ti:Al_2O_3 oscillator (Coherent Micra-18) operating at 80 MHz was used as a fundamental broadband source. This provided *sech*^{2} pulses with durations of ∼20 fs and a central wavelengths of 800 nm. A grating based pulse stretcher (Coherent 9040) was used to temporally expand the pulses before amplification in a 250 kHz actively Q-switched Ti:Al_2O_3 based regenerative amplifier (Coherent RegA 9000). The amplified pulses were subsequently temporally compressed in a grating based compressor (Coherent 9040), resulting in pulses with temporal widths of ∼35 fs and energies of ∼6 µJ. A thin beamsplitter was used to split the amplified output into pump and probe beams. The pump beam was input into a two-pass BBO-based collinear OPA (Coherent 9450), allowing spectral conversion to any desired wavelength in the 480 nm to 750 nm wavelength range with resulting temporal broadening to ∼120 fs. The probe beam was used for super-continuum generation [17] within a sapphire plate, leading to probe pulses with significant continuous spectral content from 480 nm to 1100 nm and temporal widths of ∼100 fs. Both pump and probe pulses were focussed and spatially overlapped in the sample space, with the temporal delay between them given by an optical retro-reflective delay line located on the pump arm of the system. Great care was taken to ensure the spot size of the probe beam was significantly smaller than that of the pump beam. The resulting probe signal — typically measured in transmission — was coupled into an Acton SP2300i imaging spectrograph and the dispersed signal was measured by a custom Stresing silicon based CCD linear array. Differential spectra were taken by modulation of

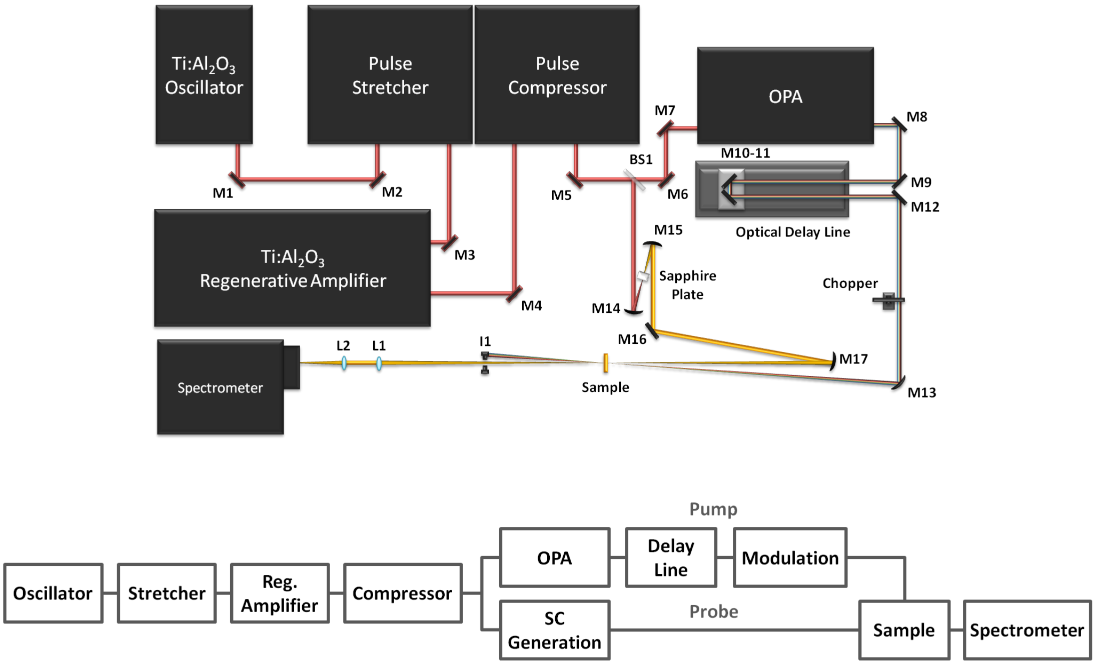
Ti:Al$_2$O$_3$ Oscillator
Pulse Stretcher
Pulse Compressor
OPA
M7
M8
BS1
M10-11
M9
M12
M1
M2
M5
M6
Optical Delay Line
M15
Ti:Al$_2$O$_3$ Regenerative Amplifier
M3
Sapphire Plate
Chopper
M4
M14
M16
M17
Spectrometer
L2
L1
I1
Sample
M13
Pump
Oscillator
Stretcher
Reg. Amplifier
Compressor
OPA
Delay Line
Modulation
SC Generation
Probe
Sample
Spectrometer

Figure 1.13: fs-TA system optical layout (top) and schematic (bottom). Abbreviated optical components; steering mirror (M), beam splitter (BS), alignment iris (I), lens (L)

the pump beam using a mechanical chopper operating at $250/(64 \cdot 2) = 1.95\,\text{kHz}$, so as to take couplets of ~50 spectra in pump-on and pump-off conditions*. Control of the different system components and data acquisition was performed by in-house software developed in LabVIEW.

1.3.2 ns-Resolution TA System Description

Transient absorption with ~10 ns temporal resolution was provided by an Edinburgh Instruments LP920 flash-photolysis system. Tunable excitation was achieved using a Nd:YAG pumped commercial OPO (Opotek OPOlette He 355 LD) yielding pulses of ~7 ns duration spanning the 410 nm to 2200 nm wavelength range. Xenon and QTH incandescent lamps provided broadband probe fields covering the UV-Visible and Visible-NIR spectral regions respectively. After interaction with the sample — typically in transmission or reflection geometries — the probe light was collected by a lens system and passed through a diffracting spectrograph. An Andor iStar intensified CCD coupled to one of the spectrograph outputs was used to collect gated spectra via fast (~1 ns) electronic gating. A set of fast PMTs (Hamamatsu R928, Hamamatsu G8605-23, Hamamatsu G5852-23, Hamamatsu G5853-23) with different response times coupled to the second

---

*Couplets of 50 and not 64 were taken so as to avoid potential issues arising from slight variations in chopper frequency

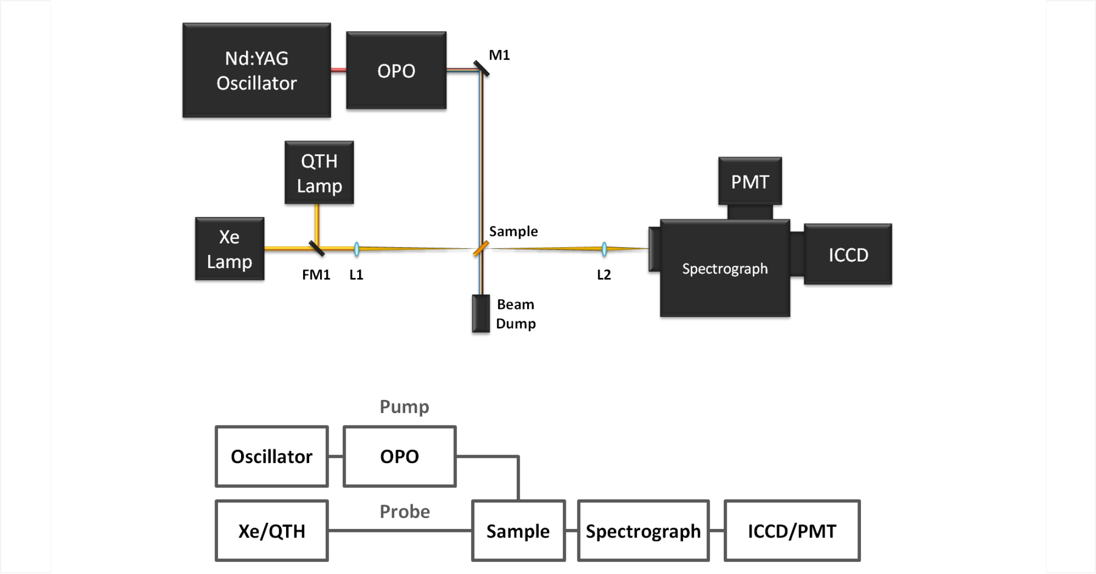
Nd:YAG Oscillator
OPO
M1
QTH Lamp
PMT
Xe Lamp
Sample
FM1
L1
L2
Spectrograph
ICCD
Beam Dump
Pump
Oscillator
OPO
Probe
Xe/QTH
Sample
Spectrograph
ICCD/PMT

Figure 1.14: ns-TA system optical layout (top) and schematic (bottom). Abbreviated optical components; steering mirror (M), flip mirror (FM), lens (L)

spectrograph output were used to collect dynamics of individual spectral bands via a 300 MHz bandwidth oscilloscope (TDS 3012C). Spectral selectivity in this case was provided by a motorised slit located after the gratings. Control of the different system components and data acquisition and processing was performed by a provided software suite (Edinburgh Instruments L900). An overall system resolution of ∼10 ns was obatined.

References

[1] N. V. Tkachenko, *Optical Spectroscopy: Methods and Instrumentations* (Elsevier Science, 2006), 1st ed., ISBN 0444521267.

[2] B. Valeur, *Molecular Fluorescence: Principles and Applications* (Wiley-VCH, 2001), 1st ed., ISBN 352729919X.

[3] J. R. Lakowicz, *Principles of Fluorescence Spectroscopy* (Springer, 2010), 3rd ed., ISBN 0387312781.

[4] A. Weiner, *Ultrafast Optics (Wiley Series in Pure and Applied Optics)* (Wiley, 2009), ISBN 0471415391.

[5] R. W. Boyd, *Nonlinear Optics* (2003), 2nd ed., ISBN 0121216829.

[6] G. Lanzani, *The Photophysics behind Photovoltaics and Photonics* (Wiley-VCH, Weinheim, 2012), 1st ed., ISBN 978-3-527-41054-5.

[7] C. Rullière, ed., *Femtosecond Laser Pulses: Principles and Experiments (Advanced Texts in Physics)* (Springer, 2004), 1st ed., ISBN 0387017690.

[8] A. Einstein, Mitteilungen der Physikalischen Gessellschaft Zürich **18**, 47 (1916).

[9] P. Hamm and M. Zanni, *Concepts and Methods of 2D Infrared Spectroscopy* (Cambridge University Press, 2011), 1st ed., ISBN 110700005X.

[10] S. Mukamel, *Principles of Nonlinear Optical Spectroscopy* (Oxford University Press, 1995), 1st ed., ISBN 0195092783.

[11] R. Thomson, C. Leburn, and D. Reid, eds., *Ultrafast Nonlinear Optics (Scottish Graduate Series)* (Springer, 2013), ISBN 3319000169.

[12] M. Zavelani-Rossi, G. Cerullo, S. D. Silvestri, L. Gallmann, N. Matuschek, G. Steinmeyer, U. Keller, G. Angelow, V. Scheuer, and T. Tschudi, Opt. Lett. **26**, 1155 (2001), URL `http://ol.osa.org/abstract.cfm?URI=ol-26-15-1155`.

[13] N. Dring, *Center for Nano Science and Technology* (2013), URL `http://cnst.iit.it/`.

[14] E. L. Malus, J. Ec. Poly. **7**, 1 (1808).

[15] A. R. S. Kandada, Doctoral thesis, Politecnico di Milano (2013).

[16] A. R. S. Kandada, G. Grancini, A. Petrozza, S. Perissinotto, D. Fazzi, S. S. K. Raavi, and G. Lanzani, Scientific Reports **3**, 2073 (2013), ISSN 2045-2322, URL `http://www.pubmedcentral.nih.gov/articlerender.fcgi?artid=3691563&tool=pmcentrez&rendertype=abstract`.

[17] M. Bradler, P. Baum, and E. Riedle, Applied Physics B **97**, 561 (2009), ISSN 0946-2171, URL `http://link.springer.com/10.1007/s00340-009-3699-1`.

Chapter 2

Transient Spectroscopic Investigations of Rubrene Single Crystals

Organic compounds — those composed primarily of carbon and hydrogen — are ubiquitous in both the natural and synthetic worlds. Many innovative applications have arisen from their highly flexible chemistry, however their insulating nature at standard temperature and pressure long precluded their use in electronic applications. This changed upon the discovery that sp^2 hybridized conjugated organic systems with delocalised π electron orbitals had significant semiconducting [1], conducting [2] or even superconducting properties [3]. Since then, there has been rapid and significant research progress into understanding this multi-faceted class of materials and bringing their unique properties to electrical and electronic applications.

Foremost amongst these has been the search for organic materials suitable for opto-electronic applications, where their low cost, light-weight, and large-scale deposition has the potential to revolutionise sectors such as photovoltaics (PV) and lighting. Despite the fast pace of progress, the understanding of the fundamental properties of many organic conjugated systems is hindered by significant structural disorder which can frequently dominate electronic and optical properties. Such disorder is often rooted in the polymeric, amorphous or polycrystalline morphology resulting from low-temperature deposition methods. Recently however, great advances have been made in single-crystal growth techniques of many small organic molecules, thereby eliminating disorder and greatly facilitating fundamental studies and understanding.

One such recently crystallised molecule is the polycyclic aromatic hydrocarbon 5,6,11,12-tetraphenyltetracene — more commonly referred to as Rubrene — whose high quality crystallisation has only been achieved in the last decade [4]. Rubrene single crystals have been shown to have excellent charge carrier mobilities, with record hole-mobilities of $20\,\mathrm{cm^2\,V^{-1}\,s^{-1}}$ being demonstrated [5] which has led to it becoming a prototypical system for organic electronic research. The strong interaction of Rubrene with visible light also opens the possibility of its use in PV applications. Indeed recent indications of long-range photo-generated exciton diffusion and claims of efficient singlet fission have led to a spate of research into its PV potential [6]. Many photophysical aspects of Rubrene remain unclear and under debate however, and a thorough understanding of these is crucial for successful exploitation of this promising material. Of particular note is a spurious yet often dominant low-energy emission peak whose origin has not yet been identified. Furthermore, whilst device based measurements indirectly imply the presence of efficient singlet fission in Rubrene crystals, there is scant spectroscopy evidence for it in the bare material.

In this chapter, we present transient spectroscopic investigations of Rubrene single crystals with an aim to clarifying these two points.

2.1 Background

By way of introduction and background to the experimental work performed on Rubrene, a brief recap of the pertinent topics in the field of conjugated organic opto-electronics is presented in this section. This is by no means comprehensive and interested readers are instead referred to other texts such as those in references 7–12.

2.1.1 Molecules

2.1.1.1 Conjugated Molecules

Most of the colours found in the natural world arise from conjugated systems — organic molecules with alternating single and double bonds. Their coloured nature implies a strong interaction with light which can be understood by consideration of the covalent bonding holding them together. Bonding between atoms is dictated by atomic orbital overlap, with the overlap of n atomic orbitals yielding n molecular orbitals often extending over the entire molecule. Such molecular orbitals have differing energies due to constructive and destructive interference, resulting in bonding and anti-bonding molecular states. The energetic splitting of these states can be partly understood as the amount of orbital overlap, with strongly overlapping orbitals leading to large energy differences (strong bonding) and weakly overlapping orbitals leading to small energy differences (weak bonding).

Carbon has a $1s^2, 2s^2, 2p^2$ electronic configuration and as such can undergo sp^2 hybridisation of its $2s$ and $2p_{x,y}$ atomic orbitals to form planar trigonal hybrid orbitals [8]. Hybrid orbitals on adjacent carbon atoms exhibit strong in-plane overlap, forming a strong bond — termed a σ-bond — with associated large state

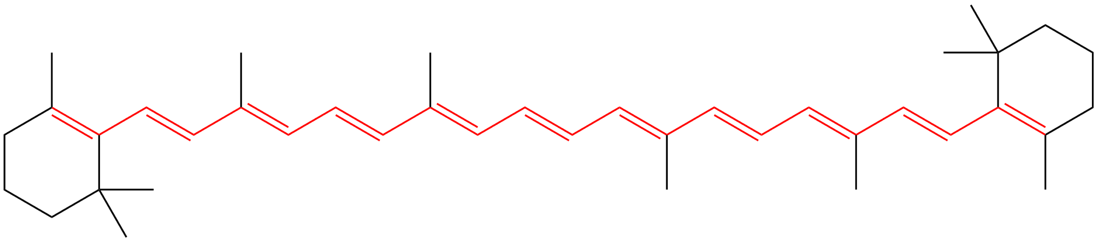

Figure 2.1: An example of a conjugated molecule (beta-carotene). The conjugated section is highlighted in red [adapted from 13, public domain]

energy splitting. The remaining out of plane $2p_z$ orbitals exhibit only a weak overlap and so form weak delocalised bonds — termed π-bonds — above and below the σ plane with associated small state energy splitting. Isolated σ-bonds are referred to as single bonds, whilst the combination of σ- and π-bonds are referred to as double bonds. The alternating single and double bonds in conjugated systems mean each carbon atom contributes one electron to the delocalised π system. This results in the highest occupied molecular orbital (HOMO) being a π bonding state, with the subsequent lowest unoccupied molecular orbital (LUMO) being the corresponding π anti-bonding state. Given the small energetic splitting between these two states — typically of a few eV — conjugated systems can exhibit semiconducting or even conducting properties. The location of the transition energies within the visible spectrum lends conjugated systems their spectacular colours and makes this wide family of materials of great interest for consideration of light-organic-matter interactions.

2.1.1.2 Electronic Structure of Molecules

An understanding of the opto-electronic properties of a molecular system can be gained from knowledge of its electronic structure. This in turn can be obtained from diagonalisation of the appropriate system Hamiltonian. The full Hamiltonian, $\hat{H}$, for any molecular system can be expressed as

$$\hat{H} = \hat{T}_N + \hat{T}_e + \hat{V}_{NN} + \hat{V}_{Ne} + \hat{V}_{ee} \; , \tag{2.1}$$

where $\hat{T}_N$ and $\hat{T}_e$ are the kinetic energies of the nuclei and electrons respectively, and $\hat{V}_{NN}$, $\hat{V}_{Ne}$ and $\hat{V}_{ee}$ are the nuclear-nuclear, nuclear-electron and electron-electron Coulomb potentials. For a molecular system comprised of N nuclei and

n electrons, the operators in (2.1) be written more explicitly as

$$\hat{T}_N = -\frac{\hbar^2}{2}\sum_{I=1}^{N}\frac{1}{M_I}\nabla_I^2 \tag{2.2a}$$

$$\hat{T}_e = -\frac{\hbar^2}{2}\sum_{i=1}^{n}\frac{1}{m_i}\nabla_i^2 \tag{2.2b}$$

$$\hat{V}_{NN} = \frac{e}{4\pi\epsilon_0}\sum_{I=1}^{N}\sum_{J>I}^{N}\frac{Z_I Z_J}{R_{IJ}} \tag{2.2c}$$

$$\hat{V}_{Ne} = -\frac{e}{4\pi\epsilon_0}\sum_{I=1}^{N}\sum_{i=1}^{n}\frac{Z_I}{R_{Ii}} \tag{2.2d}$$

$$\hat{V}_{ee} = \frac{e}{4\pi\epsilon_0}\sum_{i=1}^{n}\sum_{j>i}^{n}\frac{1}{r_{ij}}\ , \tag{2.2e}$$

where Z_I is the atomic number of nucleus I, R_{IJ}, R_{Ii} and r_{ij} are the nuclear-nuclear, nuclear-electron and electron-electron separations between nuclei I, J and electrons i, j respectively, and e is the elementary charge.

Equation 2.2 therefore contains both nuclear and electronic components with the large number of cross terms preventing direct separation and meaning that analytical solutions exist only for the hydrogen atom. This reflects the fact that both nuclei and electrons can move and have associated potentials, meaning that any change in the electronic configuration of the system can affect the position of the nuclei. This in turn can affect the potential felt by the electrons and therefore their configuration.

Given this complex interplay between nuclear and electronic sub-systems, simplifications are necessary to yield the problem tractable. Key amongst these is the adiabatic Born-Oppenheimer approximation (BOA) where the motion of the nuclei is assumed to be far slower than that of the electrons due to their significantly higher mass. Within this approximation, the electrons are taken to react immediately to any nuclear motion, and so move within the potential defined by the instantaneous nuclear coordinates. The key mathematical result of the BOA is to allow the total molecular wavefunction, ψ, to be separated into nuclear and electronic components χ and ϕ respectively,

$$\psi_{kK}(\mathbf{r}_i, \mathbf{R}_I) = \phi_k(\mathbf{r}_i; \mathbf{R}_I)\chi_K(\mathbf{R}_I)\ , \tag{2.3}$$

where the notation $\phi_k(\mathbf{r}_i; \mathbf{R}_I)$ denotes the functional dependence of the electronic wavefunction on the nuclear coordinates, $\mathbf{R}_I$.

It can be shown [14] that substitution of Equation 2.3 into the time-independent Schrödinger equation containing the Hamiltonian 2.1 yields sub-system separation into two coupled equations describing the electronic and nuclear components[*],

$$\left[\hat{T}_e(\mathbf{r}_i) + \hat{V}_{ee}(\mathbf{r}_{ij}) + \hat{V}_{Ne}(\mathbf{r}_i;\mathbf{R}_I)\right]\phi_k(\mathbf{r}_i;\mathbf{R}_I) = \varepsilon_k(\mathbf{R}_I)\phi_k(\mathbf{r}_i;\mathbf{R}_I) \tag{2.4a}$$

$$\left[\hat{T}_N(\mathbf{R}_I) + \hat{V}_{NN}(\mathbf{R}_{IJ}) + \varepsilon_k(\mathbf{R}_I)\right]\chi_K(\mathbf{R}_I) = \epsilon_K\chi_K(\mathbf{R}_I)\ . \tag{2.4b}$$

The first step of the BOA involves repeated solution of the electronic equation (2.4a) under slow variation of the nuclear coordinates $\mathbf{R}_I$, to yield the electronic potential surfaces, $\varepsilon_k(\mathbf{R}_I)$. Such solution is generally very complex due to the presence of the electron-electron repulsion potentials, $\hat{V}_{ee}(\mathbf{r}_{ij})$. Further simplifications are therefore made at this point, and several analytical and numerical methods have been used to treat these interactions to differing degrees of accuracy (e.g. Hartree-Fock, density functional theory, *etc.*).

Once solved, the electronic potential energy surfaces found are used as the nuclear-electron and electron-electron potentials in the nuclear equation (2.4b). Additionally, the nuclear-nuclear potentials in Equation 2.4b, representing the bonding between atoms, must be defined. Many degrees of freedom can be treated by these interactions, but the nuclear vibrational motion can generally be considered dominant. As such, common choices for $\hat{V}_{NN}(\mathbf{R}_{IJ})$ are the harmonic potential — i.e. parabolic — or the somewhat more realistic Morse potential which takes bond breaking into account [15]. Subsequent solution of the nuclear equation therefore often results in stationary nuclear states with approximately equal energy spacings.

Equations 2.4 show how within the BOA, each electronic state, k, yields a different electronic potential energy surface, ε_k, and so different nuclear Hamiltonians. The result of this is the formation of a manifold of nuclear sub-levels within each electronic level (Figure 2.2). Furthermore, the different electronic potential energy surfaces can yield different equilibrium positions for nuclear vibrations. The total energy of the final state — termed a vibrational-electronic, or vibronic state — is simply given by the sum of the electronic and nuclear energies $\varepsilon_k(\mathbf{R}_I)$ and ϵ_K respectively.

When calculating the electronic structure of conjugated molecules, there may be dozens or even hundreds of atoms to consider, making accurate *ab initio* calculation prohibitively computationally expensive. The strong binding of the carbon inner atomic orbitals and σ-bonded orbitals means however that they play a small role in the optical properties of the molecule. As such, they can be safely subsumed into simplifying approximations during computations of optical interest and full treatment of only the π electron interactions is required.

---

[*] The effect of the nuclear-nuclear potential $\hat{V}_{NN}(\mathbf{R}_{IJ})$ on the electronic sub-system is typically neglected and so the wavefunctions $\phi_k(\mathbf{r}_i;\mathbf{R}_I)$ and $\chi(\mathbf{R}_I)$ are not strictly eigenfunctions of the Hamiltonian (2.1)

2.1.1.3 Optical Transitions

The interaction of an electromagnetic wave with a quantum system can be treated using time-dependent perturbation theory. For a monochromatic plane wave of frequency ω_0, Fermi showed that the probability — and thus rate, $k_{i\to f}$ — of a transition from a state ψ_i to a state ψ_f separated by an energy $\hbar\omega_0$ via absorption of a photon is

$$k_{i\to f} \propto |\langle\psi_f|\hat{H}'_{\omega_0}|\psi_i\rangle|^2 \; , \tag{2.5}$$

with the perturbation operator, $\hat{H}'_{\omega_0}$, usually taken as the amplitude scaled electric dipole operator, $E_0\hat{\mu}$,

$$E_0\hat{\mu} = |E_0|e\hat{\mathbf{r}}\mathbf{q} \; , \tag{2.6}$$

defined by the dipole separation position operator, $\hat{\mathbf{r}}$, unit polarisation vector, $\mathbf{q}$, and elementary charge, e. Neglect of the magnetic component of the electromagnetic wave is justified by its vastly lower strength. A dipole interaction is usually considered as it is the simplest description of the interaction between an field and a charged particle, however other more precise interaction forms such as quadrupole interactions can also be treated.

Substitution of 2.6 into 2.5 then yields

$$\begin{aligned} k_{i\to f} &\propto |E_0 e\langle\psi_f|\hat{\mathbf{r}}\mathbf{q}|\psi_i\rangle|^2 && \text{(2.7a)} \\ &\propto |E_0\mu_{i\to f}|^2 \; , && \text{(2.7b)} \end{aligned}$$

showing that the optical transition rate between initial and final states is proportional to the square of the transition dipole moment, $\mu_{i\to f} = e\langle\psi_f|\hat{\mathbf{r}}\mathbf{q}|\psi_i\rangle$. Calculation of $\mu_{i\to f}$ therefore requires knowledge of the initial and final state wavefunctions and computation of their perturbed inner product in Hilbert space. As such, inner product arguments which are anti-symmetric with respect to spatial inversion will yield vanishing transition dipole moments. Observation that the dipole operator is spatially anti-symmetric therefore enables facile distinction between allowed and disallowed transitions based solely on knowledge of the spatial symmetry of the initial and final states. More specifically, the spatial components of the initial and final state wavefunctions must be of opposite symmetry in order to result in an even integrand and non-vanishing $\mu_{i\to f}$[*]. It should be noted that other selection rules dependent on further components of the initial and final wavefunctions (e.g. spin) may also apply.

The optical excitation of a conjugated molecule results in a perturbation of the ground state electronic configuration. New potentials such as those in equations (2.2c–2.2e) must therefore be considered in order to accurately describe the excited molecule and calculate the excited state wavefunctions. Fortunately, the small electronic/nuclear mass ratio once again allows simplifying assumptions to be made without great sacrifices in accuracy. The Franck-Condon (FC) approximation is one such approximation widely used for optical transitions. It assumes that the electrons react instantly to optical excitation, before nuclear motion can occur. Within the BOA, this is mathematically equivalent to operation of the dipole operator on the electronic part of the BO wavefunction only. The resulting transition rate, $k_{i\to f}$, can therefore be shown to be

---

[*] Recall: $\bar{\sigma}\cdot\bar{\sigma} = \sigma, \sigma\cdot\bar{\sigma} = \bar{\sigma}, \bar{\sigma}\cdot\sigma = \bar{\sigma}, \sigma\cdot\sigma = \bar{\sigma}$, where σ and $\bar{\sigma}$ denote symmetric and anti-symmetric functions respectively

$$\begin{aligned} k_{i\to f} &\propto |E_0 e\langle\chi_f|\langle\phi_f|\hat{\mathbf{r}}\mathbf{q}|\phi_i\rangle|\chi_i\rangle|^2 &\text{(2.8a)}\\ &\propto |E_0\langle\chi_f|\chi_i\rangle\mu^e_{i\to f}|^2 \,. &\text{(2.8b)}\end{aligned}$$

The squared inner product of the nuclear wavefunctions are known as Franck-Condon factors and can be seen to modulate the electronic transition dipole moment, $\mu^e_{i\to f} = e\langle\phi_f|\hat{\mathbf{r}}\mathbf{q}|\phi_i\rangle$. If the ground and excited state nuclear wavefunctions are identical, their orthogonality leads to a vanishing transition dipole moment for different vibrational levels — i.e. $\langle\chi_{K'}|\chi_K\rangle = \delta_{KK'}$ — and so only transitions between states with the same vibrational index are allowed. Recalling that within the BOA the nuclear wavefunctions depend on the electronic configuration via the electronic potential energy surfaces, it is clear that the nuclear potential governing ground and excited states are rarely the same. As such, no such orthogonality exists between ground and excited state nuclear wavefunctions, the FC factors become non-zero modulation terms, and transitions between vibrational levels of different indices are permitted (Figure 2.2).

In most conjugated systems, the typical separation between vibrational sub-levels is significantly larger than the average thermal energy at room temperature (∼25 meV) and so only the lowest vibrational level of the ground state is generally populated. In the case of non-identical ground and excited nuclear wavefunctions, the FC factors are accordingly non-zero and photon absorption leads to a series of transitions to the multiple vibrational sub-levels of the excited electronic state — e.g. from the ground state, ψ_{00} to the vibronic levels of the first excited state ψ_{1K} (see Equation 2.3). The resulting absorption spectrum exhibits a series of maxima which can be seen to be roughly equally spaced in energy due to the approximately harmonic nature of the nuclear potentials. Such an absorption feature is commonly referred to as a vibronic progression. The amplitude modulation of the progression is determined in part by the appropriate FC factors, although it can be shown that other selections rules (e.g. spin, electronic selection, etc.) have a far greater comparative modulation strength.

Higher vibrational sub-levels of the excited state can therefore be directly populated by photon absorption, however vibrational relaxation through phonon emission quickly restores thermal equilibrium, resulting in population of the lowest vibronic state only. This vibrational relaxation is typically a much faster process than spontaneous photon emission, and as such, PL almost always occurs

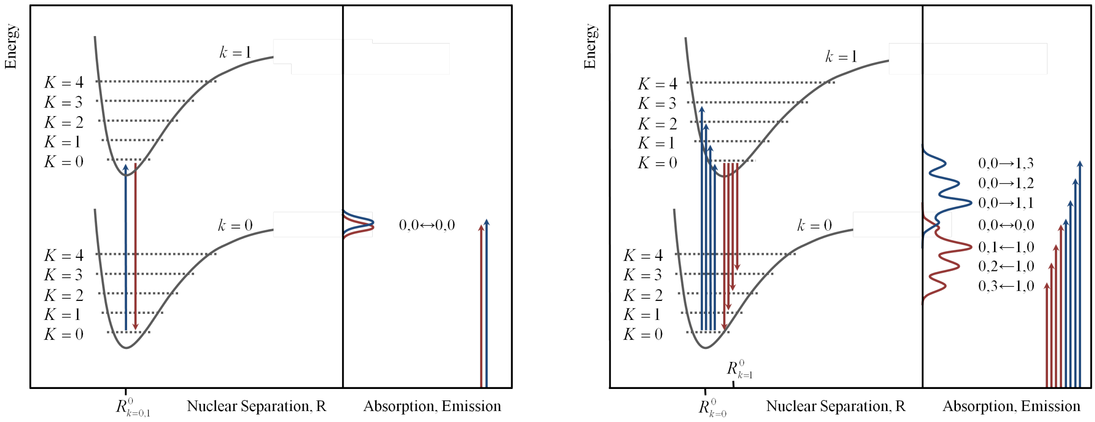

Figure 2.2: *Left panel:* Vibronic states in molecular systems, showing the manifolds of nuclear sub-levels (indexed by K) within each electronic level (indexed by k). For identical ground and excited state nuclear wavefunctions, the Franck-Condon factors are equal to zero and so only transitions between vibronic levels with the same vibrational index, K, are allowed. *Right panel:* For the more common case of differing nuclear wavefunctions, non-zero Franck-Condon factors permit transitions between levels with different vibrational indices. The approximately constant spacing of the vibrational sub-levels leads to the formation of vibronic progressions in absorption and emission

from the lowest vibrational sub-level of the excited state*. Just as with absorption, emission to the ground state is governed by the transition dipole moment. Thus, inequality of the excited and ground state nuclear potentials leads to FC allowed transitions to all the vibrational sub-levels of the electronic ground state — e.g. from the lowest vibrational sub-level of the first excited state, ψ_{10}, to the vibronic levels of the ground state, ψ_{0K}. A vibronic progression is therefore also seen in emission spectra, with spacing between maxima dictated by the energy spacing of the ground state vibrational sub-levels.

As depicted in Figure 2.2, a direct consequence of vibrational relaxation is that the highest emission transition energy will always be lower than the lowest absorption transition energy. The energy difference between these two transitions is termed the Stokes shift and is directly related to the degree of vibrational relaxation. Frequently, the ground and excited state geometries of a molecule are quite similar resulting in approximately equal FC factors and vibrational sub-level spacings for both ground and excited states. In this case, the resulting absorption and emission spectra are approximately mirror images of one another.

2.1.1.4 Neutral Excited States

The optical excitation of conjugated systems results in the promotion of an electron to the LUMO, leaving a positively charged 'hole' in the HOMO. Their opposite charge and spatial correlation along with the low dielectric constant of most organic materials means that the electron and hole exhibit strong coulombic attraction. As such, the interacting electron-hole pair can be considered as a neutrally charged quasi-particle; an exciton. Given the attractive potential between the two particles, additional energy — referred to as the exciton binding energy — must be provided in order to dissociate the exciton into an uncorrelated electron and hole. For this reason, exciton states are always located at energies lower than the HOMO-LUMO energy difference.

---

*This empirical observation is sometimes referred to as Kasha's rule [16]

Whilst ubiquitous in conjugated systems, it should be noted that excitons are by no means unique to organic materials, and can also be found in a wide variety of inorganic materials, including those which are ionically bound. In these cases however, the high dielectric constant of the material effectively screens the coulombic interaction, resulting in less correlation between the electron and hole and therefore smaller binding energies. As such, a spectrum of excitons with different electron-hole interaction strengths can be thought to exist. At one end are tightly bound (high binding energy) excitons with small electron-hole separations and a resulting typical spatial extent of less than one molecule. Such excitons are known as molecular Frenkel excitons and are typical of the neutral excitations found in organic systems comprised of light nuclei. At the other end of such a spectrum are weakly bound (low binding energy) excitons with large electron-hold separations and a resulting spatial extent of several molecules/atoms. These are known as Wannier-Mott excitons and can typically be found in inorganic systems with heavy nuclei.

Given that excitons arise from the interaction of two spin 1/2 particles — viz. an electron in the LUMO and hole[*] in the HOMO — the description of an exciton requires consideration their spin combination. Following the standard SU(2) addition operations, two spin 1/2 particles can be combined into four different spin states; one with a total spin equal to zero — referred to as the singlet spin state — and three with a total spin equal to one — referred to as triplet spin states (Table 2.1). Excitons can therefore be categorised according to their total spin, forming singlet and triplet exciton spin manifolds.

The singlet and triplet exciton states are generally not degenerate, but tend instead to be split by an exchange energy arising from HOMO-LUMO electron interactions. In conjugated systems, the magnitude of this interaction is principally determined by the spatial overlap of the HOMO-LUMO wavefunctions and typically acts to lower the energy of the triplet states below that of the singlet state. The individual triplet states are further split by spin coupling interactions — most predominantly spin-orbit coupling — however the effect of this on the optical properties is small and so is generally neglected.

Inspection of Table 2.1 shows that the spin component of the exciton wavefunc-

---

[*] Given that the spin of the hole is correlated to the spin of the electron occupying the HOMO by the Pauli exclusion principle, the spin interaction of the electron pair can be equivalently considered

Wavefunction		Spin		
Spatial	Spin	Total	z-component	Nomenclature
$2^{-1/2}\left(\psi_{A1}\psi_{B2} - \psi_{A2}\psi_{B1}\right)$	$\uparrow_1\uparrow_2$	1	1	Triplet
	$2^{-1/2}\left(\uparrow_1\downarrow_2 + \downarrow_1\uparrow_2\right)$	1	0	
	$\downarrow_1\downarrow_2$	1	-1	
$2^{-1/2}\left(\psi_{A1}\psi_{B2} + \psi_{A2}\psi_{B1}\right)$	$2^{-1/2}\left(\uparrow_1\downarrow_2 - \downarrow_1\uparrow_2\right)$	0	0	Singlet

Table 2.1: Exciton wavefunctions showing both spatial and spin components and the resulting subdivision into total spin manifolds. The spatial parts of the single particle Hamiltonian eigenfunctions are denoted ψ_A and ψ_B, such that ψ_{A1} denotes particle one in the single particle A eigenstate, and so on. Similarly, the eigenfunctions of the spin operator are denoted $\uparrow$ and $\downarrow$, corresponding to a spin z-component of $+\hbar$ and $-\hbar$ respectively

tion is symmetric and anti-symmetric under particle interchange for triplets and singlet excitons respectively. Having integer total spin, all excitons are described by Bose-Einstein statistics, and so must have total wavefunctions which are symmetric under particle interchange. This implies that the spatial components of the exciton wavefunctions for triplet and singlet excitons are also symmetric and anti-symmetric respectively. It follows therefore that the exciton ground state, S_0 — corresponding to the absence of an exciton and therefore synonymous with the electronic ground state — is always spatially symmetric. As described in § 2.1.1.3, optical transitions are therefore only permitted between the ground state and the singlet exciton manifold. It follows that radiative decay from the triplet manifold to the ground state is forbidden, meaning that triplet excitons tend to be long-lived.

Transitions between the two exciton spin manifolds — a process referred to as intersystem crossing (ISC) — requires a change of total exciton spin. This is often mediated by electron spin-orbit (SO) coupling, which acts to mix the spin character of the exciton states through a perturbing SO Hamiltonian, $\hat{H}_{SO}$ [17],

$$\hat{H}_{SO} = \alpha \sum_{I=1}^{N} \sum_{i=1}^{n} \frac{Z_I}{R_{Ii}^3} \hat{\mathbf{L}}_i \cdot \hat{\mathbf{S}}_i \ . \tag{2.9}$$

In this expression, α is the fine structure constant, $\hat{\mathbf{L}}_i$ and $\hat{\mathbf{S}}_i$ are the orbital and spin total angular momentum operators respectively, and all other quantities are as previously defined in Equations 2.2. From this, the effect of SO coupling, and therefore the rate of ISC, can be seen to depend on the atomic number of the nuclei present in the system. Intersystem crossing is therefore faster (i.e. more probable) in molecules containing heavy nuclei than those containing only light nuclei, such as pure hydrocarbons.

A particular case of ISC is the radiative transition between a triplet state and the singlet ground state, S_0 — a transition typically forbidden by spatial symmetry in the absence of ISC. The resulting long-lived (µs–ms) emission is termed phosphorescence, distinguishing it from the fast (ps–ns) fluorescence from singlet states.

2.1.1.5 Charged Excited States

The presence of excess charges in organics systems can lead to significant distortion of the molecular geometry due to the low dielectric constant of these materials[*]. The charge and associated deformation can be described as a quasi-particle termed a polaron.

Within a molecular picture, the nuclear potential for an ionised molecule can be significantly different to the ground state nuclear potential, and frequently exhibits a different equilibrium geometry and separation. In this case, ionisation taking place via FC transitions occur from the ground state equilibrium position to the ionised state non-equilibrium position and are necessarily followed by vibrational relaxation (Figure 2.3). The total ionisation energy, $\varepsilon_{\text{IP-rel}}$, therefore contains the relaxational loss energy, ε_{rel}.

An alternative ionisation scenario is deformation of the ground state nuclear geometry followed by a FC transition directly to the ionised state equilibrium position (see Figure 2.3). Whilst this requires an initial distortion energy, ε_{dis}, it results in lower transition energy, $\varepsilon_{\text{IP-dis}}$, and thus is often more energetically favourable. A polaron is just such a molecular distortion associated with an excess of charge. The energy required to return the molecule to its ground state equilibrium position is termed the polaron binding energy and is equal to the relaxational energy ε_{rel}.

It should be noted that for this picture to be valid, the ionization must be localised to a molecular site rather than a delocalised state. The resulting reduction in ionisation energy is therefore a local effect and is seen within the system ensemble as the emergence of two populated intra-gap (i.e. between HOMO-LUMO) polaron states. The symmetries of the polaron states result in allowed and forbidden optical transitions to and from them.

2.1.2 Molecular Crystals

The theoretical basis presented in § 2.1.1 implicitly assumes consideration of a system comprised of a single molecule or an ensemble of isolated non-interacting molecules. Whilst this is an accurate description for molecules in the gas and to some extent liquid phases, it is not a valid representation of molecules in the solid phase where inter-molecular van der Waals' interactions — weak as they may be — act to couple the molecules and introduce a communal system response.

---

[*] This ability to deform the surrounding nuclear environment is a direct manifestation of the strong electron-phonon coupling present in these systems

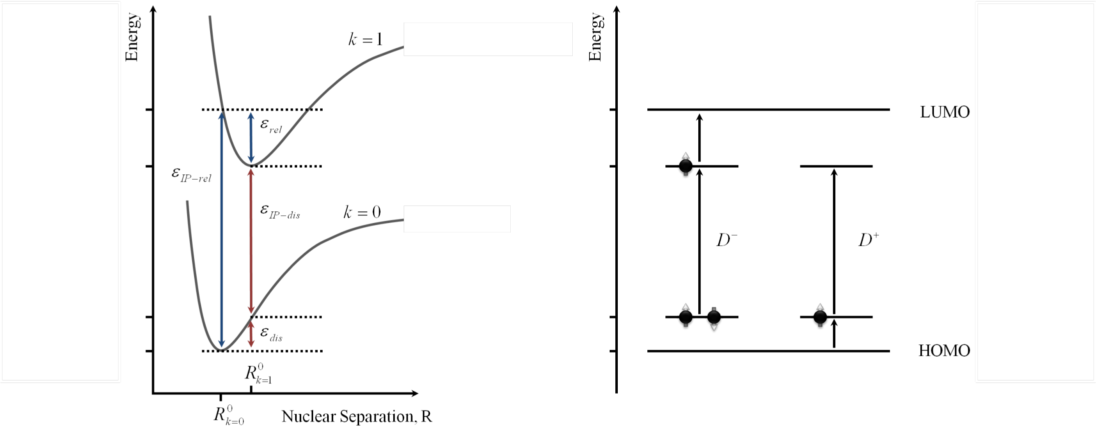

Figure 2.3: *Left panel:* Depiction of the energies involved in molecular ionisation in equilibrium (blue) and distorted (red) geometries. *Right panel:* The resulting local polaron states, D^- and d^+, as intra-gap states within the ensemble molecular electronic structure. Optically allowed transitions to/from the polaron states are also depicted (solid arrows) [adapted from 18]

The canonical example of a molecular solid is a molecular crystal, where molecules are arranged in an ordered lattice. The periodicity imposed by the crystal lattice makes molecular crystals easier to treat theoretically than their disordered amorphous counterparts, but conversely, more experimentally challenging to grow. A basic theory of excitations in molecular crystals is presented below.

2.1.2.1 Electronic Structure of Dimers

The theoretical treatment of inter-molecular interactions is best demonstrated by consideration of the limiting case of interaction between two identical molecules — viz. a physical dimer. The total Hamiltonian for such a system is given by the sum of the individual molecular Hamiltonians, $\hat{H}_1$ and $\hat{H}_2$, and an additional potential, $\hat{V}_{12}$, describing the inter-molecular interactions,

$$\hat{H} = \hat{H}_1 + \hat{H}_2 + \hat{V}_{12} \; . \tag{2.10}$$

It can be shown [7, Ch. D] that diagonalisation of this Hamiltonian results in a dimer ground state wavefunction[*], ψ^0, and energy, ε^0, given by

$$\psi^0 = \psi_1^0 \psi_2^0 \tag{2.11a}$$

$$\varepsilon^0 = \varepsilon_1^0 + \varepsilon_2^0 + D^0 \; , \tag{2.11b}$$

with,

$$D^0 = \langle \psi_1^0 \psi_2^0 | \hat{V}_{12} | \psi_1^0 \psi_2^0 \rangle \; , \tag{2.11c}$$

---

[*] For simplicity, vibrational and spin wavefunction components have been neglected

where ψ_1^0, ψ_2^0 and ε_1^0, ε_2^0 are the ground state wavefunctions and energies of molecules 1 and 2 respectively. The final term in Equation 2.11b shows how the inclusion of inter-molecular interactions intimately links the properties of the two molecules, resulting in a shift of the dimer ground state energy by an amount, D^0, referred to as the ground state Coulomb interaction energy (Figure 2.4).

A similar interaction effect can also be shown for the lowest lying dimer excited states, where the single molecule excited states undergo a Coulomb shift before being subsequently split into two non-degenerate dimer excited states. These two dimer excited state wavefunctions, $\psi_\pm^*$, and energies, $\varepsilon_\pm^*$, are given by [7, Ch. D]

$$\psi_\pm^* = 2^{-1/2}\left(\psi_1^*\psi_2^0 \pm \psi_1^0\psi_2^*\right) \tag{2.12a}$$

$$\varepsilon_\pm^* = \varepsilon_1^0 + \varepsilon_2^* + D^* \pm I_{12} \ , \tag{2.12b}$$

with,

$$D^* = \langle\psi_1^*\psi_2^0|\hat{V}_{12}|\psi_1^*\psi_2^0\rangle = \langle\psi_1^0\psi_2^*|\hat{V}_{12}|\psi_1^0\psi_2^*\rangle \ , \tag{2.12c}$$

and,

$$I_{12} = \langle\psi_1^*\psi_2^0|\hat{V}_{12}|\psi_1^0\psi_2^*\rangle \ , \tag{2.12d}$$

where ψ_1^*, ψ_2^* and ε_1^*, ε_2^* refer to the single molecule excited state wavefunctions and energies respectively. In an analogous fashion to the ground state, an excited state Coulomb interaction energy, D^*, shifts the excited states. Furthermore, the resonance interaction energy, I_{12}, acts to split the equivalent molecular excited states two into non-degenerate dimer excited states (Figure 2.4). The corresponding dimer excited state wavefunctions are linear combinations of the molecular ground and excited state wavefunctions, demonstrating that the excitation energy is no longer localised on a specific molecule, but is rather shared coherently between the two interacting molecules in a super-molecular excited state. The formation of delocalised states is a key consequence of intermolecular interactions.

The transition dipole moment between dimer states, $\mu^{0\to\pm}$, is simply given by a linear vector combination of the molecular transition dipole moments, $\mu_1^{0\to*}$ and $\mu_2^{0\to*}$. For transitions from the dimer ground to excited states, this is therefore

$$\mu^{0\to\pm} = 2^{-1/2}\left(\mu_1^{0\to*} \pm \mu_2^{0\to*}\right) \ . \tag{2.13}$$

The dimer transition dipole moment is therefore dependent on the relative orientations of the monomer molecules. For the specific case of translationally equivalent molecules, the molecular transition dipole moments are aligned either parallel or anti-parallel to one another, resulting in a vanishing transition probability to one of the dimer states. For non-translationally equivalent molecules, both states can be optically active with transitions strengths determined by the relative orientation of the molecular transition dipole moments.

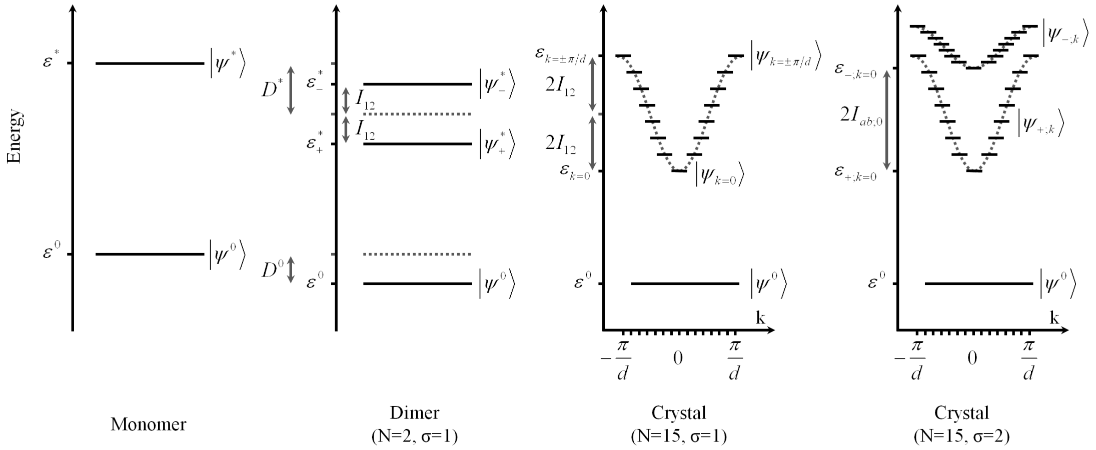
Energy
ε^*
$|\psi^*\rangle$
ε^0
$|\psi^0\rangle$
D^*
D^0
ε^*_-
ε^*_+
I_{12}
I_{12}
$|\psi^*_-\rangle$
$|\psi^*_+\rangle$
ε^0
$|\psi^0\rangle$
$\varepsilon_{k=\pm\pi/d}$
$2I_{12}$
$2I_{12}$
$\varepsilon_{k=0}$
$|\psi_{k=\pm\pi/d}\rangle$
$|\psi_{k=0}\rangle$
ε^0
$|\psi^0\rangle$
k
$-\frac{\pi}{d}$
0
$\frac{\pi}{d}$
$\varepsilon_{-,k=0}$
$2I_{ab;0}$
$\varepsilon_{+,k=0}$
$|\psi_{-,k}\rangle$
$|\psi_{+,k}\rangle$
ε^0
$|\psi^0\rangle$
k
$-\frac{\pi}{d}$
0
$\frac{\pi}{d}$
Monomer
Dimer
(N=2, σ=1)
Crystal
(N=15, σ=1)
Crystal
(N=15, σ=2)

Figure 2.4: Schematic of the electronic structure of a molecular monomer, its corresponding dimer, and corresponding linear crystals with one and two translationally inequivalent molecules per unit cell. The relevant energies (ground and excited state Coulomb energies, D_0 & D_*, resonance interaction energy, I_{12}, Davydov splitting energy, $2I_{ab;0}$) are shown in each case

2.1.2.2 Electronic Structure of Linear Molecular Crystals

The physical dimer formulation can be easily extended to the case of a one-dimensional linear crystals, where N translationally equivalent molecules are arranges in a linear lattice defined by a spacing, d. In direct analogy to the physical dimer, The total Hamiltonian for the this system is given by the sum of the N molecular Hamiltonians and the inter-molecular interactions between all molecules

$$\hat{H} = \sum_{p=1}^{N} \hat{H}_p + \sum_{q \neq p} \hat{V}_{pq} \; . \tag{2.14}$$

As before, the interaction potential splits the N individual molecular excited states into N non-degenerate crystal excited states. As $N \to \infty$, a continuous crystalline band of excited states is formed (Figure 2.4). If only nearest neighbour inter-molecular interactions are considered, the crystal excited state wavefunctions can be described by a linear combination of molecular ground and excited state wavefunction products weighted by a Bloch-like phase factor,

$$\psi_k = N^{-1/2} \sum_{p=1}^{N} e^{ikpd} \psi^*_p \prod_{q \neq p}^{N} \psi^0_q \; , \tag{2.15a}$$

where individual crystal excited states within the band are labelled by their wavevector, k, given by

$$k = \frac{2\pi m}{Nd} \quad , \quad m = 0, \pm 1, \pm 2, \pm 3, \ldots, \pm N/2 \; . \tag{2.15b}$$

The corresponding crystal excited state energies form the dispersion relation,

$$\varepsilon_k = \varepsilon^0 + \varepsilon^* + D^* + 2I_{12}\cos(kd) \ , \tag{2.15c}$$

and show how the excited state bandwidth is given by $4I_{12}$.

The inter-molecular interactions serve to delocalise excitations across the whole crystal, imparting them with a momentum equal to $\hbar k$ and allowing them to move very efficiently along the crystal. Such transport is known as coherent or band-like transport, and is in stark contrast to the stochastic hopping transport mechanisms found in disordered molecular solids where excitations are localised. As photons carry no momentum, optical access to the crystal band is obtained via the $k = 0$ state.

2.1.2.3 Electronic Structure of Real Molecular Crystals

The one-dimensional molecular crystal model can in turn be extended in order to describe more realistic crystal structures. Extension to three-dimensions and inequivalent lattice vectors simply introduces three-dimensional wavevectors and dispersion relations. Incorporation of translationally inequivalent molecules is more complex however, and was first performed by Davydov [12] who showed that whilst interactions between translationally equivalent molecules leads to splitting of the discrete molecular states into bands, the interactions between translationally inequivalent molecules leads to splitting of the formed bands into multiple bands (Figure 2.4). Davydov showed that the number of bands formed is equal to the number of translationally inequivalent molecules in the unit cell, σ. In the specific case of $\sigma = 2$, the crystal excited state band is split into two bands described by the wavefunctions, $\psi_{\pm;k}$,

$$\psi_{\pm;k} = 2^{-1/2}\left(\psi_{b;k} \pm \psi_{a;k}\right) \ , \tag{2.16a}$$

where $\psi_{a;k}$, $\psi_{b;k}$ are crystal excited state wavefunctions of the form described by Equation 2.15a summed over the two inequivalent sub-lattices, a and b. The corresponding band dispersion relations, $\varepsilon_{\pm;k}$, are given by

$$\varepsilon_{\pm;k} = \varepsilon^0 + \varepsilon^* + D^* + I_{aa;k} \pm I_{ab;k} \ , \tag{2.16b}$$

with,

$$D^* = \sum_{p=1,q\neq p}^{N} \left(\langle |\psi^*_{qb}|^2 |\hat{V}_{pa;qb}| |\psi^0_{pa}|^2 \rangle - \langle |\psi^0_{qb}|^2 |\hat{V}_{pa;qb}| |\psi^0_{pa}|^2 \rangle \right) \tag{2.16c}$$

$$I_{aa;k} = \sum_{p=1,q\neq p}^{N_a} I_{pa;qa} e^{i\mathbf{k}\cdot(\mathbf{r}_{pa}-\mathbf{r}_{qa})} \tag{2.16d}$$

$$I_{ab;k} = \sum_{p=1,q\neq p}^{N_a} I_{pa;qb} e^{i\mathbf{k}\cdot\left(\mathbf{r}_{pa}-\mathbf{r}_{qb}\right)} \ , \tag{2.16e}$$

where **r** is the lattice vector between molecules and,

$$I_{pa;qa} = \langle \psi^0_{pa} \psi^*_{qa} | \hat{V}_{pa;qa} | \psi^*_{pa} \psi^0_{qa} \rangle \tag{2.16f}$$

$$I_{pa;qb} = \langle \psi^0_{pa} \psi^*_{qb} | \hat{V}_{pa;qb} | \psi^*_{pa} \psi^0_{qb} \rangle \ , \tag{2.16g}$$

describe the interactions between translationally equivalent and inequivalent molecules. The energetic separation between the two $k = 0$ points is known as the Davydov splitting energy, and for nearest neighbour interactions can be shown to be approximately equal to $2I_{ab;0} \approx 8I_{12}$ [19, Ch. 6].

In summary, knowledge of the nature of inter-molecular interactions and the unit cell of a molecular crystal allows the crystalline energy levels to be related to their constituent molecular counterparts. The key effects can be summarised as,

- A shift of the ground and excited state molecular energies by the Coulomb interaction energy. This is mediated by interactions between translationally equivalent molecules.
- Splitting of the individual molecular excited states into a crystalline band due to the resonance interaction energy. This is once again mediated by interactions between translationally equivalent molecules.
- Splitting of the crystal bands into multiple bands by the Davydov splitting energy. This is mediated by interactions between translationally inequivalent molecules.

2.1.3 Singlet Fission & Triplet Fusion

Singlet fission (SF) is a process whereby an excited singlet state shares its energy with neighbouring chromophores to generate two (or more) lower energy triplets. Singlet fission is of great interest for PV applications as it has the potential to enable generation of two carriers from a single photon, thereby increasing the device photocurrent. A basic energetic requirement for the SF process is however that the energy of the singlet state must be at least twice the energy of the triplet state, meaning that any potential gains in photocurrent are therefore instantly negated by a loss in photovoltage. Carrier transport is however a key issue in organic PV, with most devices being severely hindered by slow stochastic hopping transport processes. In this regime, the short lifetime of photogenerated singlet excitons results in their short diffusion lengths, making them difficult to efficiently extract from the device active region. In contrast, the comparatively long-lifetime of triplet excitons makes for more efficient collection, but triplet yields are low due to the preclusion of direct photo-generation. Within this picture, it is clear that efficient singlet to triplet conversion via SF can therefore bring significant performance improvements to PV applications.

As described previously, transitions between singlet and triplet exciton manifolds are spin disallowed, and so take place very slowly via ISC. In contrast, SF can — somewhat counter-intuitively — be considered a spin allowed process and so can occur very quickly. This can be understood by considering the two resultant triplet excitons as a correlated triplet pair, where by correlation it is understood that there is significant interaction between the two triplet states so to as to enable spin-spin interactions. Recalling that triplets have a total spin of one, spin combination of two triplet states yields nine triplet pair sub-states spread over three spin manifolds; the quintet, triplet, and singlet bi-triplet manifolds. Transitions between an excited singlet state and a singlet bi-triplet state, $^1(TT)$, can therefore be seen to be spin allowed as no change of total spin is required. Within this framework, SF can be thought of as a specific case of internal conversion (IC) — i.e. non-radiative relaxation within a spin manifold — with its associated high rates.

In reality, further spin coupling (e.g. spin dipole-dipole coupling, hyperfine coupling, etc.) results in the bi-triplet states having mixed rather than pure spin multiplicity and being described as a coherent superposition of the bi-triplet sub-states* [20]. As a direct result of this, spin coupling mediated ISC can occur between the three manifolds allowing transitions from a bi-triplet state of predominant singlet spin character, $^1(TT)$, to one of predominant triplet spin character, $^3(TT)$. Such conversion is thought to be partly responsible for the subsequent dissociation of the bi-triplet state into two individual triplets. Singlet fission is therefore often treated as a two step process; 1) internal conversion from an excited singlet to an intermediate bi-triplet state with predominant singlet character, 2) decoherence of the intermediate bi-triplet state into two uncorrelated triplets via ISC across the bi-triplet spin manifolds,

$$S_0 + S_1 \xrightleftharpoons{IC} {}^1(TT) \xrightleftharpoons{ISC} T_1 + T_1 \ . \tag{2.17}$$

A further consequence of spin mixing is the possibility of direct SF to bi-triplet states with minor singlet character — i.e. low relative amplitude of the pure $^1(TT)$ total spin operator eigenstate — although this possibility is generally ignored.

The above theoretical framework relies on strong interactions between two triplets located on adjacent molecules and so inherently requires inter-molecular interactions to be present. For this reason, SF is generally assumed to be a significant process in the solid phase where inter-molecular distances are small. Indeed, it can be shown that the direct singlet fission transitions described are mediated by the coulomb integral of initial and final states, and so depend strongly on wavefunction overlap and therefore molecular packing. Molecular crystals are therefore ideal systems in which to study SF due to their regular molecular order.

---

[*] This is directly analogous to the spin mixing of singlet and triplet states by SO coupling which leads to SO-mediated ISC

It should also be noted that above formulation directly implies the possibility of an inverse SF process — viz. the conversion of two triplets into a higher energy excited singlet state and a lower energy ground state singlet. This process is known as triplet-triplet annihilation or triplet fusion (TF) and has been widely observed in many molecular systems. The repopulation of the emissive singlet state from long-lived triplets results in luminescence decays which are slower than those associated with intrinsic fluorescence. This emission is therefore referred to as delayed fluorescence and is a simple indicator of the presence of TF. The energetic requirements for TF are the inverse of those required for SF — viz. the energy of the excited singlet state must be at most twice the energy of the triplet states. As such, SF and TF are generally considered mutually exclusive processes, although it has been proposed that thermal activation of one process may permit concurrence.

2.1.4 Properties of Rubrene

2.1.4.1 Molecular Rubrene

Rubrene (5,6,11,12-tetraphenyltetracene) is a polyacence derivative consisting of a tetracene backbone with four additional phenyl groups. Its conjugation results in an extended delocalised π electron system approximately above and below the backbone plane. Ab initio calculations (density functional theory) have shown that isolated Rubrene molecules posses two possible equilibrium structures characterised by the D_2 and D_{2h} symmetry point groups (Figure 2.5) [21, 22]. It is thought that the more stable of the two is the D_2 conformation with a twisted backbone with twist angle of ∼42° [22] and so it is the D_2 conformation which can be found in solution and amorphous films. Upon crystallisation however, the lattice energy stabilises the D_{2h} form, planarising the tetracene bakbone.

The lowest optically allowed transition of the D_{2h} form of Rubrene is located at 2.32 eV with semi-empircal calculations showing this to be the HOMO-LUMO transition with a transition dipole moment oriented along the short backbone axis (denoted M). Subsequent optically allowed transitions occur at 3.09 eV and 4.48 eV eV and are polarised in the LN molecular plane [23].

2.1.4.2 Crystalline Rubrene

Single crystals of Rubrene can be grown by epitaxial and physical vapour transport (PVT) methods [4, 24, 25], forming an orthorhombic slip-stacked Herringbone lattice of the D_{2h} symmetry molecules which is characterised by the D_{2h18} point group (Figure 2.5). The unit cell contains four Rubrene molecules in two translationally inequivalent orientations. In the $Acam$ crystallographic scheme, the lattice constants are $a = 14.4$, $b = 7.18$ and $c = 26.9$ Å[4, 26]. Rubrene crystals grown by PVT typically have extended ab faces and are micrometrically

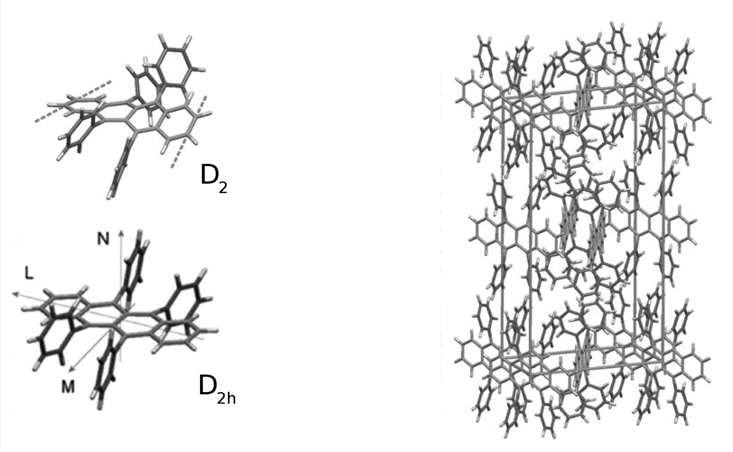

Figure 2.5: *Left panel:* The D_2 (top) and D_{2h} (bottom) equilibrium conformations of the Rubrene molecule. The molecular axis are also shown for the D_{2h} conformation [adapted from 22, 23]. *Right panel:* The Rubrene crystal unit cell [adapted from 22]

thin in the c direction, although more uniformly extensive crystals can also be grown [26]. The calculated HOMO and LUMO wavefunctions are both located predominantly over the molecular backbone, resulting in strong overlap in the b crystal direction. This has been thought to be responsible for the very high, yet anisotropic carrier mobilities [5, 27–29] observed in Rubrene, and possibly also the elongated PL emission profile along this axis [22, 28].

There is still a lack of consensus as to the electronic structure of Rubrene in the crystalline phase with the strength of the intermolecular interactions remaining particularly unclear. Whilst a clear ground state band-structure has recently been experimentally resolved via angle resolved time of flight measurements [30], the presence of such significant structuring of the low-lying excited states remains uncertain. Some authors have interpreted the strong similarity in the absorption spectra of Rubrene solutions and crystals as evidence of negligible excited state band formation and thus have proceeded with a frozen-gas picture [26, 31]. Others predict some degree of inter-molecular coupling in the excited state, leading to delocalisation and narrow band formation [23, 29, 32–34].

Experimentally, it has been shown that Rubrene crystals exhibit highly anisotropic absorption, with the extinction coefficient in the c direction being ~ 4 times higher than in the a and b directions [26]. Vibronic progressions with approximately equal spacings can be seen in all lattice directions, although the first transition is not present in a and b polarised spectra. A similar anisotropy is present in emission, with intense c-polarised emission dominating and an absent ab polarised first vibronic peak (Figure 2.6). Within the context of the frozen-gas picture, this has been explained by vibrational depolarisation of the first M polarised molecular transition [26].

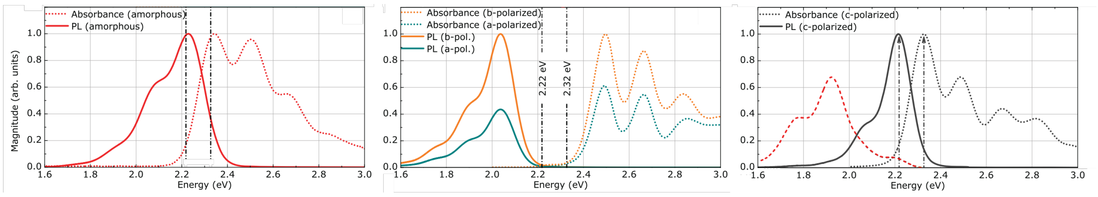

Figure 2.6: Continuous wave absorption (dashed lines) and PL (solid lines) spectra of amorphous Rubrene (left) and along the different axes in Rubrene crystals (middle, right). The spurious low-energy emission sometime observed in crystalline Rubrene is also shown (red dashed line) [adapted from 26]

2.2 Transient Spectroscopic Investigations of Rubrene Single Crystals

In this section, two investigations are presented into some of the less well understood features of Rubrene single crystal photophysics. As described earlier, these are namely the presence of a spurious yet dominant low-energy emission band, and the nature and origin of the long-lived species generated under photo-excitation. All experimental measurements were conducted on high quality monocrystalline samples of Rubrene grown via PVT by the group of Prof. Sassella at Universià degli Studi di Milano-Bicocca [32, 35]. The samples were held under an inert atmosphere before and during measurements to exclude any oxidation-related effects believed to be prevalent in Rubrene [25, 36, 37]. No immediate evidence of significant band-structure in the low-lying optically active excited states was observed, although it is stressed that this was not directly pursued and certainly cannot be excluded. To this extent however, the experimental data obtained were analysed in the context of a simple frozen-gas picture

2.2.1 Low Energy Photoluminescence

The large variation observed in CW PL spectra of Rubrene across different samples is well documented in the literature [26, 38]. Whilst PL peaks at ∼2.21 eV have been previously attributed to emission from the first excited singlet state (S_1) of pristine crystalline rubrene [26, 37, 38], a secondary lower-energy peak at ∼1.92 eV is also frequently observed, and is indeed often the dominant spectral feature (Figure 2.6). The origin of this emission has remained a somewhat enigmatic feature of the photoluminescence of rubrene crystals. Conflicting attributions have been made including an oxidised state of rubrene (possibly rubrene peroxide) [25, 36, 37], a state arising from amorphous inclusions within the rubrene crystal [38], and a self-trapped molecular exciton state [39, 40]. The highly anisotropic optical properties of Rubrene together with significant self-absorption [26] has further hindered measurement and interpretation of this spurious emission.

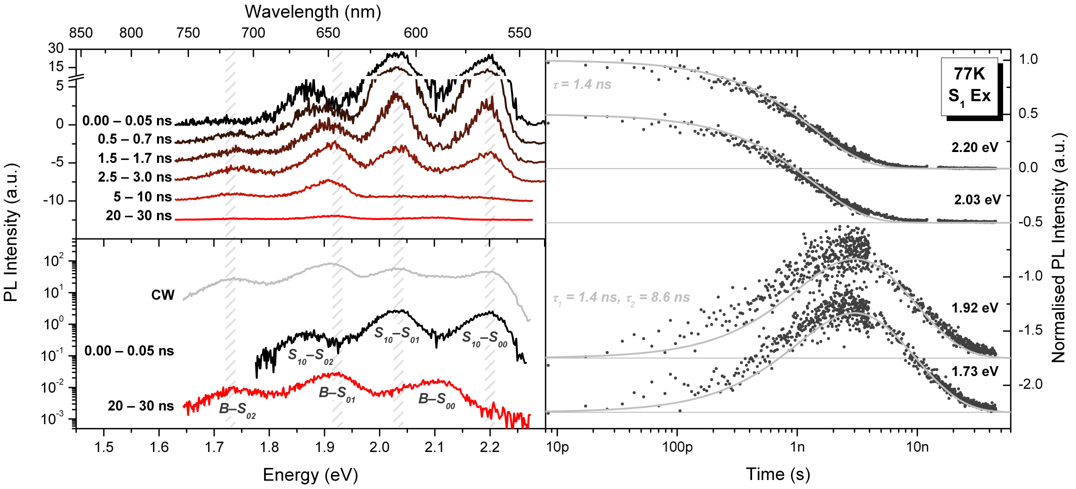

Figure 2.7: *Left panel:* TPL spectra showing the spectral evolution of the PL emission (upper panel) and the deconvolution of the CW spectrum into two distinct vibronic progressions at early and late times (lower panel). *Right panel:* PL dynamics of the principal emission peaks (hatched regions in spectra). Solid lines are scaled mono-exponential (i.e. $e^{-t/\tau}$) and difference-exponential (i.e. $e^{-t/\tau_2} - e^{-t/\tau_1}$) decay guides.

2.2.1.1 Experimental Results

The addition of temporal resolution to PL measurements can often assist the deconvolution of complex spectra. To this extent, the TPL of a Rubrene single crystal was measured in the ns-timescale under resonant excitation of the lowest absorbing excited singlet state, S_1, at 2.30 eV to 2.34 eV. As Rubrene does not exhibit a phase transition at low temperatures [4], the sample was held at 77 K to minimise thermal broadening of emission and further aid interpretation. Great care was taken to maintain the same collection conditions over the course of a measurement so as to avoid complications arising from self-absorption.

The resulting spectra and dynamics are presented in Figure 2.7 and show how temporal resolution clearly separates the high- and low-energy emission components implicitly observed in CW spectra. They can in fact be seen to be two distinct vibronic progressions dominant at early and late times respectively, which are not immediately apparent in room temperature CW spectra due to their strong spectral overlap. Assignment to vibronic progressions is confirmed by the constant energy spacing of the replicas and their identical dynamics.

The immediate mono-exponential decay of the high-energy progression starting at ~2.21 eV shows it to originate from the state initially populated by the excitation pulse. The high-energy progression is therefore assigned to Stokes-shifted emission from the first excited singlet state, S_1, to the ground state, S_0. In contrast, the low-energy progression starting at ~2.10 eV exhibits a well-resolved rise

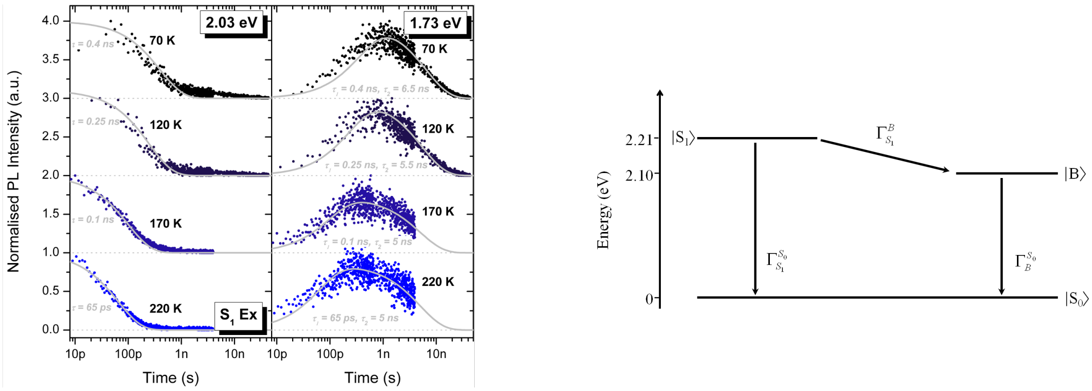

Figure 2.8: *Left panel:* Temperature dependence of Rubrene PL dynamics under excitation of S_1. The dynamics of two spectral bands corresponding to peak emission from the S_1 and B states. Solid lines are scaled mono-exponential (i.e. $e^{-t/\tau}$) and difference-exponential (i.e. $e^{-t/\tau_2} - e^{-t/\tau_1}$) decay guides. *Right panel:* Rubrene three-level model including energetically driven population transfer from S_1 to B

followed by a decay. This rise indicates that the emitting state is not initially populated by the excitation pulse, but rather is populated at later times. For convenience, this low-energy emissive state shall be labelled state B.

The PL dynamics of S_1 and B were both seen to vary with temperature, with increasing temperatures causing a decrease in the rise-time of state B and the decay-time of S_1 (Figure 2.8). This concomitant behaviour suggests B is being populated by the decay of S_1, and indeed the dynamics presented can be adequately modelled by a simple three-level system including energetically driven population transfer from S_1 to B (Figure 2.8).

Whilst emission from B is strong — indicating efficient coupling to S_0 — it is interesting to note that the corresponding absorption transition ($S_0 \rightarrow B$) is very weak. The lowest energy peak typically seen in absorption spectra occurs instead at 2.30 eV to 2.34 eV and is due to the $S_0 \rightarrow S_1$ transition as described above. In order to probe this unexpected asymmetry in optical coupling, excitation dependent TPL measurements were performed by tuning the excitation energy from the first absorption peak to progressively lower photon energies. The resulting PL spectra and dynamics presented in Figure 2.9 show that at excitation energies of ∼2.10 eV the S_1 vibronic progression previously dominant at early times gives way to the vibronic progression associated with state B. This is concurrent with the change in the dynamics of state B from a rise-decay characterised by a difference-exponential, to an instantaneous mono-exponential decay. Taken together, these two observations suggest that state B can be populated directly from S_0 without prior population of S_1. At lower excitation energies, the emission from B was seen to vanish, precluding the possibility of population of B from higher lying states via multi-photon absorption.

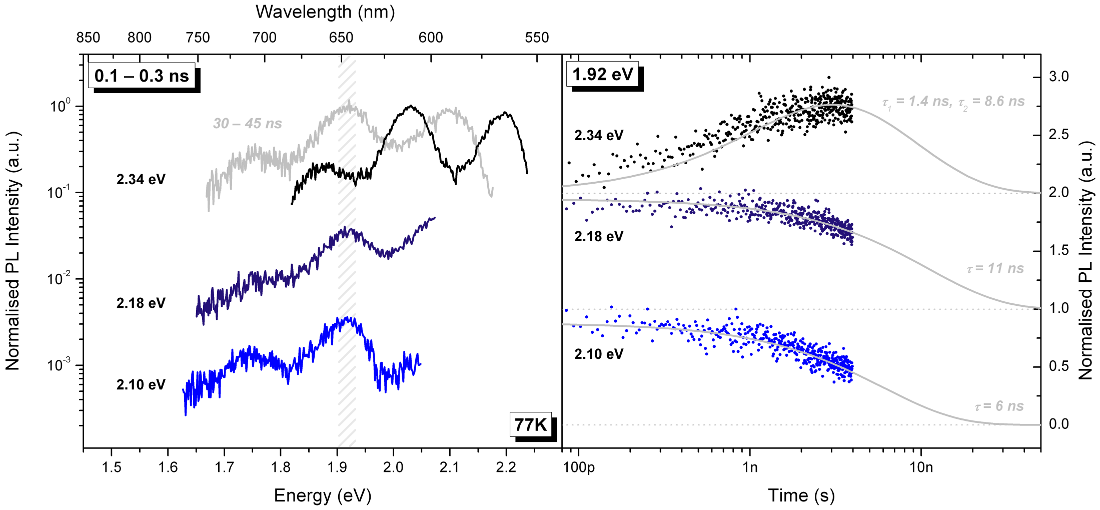

Figure 2.9: *Left panel:* TPL spectra gated at early times under different excitation energies. A spectrum gated at later times under excitation of S_1 is also shown for comparison *Right panel:* Corresponding PL dynamics of the spectral band associated with emission from B (hatched region in spectra). Solid lines are scaled mono-exponential ($e^{-t/\tau}$) and difference-exponential ($e^{-t/\tau_2} - e^{-t/\tau_1}$) decay guides

These results show that despite the absence of a significant absorption peak, direct excitation of B from the ground state is still possible, albeit with a very low efficiency. Further high-sensitivity micro-absorption measurements are planned to probe the strength and energy of this transition more precisely. The population of B without prior population of S_1 indicates that state B cannot be a transient excited state species such as a self-trapped exciton (STE), excimer or exciplex, but is rather a stable state of the ground state molecular configuration.

One possible explanation for the stark transition asymmetry observed could be that the number of B states per unit volume in the crystal is very low, leading to a low amplitude in absorption despite a significant oscillator strength. Upon photoexcitation however, mobile species will tend to funnel toward the lowest energy states before emitting, resulting in strong emission from B. This picture would be consistent with the hypotheses presented in references 38 and 37 which attribute B to a state arising from amorphous inclusions and oxidation induced defects respectively. Whilst the results presented here are not currently sufficient to support or refute these hypotheses, it is noted in passing that the emission from B was seen to be strongly polarised — in agreement with previous reports [26] — making it unlikely to arise from an amorphous phase of rubrene. A crystalline defect region — such as the superficial rubrene peroxide layer reported in [25] — is therefore considered to be the most likely origin of state B. Spatially resolved micro-TPL measurements employing the confocal collection system are planned to investigate the spatial distribution of low-energy emission, which may yield further clues as to the nature of state B.

2.2.1.2 Conclusions

In summary, the origin of the spurious low-energy PL in Rubrene has been shown to arise from a second emissive state, B, which is populated from the higher lying S_1 state. State B has a strong optical coupling to the ground state but exhibits remarkably weak absorption. Nevertheless, B can be populated directly from the ground state, ruling out attribution to a transient excited state species. Whilst not sufficiently proven by our results, we consider it most likely that state B is a defect state originating from a crystalline rubrene peroxide layer. We hypothesise that the observed transition asymmetry is due to a combination of a low defect state number-density and highly mobile photo-generated species.

2.2.2 Long-lived Photo-generated Carrier Dynamics

Carrier transport in monocrystalline Rubrene can be exceptionally efficient as evidenced by the record carrier mobilities achieved in Rubrene field effect transistors (FETs) [5, 27]. Whilst highly technologically relevant, this desirable trait has been limited to architectures where charge injection takes place, such as FETs and light emitting diodes. Recently however, reports have emerged of remarkably long-range diffusion of photo-generated species in Rubrene [6], opening up the possibility for applications in photovoltaics. The long range of these species has been attributed to a long species lifetime, although it should be noted that this is not a necessary requirement. The presence of long-lived species in photoexcited Rubrene single crystals has however been confirmed by a variety of techniques, including CW [6] and transient [41–44] absorption spectroscopies, CW [6] and transient [39, 45] photocurrent spectroscopies, and CW [6, 39, 45] and transient [46] PL spectroscopies. Furthermore, it has been suggested by many that these long-lived species are triplet excitons generated via singlet fission, a process widely believed to be prevalent in both crystalline and amorphous Rubrene [42, 43, 46–48]. Experimental evidence specifically supporting SF in Rubrene also includes device based quantum efficiency measurements [49] and magnetic field dependent PL measurements [49–51]. Despite this wealth of affirmative evidence for SF in monocrystalline Rubrene, unequivocal spectroscopic evidence of SF in the form of direct monitoring of the formed triplet excitons and their subsequent longevity, is notably scant. In particular, as far as the author is aware, only two such independent studies have been published [41, 42], both utilising fs transient absorption techniques. It is interesting to note that of these two studies, only reference 42 detects a significant triplet population attributed to population via SF.

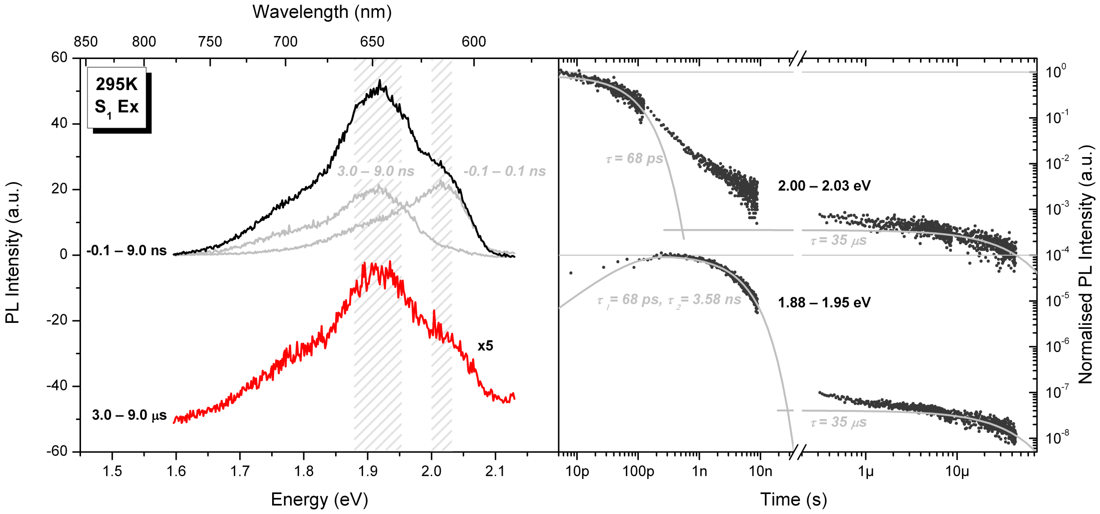

Figure 2.10: *Left panel:* TPL spectra under excitation of S_1 showing the identical nature of the prompt and delayed PL spectra. The contributions from S_1 and B to the prompt PL are shown in grey. *Right panel:* Corresponding PL dynamics of the spectral bands associated with emission from the S_1 and B states (hatched regions in spectra). Solid lines are scaled mono-exponential ($e^{-t/\tau}$) and difference-exponential ($e^{-t/\tau_2} - e^{-t/\tau_1}$) decay guides

2.2.2.1 Experimental Results

Possibly the simplest indirect evidence of the presence of long-lived species is a long-lived component in the sample PL. In Rubrene, a µs-lifetime emission has been observed alongside the typical high-intensity ns-lifetime emission [46]. Seeking to confirm these observations, TPL measurements in the ns- and µs-timescales were performed at room temperature under resonant excitation of S_1. The resulting PL spectra and dynamics are presented in Figure 2.10. Early ns-timescale emission can be seen to occur from state S_1 followed by subsequent population of and emission from state B, consistent with the results of TPL measurements at 77 K. Furthermore, a weak late emission component with a lifetime of the order of µs can be distinguished at later times, in agreement with previous reports in the literature. Tellingly, the late emission exhibits exactly the same spectral shape as the early emission, thereby indicating the same origin — viz. states S_1 and B.

The high intensity and ns-lifetimes of the early emission are however wholly incompatible with subsequent µs-emission as the participating states should be completely depopulated. This phenomenon can be observed in many material systems and is often termed delayed PL so as to differentiate it from the standard prompt PL at early times. The occurrence of delayed PL is often explained by the repopulation of the prompt emissive states via secondary, long-lived — and perhaps non emissive — states (Figure 2.11). In order to be populated, such

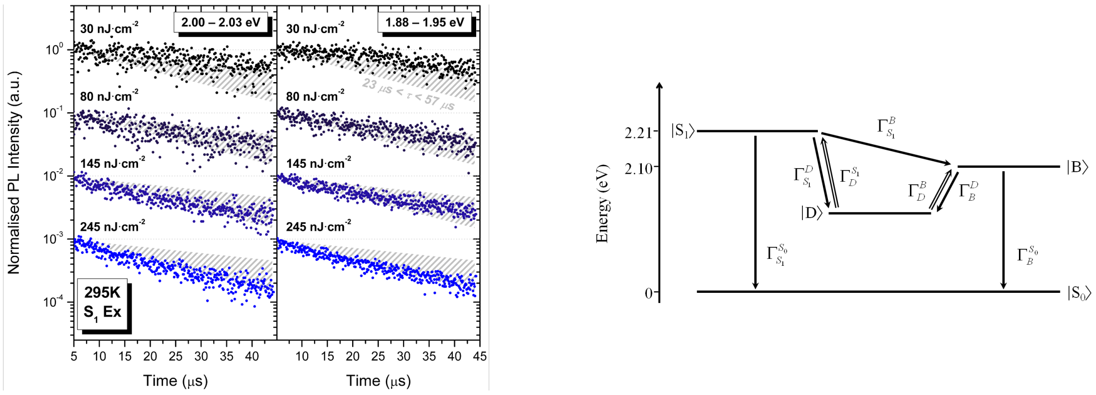

Figure 2.11: *Left panel:* Excitation fluence dependence of the delayed PL dynamics under excitation of S_1. The dynamics of two spectral bands are shown corresponding to peak emission from the S_1 and B states. The hatched regions are mono-exponential ($e^{-t/\tau}$) decay guides for a range of decay times *Right panel:* Rubrene four-level model including repopulation of emissive states from a lower lying long-lived state via multi-particle mechanisms (double arrows)

states generally have an energy below that of the prompt emissive states. As such, energetic requirements require repopulation of the prompt emissive states to take place via a multi-particle recombination mechanism.

To validate this conjecture for the specific case of Rubrene, the fluence dependence of the delayed PL was measured and the resulting dynamics are presented in Figure 2.11. In agreement with previous reports [46, 52], a clear dependence is apparent in the delayed PL from both states S_1 and B, with faster decay dynamics observed at higher fluences as would be expected from multi-particle recombination [46]. This supports the hypothesis that multi-particle repopulation of S_1 and B from a long-lived, low-lying state is responsible for the delayed PL observed in Rubrene. For convenience, we label this state D (Figure 2.11).

State D has typically been assumed to be the lowest triplet state, and the multi-particle recombination mechanism observed has therefore been attributed to triplet fusion [46]. Given the low rate of ISC due to the absence of heavy nuclei in Rubrene, it has been presumed that such a triplet state is populated via SF [42, 43, 46]. Whilst the presence of long-lived states can be inferred indirectly from delayed PL measurements, as mentioned previously direct monitoring of the triplet population is by far preferable as an indicator of SF. To this extent, seeking to investigate the assignment of D to a triplet state optical-probe transient absorption measurements were performed over a wide range of timescales (ps–µs) at room temperature under resonant excitation of S_1. The principal features present in the TA spectra (Figure 2.12) are three photo-induced absorption bands; a weak decaying band at 2.10 eV to 2.18 eV, a sharp growing band peaked at 2.35 eV to 2.45 eV, and a somewhat wider growing band extending from 1.53 eV to 1.80 eV.

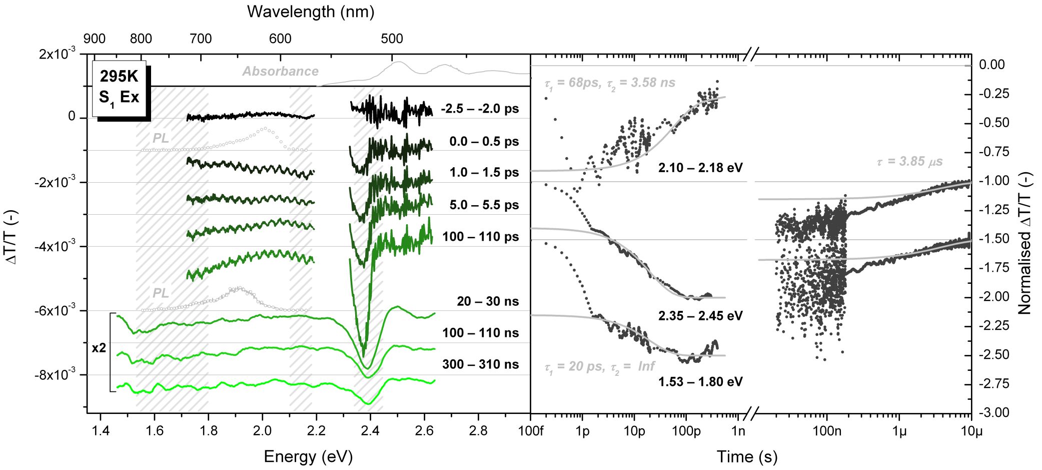

Figure 2.12: *Left panel:* TA differential transmission spectra under excitation of S_1. The corresponding TPL spectra and the CW absorbance spectrum are also shown in grey for reference. *Right panel:* Corresponding TA dynamics of the principal PA bands (hatched regions in spectra). Solid lines are scaled mono-exponential ($e^{-t/\tau}$) and difference-exponential ($e^{-t/\tau_2} - e^{-t/\tau_1}$) decay guides. A bi-exponential ($e^{-t/\tau_2} + e^{-t/\tau_1}$) decay guide is also shown for the 2.10 eV to 2.18 eV band

The growing bands seen at 2.35 eV to 2.45 eV and 2.10 eV to 2.18 eV show identical formation and decay dynamics over multiple time decades (Figure 2.12), strongly implying the same origin. Furthermore, their presence at late times (e.g. 300 ns) ascribes them to a state with a long lifetime. Noting the similar magnitudes of the PA and delayed PL long lifetimes, we assign these bands to PA from the same long-lived state responsible for the delayed PL described above — viz. state D (Figure 2.11). It should be noted that whilst both PA bands have been observed separately before [41, 42, 53], they have not to our knowledge been shown to have the same origin.

The 1.53 eV to 1.80 eV band has been assigned to PA from positive and negative polaron states through comparison with pulsed radiolysis spectra of Rubrene solutions [41, 53]. Further support for this assignment can be found from charge modulation spectroscopy (CMS) performed on Rubrene FETs [54] where a matching, broad PA band peaked at 1.6 eV has been observed (Figure 2.13). Interestingly neither of these supporting datasets shows evidence of the sharp PA band seen at 2.35 eV to 2.45 eV. In the case of the radiolysis measurements, the high optical density of the solutions prevented data being obtained in the 2.07 eV to 2.75 eV range. In the CMS data, no such PA band was observed. This may not be surprising however as CMS is a fundamentally unipolar technique, measuring in this case only induced transitions arising from negative polaron states (n.b. excellent match to Ru^- radiolysis spectrum). In contrast, optical TA measure-

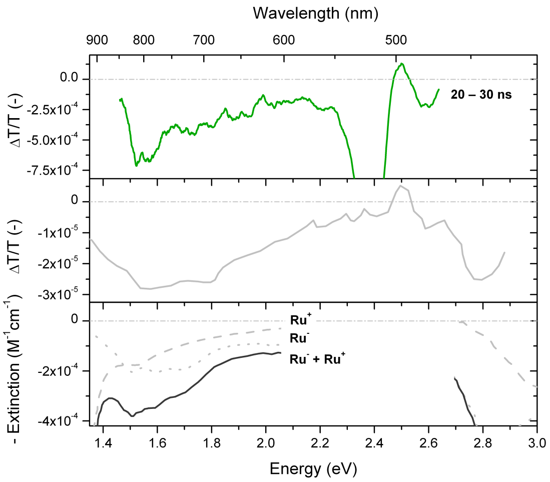

Figure 2.13: Comparison of the measured TA spectrum (upper panel) with CMS (middle panel) [adapted from 54] and pulsed radiolysis spectra (lower panel) [adapted from 53]

ments are intrinsically ambipolar, and as such both positive and negative polaron transitions are probed. Whilst the resulting photo-induced transitions will arise from the two distinct polaron states, their intrinsically linked decay channels mean that they can be expected to exhibit identical dynamics.

Given these good spectral agreements, we attribute state D to the Rubrene crystal polaron states. The associated PA dynamics show that these states are populated in ~100 ps and exhibits a lifetime of several µs. As the S_1 state has been shown to depopulate on a similar timescale ($\tau = 68\,\mathrm{ps}$) to the population of D, we hypothesise that D is populated via exciton dissociation from S_1. Further population may also occur at later times from B, although no evidence for this is presented.

It should be noted that the 2.35 eV to 2.45 eV band has been conflictingly assigned to PA from the lowest Rubrene triplet state T_1 [42–44]. The population time of ~100 ps was considered to be too fast for intersystem crossing in a pure hydrocarbon system such as Rubrene, and as such it was concluded that triplet population was occurring via thermally assisted singlet fission. We comment that 100 ps seems unreasonably slow even for assisted singlet fission, particularly given its reported efficiency of >99 % [43].

Seeking further confirmation for the assignment of state D to a polaronic state, the non-negligible absorption of state B described in § 2.2.1 was exploited to provide an extra energetic degree of freedom. Wide timescale transient absorption measurements were once again performed at room temperature, this time however under direct excitation of state B. The resulting gated spectra and dynamics are presented in Figure 2.14. Interestingly, no significant changes in the spectral features or their dynamics are observed, with both 2.35 eV to 2.45 eV and 1.53 eV

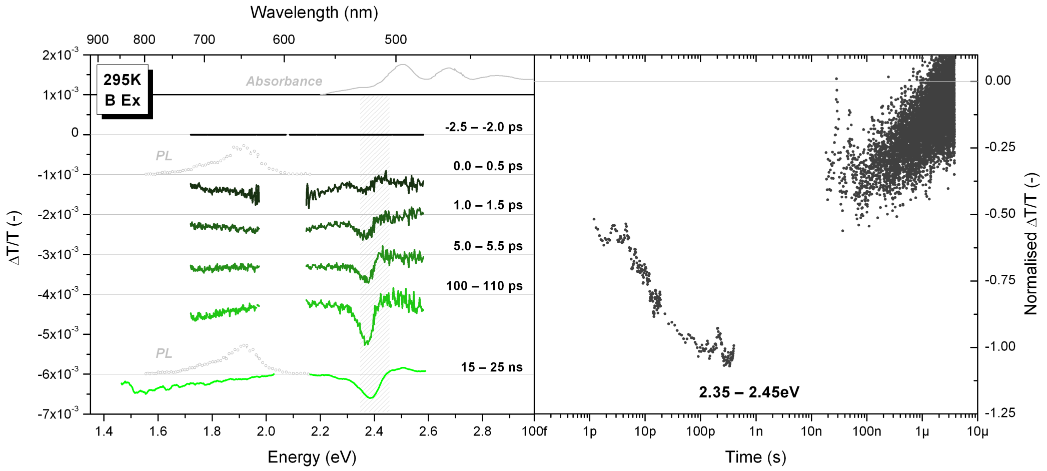

Figure 2.14: *Left panel:* TA differential transmission spectra under excitation of B. The corresponding TPL spectra and the CW absorbance spectrum are also shown in grey for reference. *Right panel:* Corresponding TA dynamics of the principal PA band (hatched region in spectra). N.b. No meaningful data could be extracted for the 1.53 eV to 1.80 eV range due to very low signal to noise levels

to 1.80 eV PA bands still present and lasting for μs. The continued presence of the 2.35 eV to 2.45 eV band indicates that the long-lived state responsible for it can be populated not only from S_1 but also from B. Furthermore, the uncannily similar formation times of the 2.35 eV to 2.45 eV bands under S_1 and B excitation strongly suggest that population of the long-lived state is not occurring via a thermally assisted process. Were this to be the case, the lower energy of B with respect to S_1 would imply a lower proportion of its population distribution would have sufficient energy to undergo thermally assisted SF. As such, a significant decrease in the rate of SF — and thereby triplet formation — would be expected under excitation of state B. The absence of such a dependence in the dynamics of the 2.35 eV to 2.45 eV band suggests an alternative to this triplet-based picture of the long-lived dynamics of Rubrene.

Further opposition for the assignment of D to a triplet state populated by SF can be found in the consideration of the delayed PL described earlier. A key tenet of the singlet fission mechanism is the location of the triplet level below half the energy of the fissile singlet [20]. This is clearly required by energy conservation, although thermal broadening of population distributions and/or excited state band-structuring can potentially allow for moderately higher triplet energies. Interpretation of the results presented in Figure 2.14 with attribution of D to a triplet rather than polaronic state therefore constrains the triplet energy to approximately half the energy of state B (i.e. $2\varepsilon(T) \approx \varepsilon(B)$). In this scenario, the large ~110 meV energy barrier between $2\varepsilon(T)$ and S_1 would render repopulation of S_1 via TF very inefficient if not negligible. As such, it would be expected that the delayed PL spectrum of Rubrene under excitation of state B would not exhibit the high energy component associated with emission from S_1 (c.f. Figure 2.10). Preliminary TPL measurements of this kind — only partially completed due to logistical reasons — have shown that this is not the case, and that the high energy S_1 emission component may still be present in the delayed PL spectrum. Further confirmation of this is however required, including the comparison of the delayed S_1 PL dynamics observed under excitattion of S_1 and B.

2.2.2.2 Conclusions

In summary, the presence of delayed PL in Rubrene crystals due to multi-molecular repopulation of the emissive S_1 and B states via a lower lying, long-lived state D has been confirmed. Two long-lived bands observed in the transient absorption spectra have been assigned to photo-induced absorption from state D. One of these bands shows excellent spectral agreement with polaron photo-induced absorption bands observed in pulsed radiolysis and charge modulation spectroscopy experiments. Both transient absorption bands are still present under excitation of state B, and exhibit the same dynamics. This is inconsistent with the attribution of state D to to a triplet state populated via thermally assisted singlet fission due to the inherent energetic constraints involved. Under all these considerations, the long-lived state D has therefore been attributed to Rubrene polaron states.

References

[1] C. K. Chiang, C. R. Fincher, Y. W. Park, A. J. Heeger, H. Shirakawa, E. J. Louis, S. C. Gau, and A. G. MacDiarmid, Physical Review ... **39**, 1098 (1977), URL http://link.aps.org/doi/10.1103/PhysRevLett.39.1098.

[2] V. V. Walatka, M. M. Labes, and J. H. Perlstein, Physical Review Letters **31**, 1139 (1973), URL http://link.aps.org/doi/10.1103/PhysRevLett.31.1139.

[3] R. Greene, G. Street, and L. Suter, Physical Review Letters **34**, 577 (1975), URL http://prl.aps.org/abstract/PRL/v34/i10/p577_1.

[4] O. D. Jurchescu, A. Meetsma, and T. T. M. Palstra, Acta crystallographica. Section B, Structural science **62**, 330 (2006), ISSN 0108-7681, URL http://www.ncbi.nlm.nih.gov/pubmed/16552167.

[5] V. Podzorov, E. Menard, A. Borissov, V. Kiryukhin, J. a. Rogers, and M. E. Gershenson, Physical Review Letters **93**, 086602 (2004), ISSN 0031-9007, URL http://link.aps.org/doi/10.1103/PhysRevLett.93.086602.

[6] H. Najafov, B. Lee, Q. Zhou, L. C. Feldman, and V. Podzorov, Nature Materials **9**, 938 (2010), ISSN 1476-1122, URL `http://www.nature.com/doifinder/10.1038/nmat2872`.

[7] M. Pope and C. E. Swenberg, *Electronic Processes in Organic Crystals and Polymers* (Oxford University Press, 1999), 2nd ed., ISBN 0195129636.

[8] K. P. C. Vollhardt and N. E. Schore, *Organic Chemistry* (W. H. Freeman, 2010), 6th ed., ISBN 142920494X.

[9] M. Klessinger and J. Michl, *Excited States and Photochemistry of Organic Molecules* (VCH Publishers, 1995), 1st ed., ISBN 1560815884.

[10] P. Atkins and J. De Paula, *Physical Chemistry* (Oxford University Press, Oxford, 2006), 8th ed., ISBN 0198700722.

[11] W. Brütting, ed., *Physics of Organic Semiconductors* (Wiley-VCH, 2005), 1st ed., ISBN 352740550X.

[12] A. S. Davydov, *Theory of Molecular Excitons* (McGraw-Hill, 1962).

[13] Sirjasonr, *Beta Carotene* (2007), URL `http://en.wikipedia.org/wiki/File:Beta-carotene-conjugation.png`.

[14] M. Born and J. R. Oppenheimer, Annalen der Physik **389**, 457 (1927).

[15] P. M. Morse, Physical Review **34**, 57 (1929), URL `http://link.aps.org/doi/10.1103/PhysRev.34.57`.

[16] M. Kasha, Discussions of the Faraday Society **9**, 14 (1950).

[17] D. Beljonne, Z. Shuai, G. Pourtois, and J. L. Bredas, Journal of Physical Chemistry A **105**, 3899 (2001), URL `http://dx.doi.org/10.1021/jp010187w`.

[18] J. Bredas and G. Street, Accounts of Chemical Research **1305**, 309 (1985), URL `http://pubs.acs.org/doi/pdf/10.1021/ar00118a005`.

[19] M. Schwoerer and H. C. Wolf, *Organic Molecular Solids (Physics Textbook)* (Wiley-VCH, 2007), 1st ed., ISBN 3527405402.

[20] M. B. Smith and J. Michl, Chemical reviews **110**, 6891 (2010), ISSN 1520-6890, URL `http://www.ncbi.nlm.nih.gov/pubmed/21053979`.

[21] T. Petrenko, O. Krylova, F. Neese, and M. Sokolowski, New Journal of Physics **11**, 015001 (2009), ISSN 1367-2630, URL `http://stacks.iop.org/1367-2630/11/i=1/a=015001?key=crossref.449efca8b15e254f66872d5d55d6d828`.

[22] D. Käfer and G. Witte, Physical chemistry chemical physics : PCCP **7**, 2850 (2005), ISSN 1463-9076, URL http://www.ncbi.nlm.nih.gov/pubmed/16189602.

[23] S. Tavazzi, A. Borghesi, A. Papagni, P. Spearman, L. Silvestri, A. Yassar, A. Camposeo, M. Polo, and D. Pisignano, Physical Review B **75** (2007), ISSN 1098-0121, URL http://prb.aps.org/abstract/PRB/v75/i24/e245416.

[24] R. A. Laudise, C. Kloc, P. G. Simpkins, and T. Siegrist, Journal of Crystal Growth **187**, 449 (1998), ISSN 0022-0248, URL http://www.sciencedirect.com/science/article/pii/S0022024898000347.

[25] E. Fumagalli, L. Raimondo, L. Silvestri, M. Moret, A. Sassella, and M. Campione, Chemistry of Materials **23**, 3246 (2011), ISSN 0897-4756, URL http://pubs.acs.org/doi/abs/10.1021/cm201230j.

[26] P. Irkhin, A. Ryasnyanskiy, M. Koehler, and I. Biaggio, Physical Review B **86**, 1 (2012), ISSN 1098-0121, URL http://link.aps.org/doi/10.1103/PhysRevB.86.085143.

[27] V. C. Sundar, J. Zaumseil, V. Podzorov, E. Menard, R. L. Willett, T. Someya, M. E. Gershenson, and J. a. Rogers, Science **303**, 1644 (2004), ISSN 1095-9203, URL http://www.ncbi.nlm.nih.gov/pubmed/15016993.

[28] P. Irkhin and I. Biaggio, Physical Review Letters **107**, 017402 (2011), ISSN 0031-9007, URL http://link.aps.org/doi/10.1103/PhysRevLett.107.017402.

[29] D. a. da Silva Filho, E.-G. Kim, and J.-L. Brédas, Advanced Materials **17**, 1072 (2005), ISSN 0935-9648, URL http://doi.wiley.com/10.1002/adma.200401866.

[30] a. Vollmer, R. Ovsyannikov, M. Gorgoi, S. Krause, M. Oehzelt, A. Lindblad, N. Må rtensson, S. Svensson, P. Karlsson, M. Lundvuist, et al., Journal of Electron Spectroscopy and Related Phenomena **185**, 55 (2012), ISSN 03682048, URL http://linkinghub.elsevier.com/retrieve/pii/S0368204812000072.

[31] N. Sai, M. Tiago, J. Chelikowsky, and F. Reboredo, Physical Review B **77** (2008), ISSN 1098-0121, URL http://prb.aps.org/abstract/PRB/v77/i16/e161306.

[32] S. Tavazzi, L. Silvestri, M. Campione, A. Borghesi, A. Papagni, P. Spearman, A. Yassar, A. Camposeo, and D. Pisignano, Journal of Applied Physics **102**, 023107 (2007), ISSN 00218979, URL http://link.aip.org/link/doi/10.1063/1.2759188/html.

[33] B. West, J. Womick, and L. McNeil, The Journal of Physical Chemistry C **114**, 10580 (2010), ISSN 1932-7447, URL http://pubs.acs.org/doi/abs/10.1021/jp101621v.

[34] S. Yanagisawa, Y. Morikawa, and A. Schindlmayr, Physical Review B **88**, 115438 (2013), ISSN 1098-0121, URL http://link.aps.org/doi/10.1103/PhysRevB.88.115438.

[35] D. Braga, N. Battaglini, A. Yassar, G. Horowitz, M. Campione, A. Sassella, and A. Borghesi, Physical Review B **77**, 115205 (2008), ISSN 1098-0121, URL http://link.aps.org/doi/10.1103/PhysRevB.77.115205.

[36] O. Mitrofanov, C. Kloc, T. Siegrist, D. V. Lang, W.-Y. So, and A. P. Ramirez, Applied Physics Letters **91**, 212106 (2007), ISSN 00036951, URL http://link.aip.org/link/APPLAB/v91/i21/p212106/s1&Agg=doi.

[37] O. Mitrofanov, D. V. Lang, C. Kloc, J. M. Wikberg, T. Siegrist, W.-Y. So, M. A. Sergent, and A. P. Ramirez, Physical Review Letters **97**, 166601 (2006), ISSN 0031-9007, URL http://prl.aps.org/abstract/PRL/v97/i16/e166601.

[38] Y. Chen, B. Lee, D. Fu, and V. Podzorov, Advanced Materials **23**, 5370 (2011), ISSN 09359648, URL http://doi.wiley.com/10.1002/adma.201102294.

[39] H. Najafov, I. Biaggio, V. Podzorov, M. Calhoun, and M. Gershenson, Physical Review Letters **96** (2006), ISSN 0031-9007, URL http://prl.aps.org/abstract/PRL/v96/i5/e056604.

[40] R. J. Stohr, G. J. Beirne, P. Michler, R. Scholz, J. Wrachtrup, and J. Pflaum, Applied Physics Letters **96**, 231902 (2010), ISSN 00036951, 0810.1683, URL http://link.aip.org/link/?APPLAB/96/231902/1http://arxiv.org/abs/0810.1683http://link.aip.org/link/APPLAB/v96/i23/p231902/s1&Agg=doi.

[41] S. Tao, H. Matsuzaki, H. Uemura, H. Yada, T. Uemura, J. Takeya, T. Hasegawa, and H. Okamoto, Physical Review B **83**, 1 (2011), ISSN 1098-0121, URL http://link.aps.org/doi/10.1103/PhysRevB.83.075204.

[42] L. Ma, K. Zhang, C. Kloc, H. Sun, M. E. Michel-Beyerle, and G. G. Gurzadyan, Physical Chemistry Chemical Physics **14**, 8307 (2012), ISSN 1463-9076, URL http://xlink.rsc.org/?DOI=c2cp40449d.

[43] L. Ma, K. Zhang, C. Kloc, H. Sun, C. Soci, M. E. Michel-Beyerle, and G. G. Gurzadyan, Physical Review B **87**, 201203 (2013), ISSN 1098-0121, URL http://link.aps.org/doi/10.1103/PhysRevB.87.201203.

[44] L. Ma, G. Galstyan, K. Zhang, C. Kloc, H. Sun, C. Soci, M. E. Michel-Beyerle, and G. G. Gurzadyan, The Journal of chemical physics **138**, 184508 (2013), ISSN 1089-7690, URL `http://www.ncbi.nlm.nih.gov/pubmed/23676057`.

[45] H. Najafov, B. Lyu, I. Biaggio, and V. Podzorov, Applied Physics Letters **96**, 183302 (2010), ISSN 00036951, URL `http://link.aip.org/link/APPLAB/v96/i18/p183302/s1&Agg=doi`.

[46] A. Ryasnyanskiy and I. Biaggio, Physical Review B **84**, 2 (2011), ISSN 1098-0121, URL `http://link.aps.org/doi/10.1103/PhysRevB.84.193203`.

[47] V. Jankus, E. W. Snedden, D. W. Bright, E. Arac, D. Dai, and A. P. Monkman, Physical Review B **87**, 224202 (2013), ISSN 1098-0121, URL `http://link.aps.org/doi/10.1103/PhysRevB.87.224202`.

[48] D. Casanova, Journal of Chemical Theory and Computation **10**, 324 (2013), ISSN 1549-9618, URL `http://dx.doi.org/10.1021/ct4007635`.

[49] P. D. Reusswig, D. N. Congreve, N. J. Thompson, and M. a. Baldo, Applied Physics Letters **101**, 113304 (2012), ISSN 00036951, URL `http://link.aip.org/link/APPLAB/v101/i11/p113304/s1&Agg=doi`.

[50] G. B. Piland, J. J. Burdett, D. Kurunthu, and C. J. Bardeen, The Journal of Physical Chemistry C **117**, 1224 (2013), ISSN 1932-7447, URL `http://pubs.acs.org/doi/abs/10.1021/jp309286v`.

[51] Y. Zhang, Y. Lei, Q. Zhang, and Z. Xiong, Organic Electronics **15**, 577 (2014), ISSN 15661199, URL `http://linkinghub.elsevier.com/retrieve/pii/S1566119913005417`.

[52] X. Wen, P. Yu, C.-T. Yuan, X. Ma, and J. Tang, The Journal of Physical Chemistry C **117**, 17741 (2013), ISSN 1932-7447, URL `http://pubs.acs.org/doi/abs/10.1021/jp404666w`.

[53] a. Saeki, S. Seki, T. Takenobu, Y. Iwasa, and S. Tagawa, Advanced Materials **20**, 920 (2008), ISSN 09359648, URL `http://doi.wiley.com/10.1002/adma.200702463`.

[54] J.-F. Chang, T. Sakanoue, Y. Olivier, T. Uemura, M.-B. Dufourg-Madec, S. G. Yeates, J. Cornil, J. Takeya, A. Troisi, and H. Sirringhaus, Physical Review Letters **107**, 066601 (2011), ISSN 0031-9007, URL `http://link.aps.org/doi/10.1103/PhysRevLett.107.066601`.

Chapter 3

Broadband Transient Photoluminescence Case Studies

In this chapter, a variety of published or submitted investigations performed using the TPL system described in Chapter 1 are presented. In each case, focus is given to the role of TPL measurements within the investigation and the particular TPL system specifications enabling them to be undertaken. The work described contains contributions from multiple authors and so readers are referred to the full publications [1–4] for further details and full acknowledgements.

3.1 Panchromatic Dye-Doped Polymer Solar Cells [1]

3.1.1 Background

Photovoltaic (PV) devices rely on the separate extraction of electrons and holes from the active material in order to generate a photocurrent. This can pose a challenge for organic PV materials which — as described in § 2.1.1.4 — have neutral molecular Frenkel excitons as the dominant photoexcitation due to their low dielectric constants. Organic PV devices must therefore exhibit efficient exciton dissociation to overcome the exciton binding energy and result in an electron-hole pair. This is typically achieved by combining two photo-active organic materials with differing energetic levels so as to create a type II electron donor-acceptor interface. The energetic gradient across the interface is used for dissociation of excitons located on either side of it.

Of all the possible configurations, the archetypal donor-acceptor architecture is perhaps the bulk heterojunction (BHJ) — a bulk mixture of two immiscible absorbing organic materials (e.g. polymer donor, fullerene acceptor) which self-assemble into donor and acceptor domains [5]. Whilst this typically results in a highly absorbing device, carrier transport and collection is usually very poor due to the disconnected donor and acceptor domains and poor transport properties of most organic materials [6, 7]. In aiming to address this shortcoming, alternative hybrid architectures can be used where the organic acceptor of the BHJ is replaced by an inorganic acceptor, such as a mesoporous metal oxide. Whilst transport is typically improved due to the significantly greater order and transport properties of most inorganic materials, the absorption spectrum of such devices is generally very narrow owing to the semi-transparent nature of most suitable inorganic acceptors. This results in a significant fraction of solar radiation incident on the cell being lost and consequentially, lower device efficiencies. Careful choice of donor and acceptor material absorption bands can of course come some way to resolving this issue, although energetic alignment must always be carefully considered to maintain a dissociating interface. A recently proposed alternative approach for spectral broadening of such devices is the additions of further absorbing elements to the donor-acceptor architecture. Whilst providing absorption, these need not necessarily yield further interfaces for exciton dissociation but rather act only as light harvesting antennae, transferring generated excitons to the donor or acceptor materials for subsequent dissociation. Such decoupling relaxes the energetic alignment constraints imposed by the need for an interface and allows wider device absorption bands to be achieved.

Exciton transfer can occur via fast non-radiative processes such as Förster resonant energy transfer (FRET) — a mechanism by which an excited chromophore transfers its energy to a neighbouring unexcited chromophore via dipole-dipole coupling [8]. Förster resonant energy transfer is highly sensitive to both the chromophore separation and emission/absorption spectra overlap, with the characteristic Förster radius, R_0, being given by

$$R_0 = \frac{9 Q_{D0} \ln(10) \kappa^2 J}{128 \pi^5 n^4 N_A} \, , \tag{3.1}$$

where Q_{D0} is the PL quantum yield of the isolated energy donor chromophore, κ is a factor describing the dipole orientation, N_A is Avogadro's number and J is the normalised emission, f_D, and extinction, ϵ_A spectral overlap integral, $J = \int f_D \epsilon_A \lambda^4 d\lambda$.

The work presented below demonstrates the operation of such a light harvesting organic PV device (Figure 3.1) consisting of the low bandgap copolymer donor poly[2,6-(4,4-bis-(2-ethylhexyl)-4H-cyclopenta[2,1-b;3,4-b0]dithiophene)-alt-4,7-(2,1,3-benzothiadia-zole)] (PCPDTBT), the transparent inorganic metal oxide acceptor ZnO, and the high bandgap small molecule antenna 2,2,7,7-tetrakis(3-hexyl-5-(7-(4-hexylthiophen-2-yl)benzo[c][1,2,5]thiadiazol-4-yl)thiophen-2-yl)-9,9-spirobifluorene (Spiro-TBT). Focus is given on the demonstration of exciton transfer from the antennae to the donor via FRET and its beneficial effects on PV device performance via transient spectroscopic techniques.

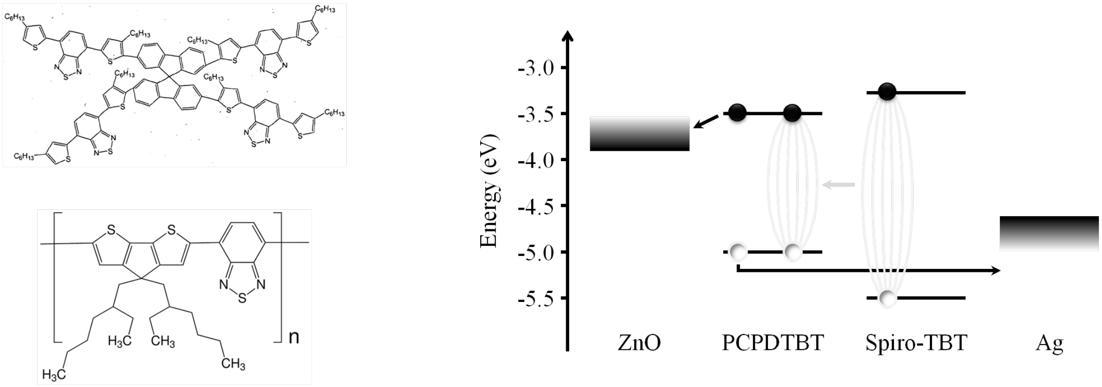

Figure 3.1: *Left panel:* Chemical structure of Spiro-TBT (top) and PCPDTBT (bottom). *Right panel:* Energetic model of the dye-doped polymer cell showing the distinct energy (grey) and charge (black) transfer steps [adapted from 1 courtesy of Dr. G. Grancini]

3.1.2 Experimental Results

The CW absorption spectra of Spiro-TBT and PCPDTBT were measured and shown to be complimentary, with Spiro-TBT exhibiting an absorption peak around the 500 nm region where PCPDTBT absorption is weak (Figure 3.2). The CW PL spectrum of Spiro-TBT was also measured and shown to have significant overlap with the PCPDTBT absorption spectrum, suggesting the possibility of FRET from the Spiro-TBT to the PCPDTBT donor. This was supported by calculation of the Förster radius (using Equation 3.1 with representative material parameters) which yielded a radius of a similar order of magnitude to the expected donor/antenna separation (∼4 nm).

Experimental confirmation of FRET was sought through measurement of the CW PL spectra of neat Spiro-TBT, neat PCPDTBT and blended Spiro-TBT:PCPDTBT samples (Figure 3.2). These showed that the strong Spiro-TBT PL was heavily quenched in the blended sample, suggesting the presence of energy transfer from the Spiro-TBT to the PCPDTBT.

Seeking more unequivocal confirmation, high temporal resolution TPL measurements were performed with an aim to explicitly resolve the energetic migration from antennae to donor (Figure 3.3). Sample excitation was chosen to be at 2.3 eV so as to preferentially excite the Spiro-TBT antennae. Comparison of the PL dynamics of the neat Spiro-TBT and blended samples integrated over the peak Spiro-TBT emission (∼1.94 eV) confirm a marked quenching of the Spiro-TBT PL when blended with PCPDTBT, as evidenced by a faster PL decay. Correspondingly, the PL dynamics integrated over the peak PCPDTBT emission (∼1.44 eV) show the instantaneous decay dynamics present in the neat sample giving way to a rise-decay form in the blended sample. Taken together, these two characteristics are compelling evidence for the presence of an energy transfer process from Spiro-TBT to PCPDTBT which completes within ∼20 ps.

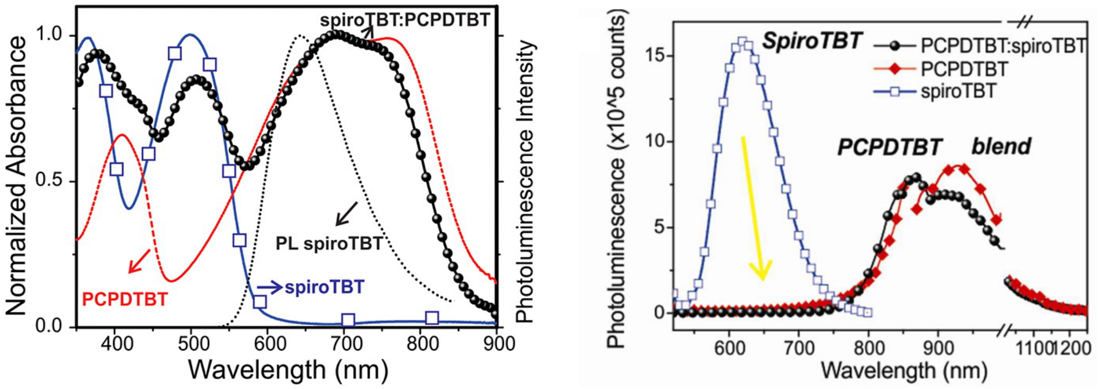

Figure 3.2: *Left panel:* Continuous wave absorption spectra of the neat Spiro-TBT, neat PCPDTBT and blended Spiro-TBT:PCPDTBT samples. The CW PL spectrum of neat Spiro-TBT is also depicted (dashed black line) showing the significant spectral overlap with PCPDTBT absorption. *Right panel:* Continuous wave PL spectra of the same three samples showing the heavy quenching of Spiro-TBT PL in the blended sample [adapted from 1 courtesy of Dr. G. Grancini]

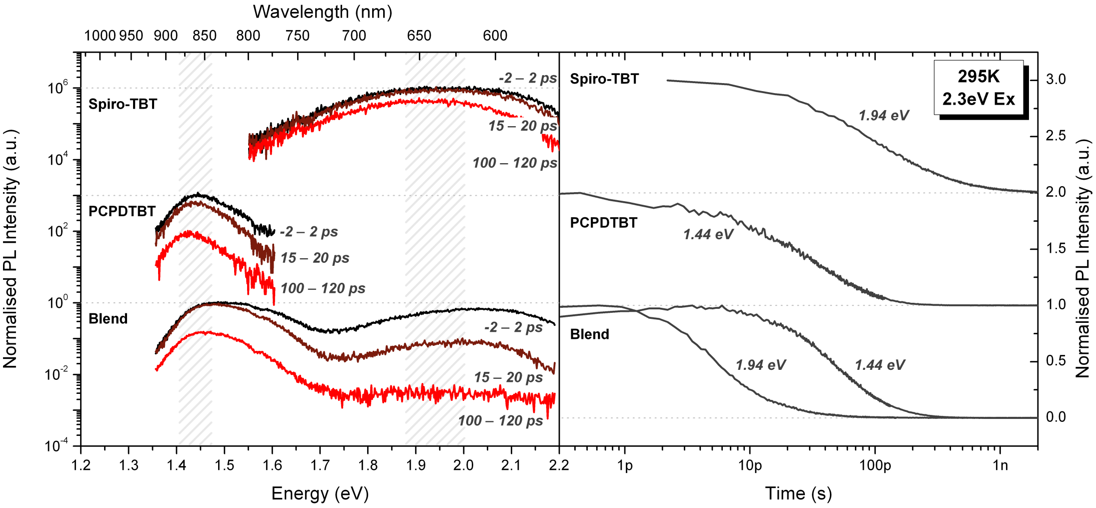

Figure 3.3: *Left panel:* TPL spectra of the neat Spiro-TBT, neat PCPDTBT and blended Spiro-TBT:PCPDTBT samples under 2.3 eV excitation showing the spectral evolution of their PL emission. *Right panel:* Corresponding PL dynamics of the spectral bands associated with Spiro-TBT and PCPDTBT emission (hatched regions in spectra). The significantly shortened PL lifetime of Spiro-TBT and the ∼4 ps rise-time of PCPDTBT emission in the blended sample can be clearly seen

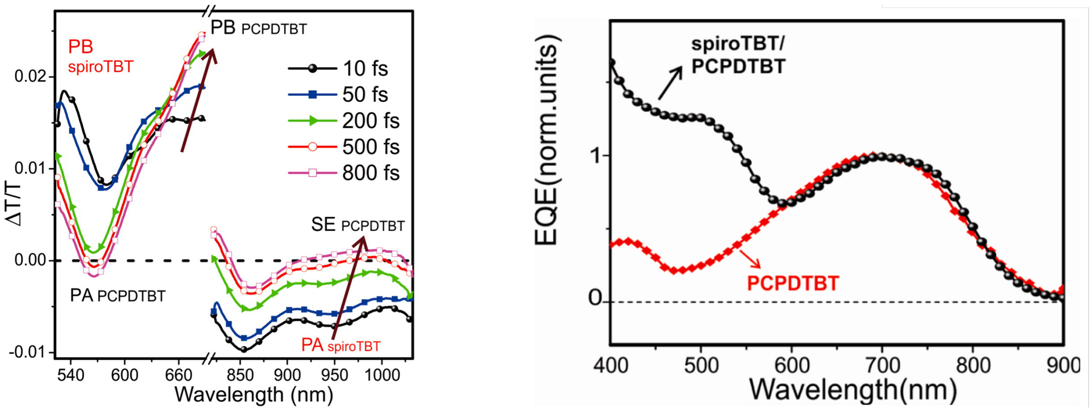

Figure 3.4: *Left panel:* Transient absorption spectra of the Spiro-TBT:PCPDTBT blend sample showing the evolution from dominant Spiro-TBT features to dominant PCPDTBT features [adapted from 1 courtesy of Dr. G. Grancini, Dr. S.S.K. Raavi & Dr. M. Maiuri] *Right panel:* External quantum efficiency spectrum of the full blend device (ZnO:PCPDTBT:Spiro-TBT) showing increased efficiency due to Spiro-TBT absorption and energy transfer [adapted from 1 courtesy of Dr. G. Grancini]

Seeking to observe the onset of this process, sub-10 fs resolution [9] TA measurements of the neat and blended films were performed with the excitation wavelength once again selected so as to preferentially excite the Spiro-TBT antennae. The presence of two different materials each potentially exhibiting multiple PA, PB and SE bands resulted in significantly congested spectra with multiple differential band overlap (Figure 3.4). As such, further spectral and temporal information on the system population dynamics from TPL was necessary in order to deconvolve the complex TA maps.

At early times (∼10 fs), the blended TA spectra are seen to closely resemble the pure Spiro-TBT TA spectra. Spiro PB and SE bands can be identified at wavelengths below 700 nm, in good agreement with the previously measured absorption and TPL spectra respectively, and confirming the preferential excitation of the Spiro-TBT antennae. Within 100 fs however, the spectra can be seen to change rapidly, assuming a form more closely related to the pure PCPDTBT spectra. In particular, a growing positive band located at ∼680 nm can be identified as the polymer PB band due to its proximity to the polymer CW absorption peak and location in a spectral region with little Spiro-TBT TA signal. Comparison of this band with the polymer TPL dynamics identified in the blended film (Figure 3.3) shows good agreement, confirming the attribution of this TA feature to PB of the polymer. As in the TPL measurements, the presence of a rapidly decaying initial Spiro-TBT signal in conjunction with an initially absent but rapidly growing PCPDTBT signal is a compelling indicator of the presence of rapid energy transfer from the Spiro-TBT to the PCPDTBT.

Further TA measurements on a full device structure incorporating the metal-oxide acceptor were also conducted and showed similar evidence of energy transfer. Tellingly, PA bands associated to the presence of holes in the PCPDTBT could be seen in this sample — a feature notably absent in the samples without the metal-oxide acceptor. This demonstrates that exciton dissociation is indeed only occurring at the donor-acceptor interface, whilst pure energy and not charge transfer is taking place across the donor-antennae interface.

A marked improvement in photovoltaic performance was also observed in the full device, with measurement of the external quantum efficiency spectrum showing this to be due to an additional contribution to the device efficiency from Spiro-TBT absorption (Figure 3.4).

3.1.3 Conclusions

The experimental work described in this publication shows a novel approach for extending the useful spectral range of PV devices without requiring careful consideration of typical energetic constraints. The demonstrated separation of light-harvesting and charge generation functions of PV devices has the potential to open up new device architecture possibilities.

The work also highlights the utility of ps-resolution TPL in the identification and investigation of fast processes such as FRET. It should be noted that such processes need not necessarily be radiative in themselves in order to be detected via TPL as their comparative effect on the radiative transitions of the system are frequently enough to allow useful insights to be gained.

The importance of broadband tunability of the PL excitation source was also demonstrated, enabling selective subs-system excitation and thereby control of initial system conditions.

Finally, the utility of ps-resolution TPL measurements as an additional information source to aid deconvolution of complex overlapping fs-TA spectra was shown. This allows the full power of TA measurements to be leveraged through more precise band assignment through spectral and temporal comparison. This can only be achieved when there is both significant spectral and temporal overlap of TA and TPL systems.

3.2 Regulation of Photosystem I Light Harvesting by Zeaxanthin [2]

3.2.1 Background

The most abundant, and arguably most important light harvesting process on this planet is photosynthesis — the process by which certain organisms convert incident light into chemical energy. In higher plants, photosynthesis is a two part process consisting of light-dependent and light-independent reactions. The light-dependent reactions are the first stage of photosynthesis, where light and water inputs are converted into the energy carrying molecules adenosine triphosphate (ATP) and nicotinamide adenine dinucleotide phosphate (NADPH). These are subsequently used as in the light-independent reactions alongside CO_2 to produce glucose. The overall scheme for these two reactions in oxygenic photosynthesis can be written as [10],

$$\begin{aligned} 6\,\mathrm{H_2O} + 3\,(2\,\mathrm{NADP^+} + 3\,\mathrm{ADP} + 3\,\mathrm{P_i}) \xrightarrow{\gamma} 3\,\mathrm{O_2} + 3\,(2\,\mathrm{NADPH} \\ + 3\,\mathrm{ATP} + 2\,\mathrm{H^+}) \end{aligned} \tag{3.2a}$$

$$\begin{aligned} 3\,\mathrm{CO_2} + 3\,(2\,\mathrm{NADPH} + 3\,\mathrm{ATP} + 2\,\mathrm{H^+}) \longrightarrow 3\,\mathrm{H_2O} + (\mathrm{G3P} + 8\,\mathrm{P_i}) \\ + 3\,(2\,\mathrm{NADP^+} + 3\,\mathrm{ADP})\,, \end{aligned} \tag{3.2b}$$

where $3P_i$ is inorganic phosphate and G3P is glyceraldehyde-3-phosphate.

3.2.1.1 Light Dependent Reactions of Photosynthesis

In higher plants, the light-dependent reactions of photosynthesis take place at thylakoids — membrane-bound compartments within the chloroplast organelles found in leaf cells (Figure 3.5). The thylakoid membrane separates the thylakoid interior — denoted the lumen — from the exterior chloroplast space — denoted the stroma. Multiple protein structures are embedded within the thylakoid membrane (Figure 3.5), and it is within these structures that the light-dependent reactions take place. Briefly;

- A photon is absorbed by photosystem II (PSII)
- The excited electron is transferred to the plastoquinone structure, thereby oxidising PSII
- PSII is subsequently reduced by the hydrolysis of water present in the lumen, liberating molecular oxygen to the environment and protons to the lumen
- The electron is passed along a transfer chain consisting of plastoquinone, cytochrome and plastocyanin structures, before arriving at photosystem I (PSI)
- During transfer from plastoquinone to cytochrome, the energy carried by the electron is used to pump protons from the stroma to the lumen via a further trans-membrane reduction-oxidation (REDOX) reaction
- A photon is absorbed by PSI
- The excited electron is transferred to ferredoxin — thereby oxidising PSI — where it is used to reduce $NADP^+$ to NADPH

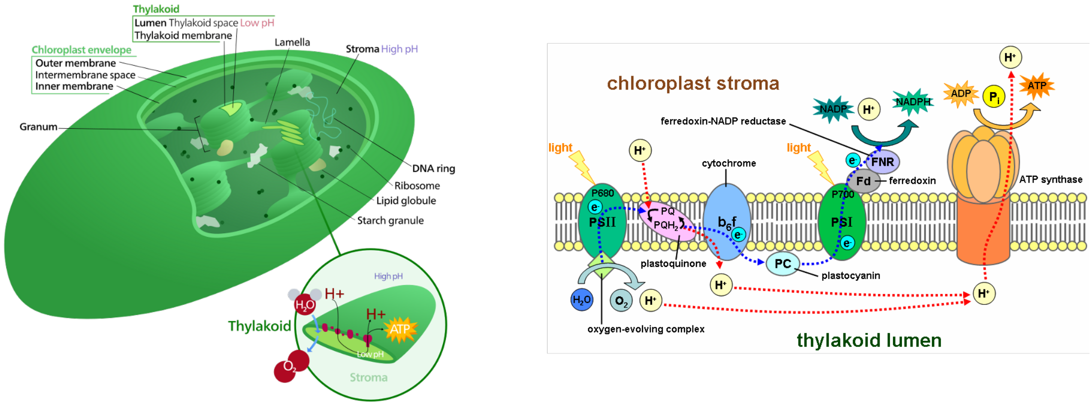
Thylakoid
Lumen Thylakoid space Low pH
Thylakoid membrane
Lamella
Stroma High pH
Chloroplast envelope
Outer membrane
Intermembrane space
Inner membrane
Granum
DNA ring
Ribosome
Lipid globule
Starch granule
High pH
H+
H_2O
H+
ATP
Thylakoid
Low pH
O_2
Stroma
chloroplast stroma
H+
NADP
H+
NADPH
ADP
P_i
ATP
ferredoxin-NADP reductase
light
H+
light
cytochrome
e-
FNR
Fd
ferredoxin
ATP synthase
P680
e-
PSII
PQ
PQH_2
b_6f
e-
P700
PSI
e-
plastoquinone
PC
plastocyanin
H+
H+
H_2O
O_2
H+
oxygen-evolving complex
thylakoid lumen

Figure 3.5: *Left panel:* Location of thylakoid compartments within the chloroplast organelles [adapted from 11, public domain *Right panel:* Thylakoid membrane protein structures involved in the light dependent reactions of photosynthesis. Electron transfer (blue arrows) and proton pumping processes (red arrows) are also depicted [adapted from 12, public domain]

- PSI is subsequently reduced by the electron originating from PSII
- The proton gradient developed across the thylakoid membrane during the entire reaction is used by the ATP synthase structure to convert ADP in the stroma to ATP

It can be seen that the light-dependent reactions are reliant on the sequential absorption of two photons. This is required for the fast reduction of PSI so as to render the reduction of $NADP^+$ competitive with recombination.

3.2.1.2 Higher Plant Photosystems

Light absorption in higher plants occurs in the pigment containing protein structures PSI and PSII. A key feature common to both photosystems is a reaction centre containing a chlorophyll (Chl) dimer which performs electron transfer to adjacently located structures (plastoquinone in the case of PSII, ferredoxin in the case of PSI). Owing to its small cross-section however, the probability of photon absorption by the Chl dimer is very low. The reaction centre is therefore bound to pigment containing cofactors to increase absorption, with the absorbed energy being transferred to the reaction centre via non-radiative processes (viz. FRET). These additional antenna cofactors are denoted inner light harvesting complexes (LHCs) and contain beta-carotene and Chl A pigments. The ensemble of reaction centre and inner LHCs are known as the photosystem-core (PS-core) and are depicted in Figure 3.6.

Photosystem-core absorbance is further increased by association to surrounding outer LHCs, which once again harvest light and transfer energy non-radiatvely to the PS-core. The outer LHCs predominantly associated to PSI are denoted

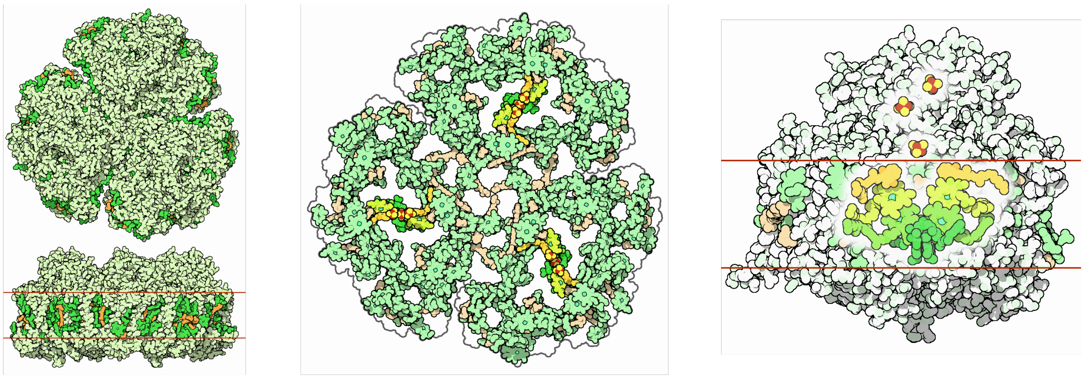

Figure 3.6: *Left panel:* Photosystem I structure showing the protein scaffold (light green) and pigments (dark green, orange). *Middle panel:* Photosystem I structure with the protein scaffold hidden. Three PSI-cores can be seen each comprised of a Chl dimer (dark green), inner LHC Chls (yellow-green), inner LHC xanthophylls (dark orange) and ferredoxin molecules (red-yellow). The corresponding three outer LHCs can also be made out with their abundant Chl (light green) and xanthophyll (light orange) content. *Right panel:* Close-up of the PSI-core. The position of thylakoid membrane is depicted by the red solid lines [courtesy of 13]

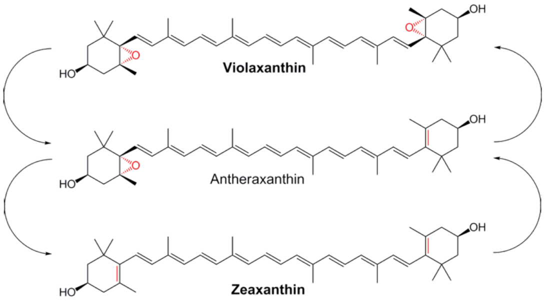

Figure 3.7: Xanthophyll cycle showing reversible conversion from Violaxanthin and Zeaxanthin through the intermediate, Antheraxanthin [adapted from 16, public domain]

LHCI, whilst those predominantly associated to PSII are denoted LHCII. The outer LHCs contain the pigments Chl A, Chl B and xanthophylls — a family of oxygen containing conjugated molecules (Figure 3.7). Conversion between two specific xanthophylls present in the outer LHCs — viz. violaxanthin and zeaxanthin — takes place via depoxidation. In thylakoids, the forward conversion from violaxanthin to zeaxanthin is mediated by the enzyme violaxanthin de-epoxidase, which is present in the thylakoid lumen and is activated at low pH[*]. Proton accumulation in the lumen as a result of strong illumination (§ 3.2.1.1) therefore stimulates conversion of the normally abundant violaxanthin into zeaxanthin [14, 15].

---

[*] The reverse reaction is correspondingly mediated by the enzyme zeaxanthin epoxydase

3.2.1.3 Non-Photochemical Quenching

Excess light absorption can cause saturation of the electron transfer chain of the light dependent reactions, leading to an increase in the Chl excited singlet state population, and thereby increasing the probability of ISC and population of the Chl triplet state. This is significant because triplet Chl is a potent molecular oxygen sensitizer, enabling efficient conversion of the abundant surrounding oxygen from the stable oxygen triplet ground state to highly reactive oxygen singlet responsible for catastrophic photo-damage in biological systems. Photosystem excitation under strong illumination must therefore be carefully regulated by plants.

In PSII, the outer LHCs are only loosely associated to the PS-core and can migrate significant distances. This allows light absorption to be regulated via emigration of some outer LHCs (specifically LHCII 1, 2, 3 and 6), and it is has been shown that this is the principle photo-regulation mechanism in PSII under intense illumination [17–20]. Furthermore, the accumulation of zeaxanthin caused by light stress also has a photo-protective role, with zeaxanthin acting as a singlet oxygen scavenger [21, 22].

In PSI on the other hand, the outer LHCs are tightly bound to the PS-core and the LHC:PS-Core stoichiometry is fixed. Absorption regulation — referred to as non-photochemical quenching (NPQ) — cannot therefore occur via LHCI emigration. For a long time, it was believed that NPQ was not necessary in PSI, as PSI REDOX was thought to be fast enough to mitigate the risk of transfer chain saturation. Recent reports however claim this might not be the case [23–30], and suggest other NPQ mechanisms may be present in PSI. Additionally, the photo-protective role — if any — played by zeaxanthin accumulation in PSI is not yet well understood.

The key aim of this work was therefore to investigate the photo-protective mechanisms present in PSI by monitoring the Chl excited state populations using TPL.

3.2.2 Experimental Results

The photo-protective role of zeaxanthin in PSI was confirmed by measurement of the gradual photo-bleach in reaction centre CW absorption (located at 705 nm) under intense illumination. The PB of both wild-type (WT) — exhibiting standard violaxanthin$\leftrightharpoons$zeaxanthin cycling — and mutant samples engineered to contain zeaxanthin only (NPQ2) was measured in vitro. Both samples showed a marked bleach over time, reaching ∼30 % reduction in absorption after three hours of illumination (Figure 3.8). Significantly, the evolution of the PB was faster in the WT sample, suggesting that the presence of zeaxanthin does indeed infer some degree of photo-protection in PSI.

In order to understand the mechanism behind this photo-protective effect,

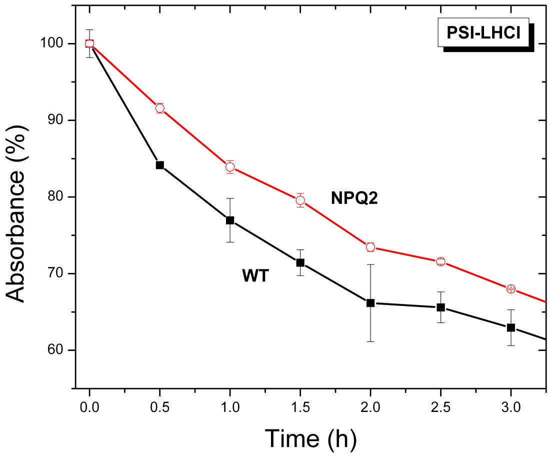

Figure 3.8: Evolution of photosystem I reaction centre CW photo-bleach for wild-type (WT) and zeaxanthin rich mutant (NPQ2) variants as measured in vitro [adapted from 2 courtesy of Dr. M. Ballottari]

TPL measurements were performed on three different subunits of the two sample variants under excitation of the Chl soret band at 440 nm. The investigated subunits were; the entire PSI super-complex (PSI-LHCI), the isolated outer LHCs (LHCI) and the isolated photosystem-core (PSI-core). Given the multitude of emitting chromophores present in the samples, their individual local environments and the complex interplay between them, the resulting TPL maps were highly congested. In order to deconvolve these complex maps, a global fitting procedure was applied to the entire map. In this procedure, prior physical knowledge of the system was used to define the order, N, and relevant decay constant intervals of the multi-exponential fitting curve, $\mathrm{PL}(\lambda, t)$,

$$\mathrm{PL}(\lambda, t) = \sum_{i=1}^{N} A_i(\lambda) e^{-t/\tau_i} \ . \tag{3.3}$$

This was subsequently used to fit the entire TPL map under the assumption that the decay constants were wavelength independent — i.e. $\tau_i \neq \tau_i(\lambda)$. This assumption is typically reasonable, and allows the dimensionality of the fit parameter space to be greatly reduced, resulting in better convergence than fits to individual dynamics [31, Ch. 5]. The resulting multi-exponential amplitudes, $A_i(\lambda)$, were plotted as a function of wavelength, yielding the so called decay associated spectra (DAS) presented in Figure 3.9*.

Inspection of the PSI-core DAS shows that there is very little difference between WT and NPQ2 variants, in agreement with the absence of xanthophyll

---

*It should be noted that the DAS do not necessarily posses a physical meaning, but are simply a convenient way of depicting the result of a multi-dimensional parametric fit. Interpretation therefore requires prior knowledge of the photo-physical system

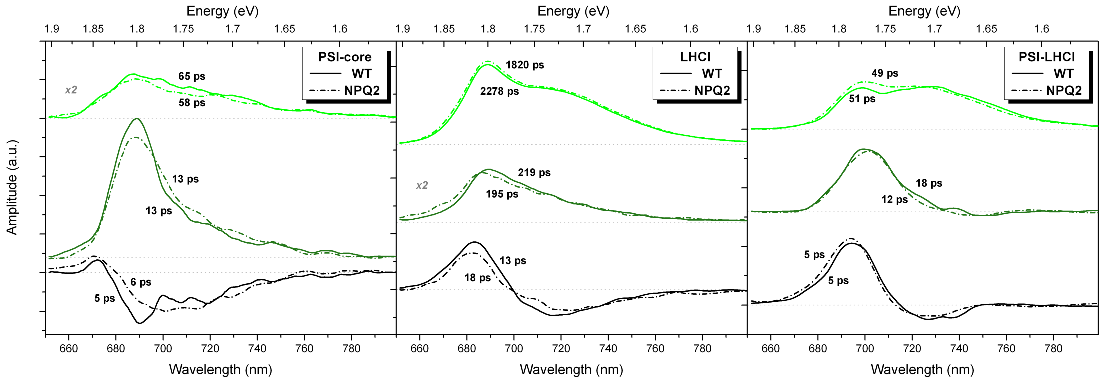

Figure 3.9: *Left panel:* Photosystem I TPL decay associated spectra for the PSI-core sub-unit of both WT (solid line) and NPQ2 (broken line) variants. *Middle panel:* Corresponding TPL DAS for the LHCI sub-unit. *Right panel:* Corresponding TPL DAS for the entire PSI-LHCI super-complex [adapted from 2 in collaboration with Dr. C. D'Andrea & Dr. D. Viola]

binding to the PSI-core. Three different decay components were identified and attributed as shown in Table 3.1.

Whilst minor divergence between the WT and NPQ2 PSI-core DAS is not necessarily surprising, the marked similarity of the outer LHC spectra shown in Figure 3.9 is somewhat less expected due to their differing xanthophyll contents — viz. violaxanthin in WT, zeaxanthin in NPQ2. Three components could once again be identified and assigned as presented in Table 3.1. The slight reduction in the longer two decay times for the NPQ2 variant shows that the presence of zeaxanthin induces mild quenching of outer LHC fluorescence. The attribution of these components to different LHC protein conformations suggests that this quenching may be due to a zeaxanthin induced outer LHC conformational change.

Finally, Figure 3.9 shows that three components were necessary for deconvolution of the entire PSI-LHCI super-complex. The reduction of the second component from 18 ps in WT to 12 ps in the NPQ2 variant suggests that the presence of zeaxanthin acts to dissipate energy in the excited outer LHCs, thereby reducing energy transfer from the outer to the inner LHCs. This is further supported by the observed reduced emission from the outer LHCs in the NPQ2 variant as evidence by the lower amplitude of 725 nm peak in the 51/49 ps spectra.

Taken as a whole, these results serve to show that the photo-protection afforded by zeaxanthin accumulation in PSI is not limited to singlet oxygen scavenging but also plays a role in dissipating energy absorbed in the outer LHCs. Most interestingly, this dissipative effect is relatively weak in the isolated outer LHCs, only becoming significant when the LHCs are bound to the PSI-core. The proposed explanation for this is that zeaxanthin induces a conformational change in the LHC protein structure which yields only mild dissipation at the outer LHCs but significantly affects LHC-core energy transfer.

	Decay constant, τ (ps)		
Sub-unit	WT	NPQ2	Assignment
PSI-Core	5	6	Energetic equilibration amongst inner LHC Chl [32, 33]
	13	13	Emission from inner LHC Chls [32, 34–37]
	65	58	Emission from lowest energy inner LHC Chls [35]
LHCI	13	18	Energetic equilibration amongst outer LHC Chls
	219	195	Outer LHC conformation dependent emission
	2278	1820	Outer LHC conformation dependent emission [38, 39]
PSI-LHCI	5	5	Energetic equilibration amongst all LHC Chls
	18	12	Energy transfer from outer LHCs to inner LHCs
	51	49	Outer LHC emission (predominantly ~725 nm)

Table 3.1: Photosystem I TPL decay associated spectra assignment

3.2.3 Conclusions

The experimental results presented show that Zeaxanthin accumulation in PSI does indeed confer increased photo-protection through the dissipation of excited Chl excess energy. In contrast to PSII — where dissipation occurs directly within the outer LHCs — Zeaxanthin induced NPQ in PSI is only significant when the outer LHCs are connected to the PSI-Core, suggesting a quenching mechanism whereby energy transfer efficiency is reduced. Suggested mechanisms are an induced conformation change of the outer LHCs, an augmented interaction with dissipative low-energy gap Chls, or possibly both.

The work once again highlights the utility of high temporal resolution TPL in the investigation of fast energy transfer processes. These processes play a crucial role in many highly efficient photo-conversion schemes such as photosynthesis, and can only be fully understood through sufficiently resolved dynamics.

Furthermore, the benefits of parallel collection of multiple wavelength channels afforded by the streak camera detection system were also demonstrated, allowing rapid acquisition of high quality TPL maps suitable for global analysis techniques. These multi-dimensional techniques are very powerful tools for unravelling complex systems with convoluted spectral and dynamic evolutions.

3.3 Cation Exchange in Inorganic Nanocrystals

3.3.1 Background

A key semiconductor parameter of great importance to opto-electronic applications is the band-gap — the energetic separation between valence and conduction bands. In bulk materials, the band-gap is an intrinsic material property, being dictated by the lattice symmetry, site elements, etc. Consequentially, tuning the band-gap of a bulk material is challenging and is typically only possible through compositional changes such as doping or stoichiometric variation which can negatively affect material quality.

When material dimensions approach the bulk electron-hole separations (typically a few nm for inorganic semiconductors), quantum confinement can come into play. Such tiny crystals are known as quantum dots or nanocrystals (NCs) and can be fabricated in a variety of different ways including via nucleation and solution growth from metal-organic precursors. The small crystal dimensions act to confine carriers within a three dimensional potential well, resulting in a density of states which is described by discrete Dirac delta functions rather than the continuous form found in bulk.

Quantum confinement in NCs is perhaps best demonstrated by the simple model of a particle in an infinite spherical well. Within such a scheme, the potential, $V(r)$, imposed on a carrier by a spherical NC of radius a, is given by

$$V(r) = \begin{cases} 0 & r < a \\ \infty & r > a \end{cases} . \tag{3.4}$$

For electrons and holes located in the conduction and valence bands respectively, the effective mass approximation can be used to subsume carrier interactions with the lattice into effective masses m_*^c and m_*^v, thereby necessitating further consideration of only the infinite potential well. It can be shown [40] that diagonalisation of the system Hamiltonian, $\hat{H} = \hat{T} + \hat{V}$, results in discrete electron and hole energies, $\varepsilon^c_{n,l}$ and $\varepsilon^v_{n,l}$, given by

$$\varepsilon^c_{n,l} = \frac{\hbar^2 k^2_{n,l}}{2m_*^c} + \varepsilon_g \tag{3.5a}$$

$$\varepsilon^v_{n,l} = -\frac{\hbar^2 k^2_{n,l}}{2m_*^v} , \tag{3.5b}$$

with,

$$k_{n,l} = \frac{\alpha_{n,l}}{a} , \tag{3.5c}$$

where $\alpha_{n,l}$ is the nth zero of the lth-order spherical Bessel function $j_l(k_{n,l}r)$, and ε_g is the band-gap energy.

From this simple model, it can be seen that quantum confinement leads to the discretization of the continuous material dispersion relation exhibited in bulk (Figure 3.10). Most notabley, the energy gap between the highest valence band state and the lowest conduction band state — denoted the effective band-gap — becomes dependent on the NC radius, a. The effective band-gap of a NC can therefore be continuously tuned from the bulk band-gap to higher energies by reduction of the NC dimension. Such control of band-gap energies within a

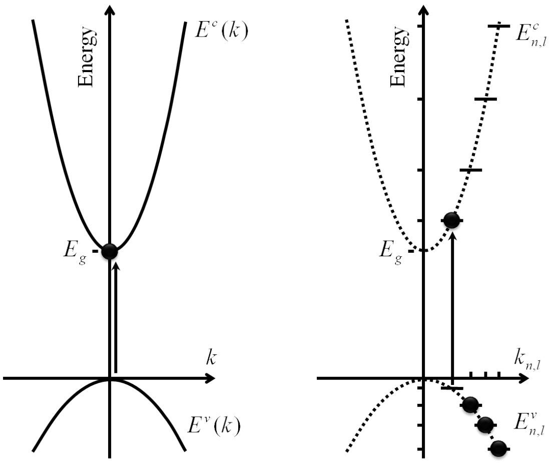

Figure 3.10: *Left panel:* Typical bulk semiconductor dispersion relations, $E(k)$ for conduction and valance bands. *Right panel:* Typical nanocrystal dispersion relations showing discretization due to quantum confinement and the resulting increase in (effective) band-gap energy [adapted from 40, Ch. 2]

single material system is potentially interesting for a variety of opto-electronic applications such as lighting, PV and biological markers.

As mentioned previously, NCs can be fabricated using a variety of different techniques. Regardless of the synthetic route, NC quality is usually defined by good size control, a narrow size distribution, a high PL quantum yield (PLQY) if emissive, and good stability to oxidation. The latter two properties can often be improved by growth of an encapsulating shell of a higher band-gap material, which can be spherical, rod shaped, or multi-limbed depending on growth parameters.

High quality NCs have been grown in a variety of different inorganic material systems including CdSe, CdS, PbSe, PbS, InAs, CuInS to name but a few. Recently, conversion from one NC material system to another has been shown via cation exchange (CE), whereby the cations in a parent NC are fully or partially replaced with an alternative cation in a high temperature reaction [41, 42]. Interestingly, the anion framework does not seem to be significantly affected by the exchange process [41–44], and so CE has opened up an alternative multi-step synthetic route for fabrication of NCs in material systems which have previously proved challenging.

The work presented in this section details two such NC syntheses utilising CE, and the application of TPL to confirm their composition and quality.

In the first, full CE is used as a route to obtaining highly efficient blue-UV emitting NCs in the ZnSe system from CdSe precursors. Whilst high quality direct synthesis has proved difficult, ZnSe based NCs are significantly less toxic than their CdSe counterparts which have accordingly found limited applications despite their extremely high quality. Cation exchange has the potential to unite

Material	Diameter (nm)	Amplitude, A_i (-)		Decay constant, τ_i (ns)		PLQY (-)
		A_1	A_2	τ_1	τ_2	
CdSe/CdS	~ 2.2	1	–	20.2	–	0.34
	~ 5.0	1	–	16.9	–	0.39
ZnSe/ZnS	~ 2.5	1	2.88	0.43	3.04	0.13
	~ 5.0	1	0.82	0.32	3.34	0.14

Table 3.2: Cadmium- and Zinc-based nanocrystal TPL decay parameters

the best of both material systems by projecting the good structural qualities of the CdSe system onto the less toxic ZnSe system.

In the second, the effect of variable Cu vacancy incorporation via partial CE is investigated in the up-and-coming ternary and quaternary Cu-In-S (CIS) and Cu-In-Zn-S (CIZS) NC systems. The heterogeneous nature of these material systems provides a wide parameter space for band-gap tunability, but requires fine control of stoichiometry. Partial CE is presented as tool for stoichiometric tuning and is evaluated using TPL.

3.3.2 Experimental Results

3.3.2.1 Blue-UV-Emitting ZnSe(Dot)/ZnS(Rod) Core/Shell Nanocrystals Prepared from CdSe/CdS Nanocrystals by Sequential Cation Exchange [3]

Zinc selenide/zinc sulphide dot-core/rod-shell NCs with varying core sizes were synthesised via a two step cation exchange reaction from parent CdSe/CdS dot-core/rod-shell NCs via a Cu_2Se/Cu_2S intermediate. The TPL and PLQY of both Cd- and Zn-based NCs was measured to evaluate correct NC composition and quality.

Representative TPL spectra and dynamics of small (~2.2 nm) and large (~5.0 nm) core Cd-based parent NCs under excitation at 2.82 eV are depicted in Figure 3.11. The integrated peak dynamics follow mono-exponential decay forms with lifetimes of 17 ns to 20 ns, in good agreement with previous literature reports for high quality samples of such CdSe/CdS NCs. A NC PLQY of 34 % to 39 % was measured, demonstrating efficient emission and confirming high quality. A radiative decay lifetime of ~50 ns was calculated from PLQY and PL lifetimes, via the relation,

$$\tau = \Phi \tau_R \, , \tag{3.6}$$

where τ and τ_R are the observed and radiative decay lifetimes respectively, and Φ is the PLQY.

The TPL of the corresponding small (~2.5 nm) and large (~5.0 nm) Zn-based NCs obtained from sequential CE of the Cd-based NCs was also measured (Figure 3.11). In contrast to their Cd-based precursors, the peak dynamics displayed

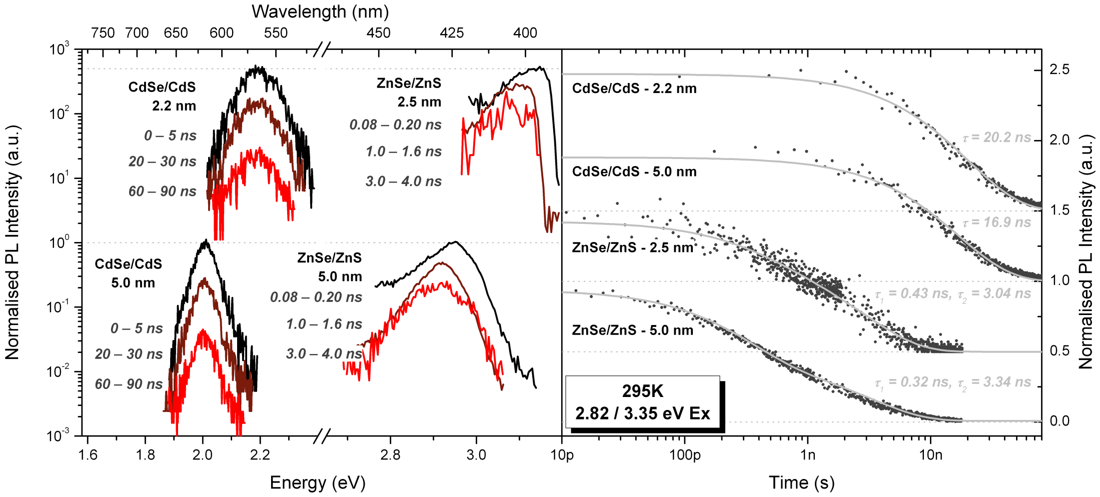

Figure 3.11: *Left panel:* TPL spectra of small and large CdSe/CdS parent NCs (left) and the resulting ZnSe/ZnS offspring (right) obtained via sequential cation exchange. The excitation energies used were 2.82 eV and 3.35 eV respectively. *Right panel:* Corresponding peak TPL dynamics for both NC systems (integrated over the entire emission spectrum shown in left panel). Solid lines are scaled mono-exponential (i.e. $e^{-t/\tau}$) and bi-exponential (i.e. $e^{-t/\tau_2} + e^{-t/\tau_1}$) fits.

a bi-exponential form, with short and long component lifetimes of 0.3 ns to 0.4 ns and 3.0 ns to 3.8 ns respectively (Table 3.2). A PLQY of 12 % to 15 % was also measured for both dimensions. The brevity of the short decay component and its relatively low amplitude suggests attribution to trap related recombination dominated by non-radiative channels. As such, the major contribution to the PLQY was ascribed to the high amplitude long decay component, which was therefore used to calculate a radiative decay lifetime ∼25 ns via relation (3.6).

The short radiative lifetime obtained for the Zn-based NCs is consistent with strong wavefunction confinement within the ZnSe core as predicted by band alignment calculations. The comparatively longer radiative lifetime obtained for the Cd-based NCs would at first sight seem to imply significantly weaker confinement. In inorganic semiconductors however, the wavelength of emission must also be considered when calculating expected radiative lifetimes. It has been shown that the transition dipole moment of many inorganic semiconductors exhibits an inverse quadratic dependence on the energy between initial and final states [45]. Calculation of the expected spontaneous transition rate through application of Fermi's golden rule (§ 2.1.1.3) in the presence of stimulating vacuum fluctuations [46] therefore results in a linear wavelength dependence. Given the emission wavelength of the Cd-based NCs is ∼1.5 times that of the Zn-based NCs, a radiative lifetime ∼1.5 times longer is therefore expected. As such, obtained radiative lifetime value of 50 ns indicates only mild wavefunction delocalisation into the CdS shell.

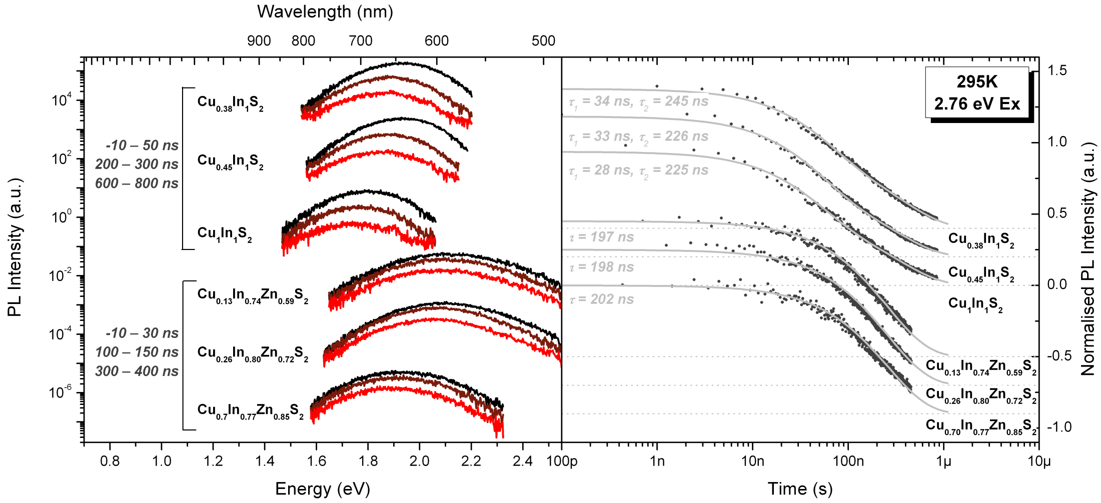

Figure 3.12: *Left panel:* TPL spectra of parent CIS NCs (top) and CIZS offspring (bottom) obtained via partial cation exchange at various levels of Cu vacancy doping. *Right panel:* Corresponding peak TPL dynamics for both NC systems (integrated over the entire emission spectrum shown in left panel). Solid lines are scaled mono-exponential (i.e. $e^{-t/\tau}$) and bi-exponential (i.e. $e^{-t/\tau_2} + e^{-t/\tau_1}$) fits.

3.3.2.2 Strongly Fluorescent Quaternary CuInZnS Nanocrystals Prepared from $Cu_{1-x}InS_2$ Nanocrystals by Partial Cation Exchange [4]

Copper-indium-zinc-sulphide NCs with varying levels of Cu vacancy incorporation were synthesised via partial CE from copper deficient $Cu_{1-x}InS_2$ parent NCs. The TPL and PLQY of both CIS and CIZS NCs was measured to evaluate correct NC composition and quality.

The TPL spectra and peak dynamics of the parent CIS NCs under 2.76 eV excitation are presented in Figure 3.12 for varying levels of Cu vacancy incorporation. A blue-shift of the peak emission wavelength be seen with decreasing Cu stoichiometry (increasing Cu vacancy concentration). The magnitude of this shift is significantly larger that that expected from the small reduction in NC size associated with Cu absence and confirmed via transmission electron microscopy. It has been shown that Cu vacancies act as p-dopants in multivalent chalcogenide systems [47], and so the observed spectral shift is instead ascribed to a Burnstein-Mott shift[*] arising from heavy Cu vacancy p-doping [48]. The PLQY was also seen to have a strong stoichiometric dependence, with decreasing Cu content resulting in higher PLQYs up to an optimum value of 23 % at a stoichiometry of $Cu_{0.38}InS_2$.

The integrated peak PL dynamics were observed to follow a bi-exponential

---

[*] This is when a semiconductor is doped beyond degeneracy so as to push the Fermi level within the electron bands. In this case, heavy p-doping results in relocation of the Fermi level from within the CIS band-gap to within the valence band

		Amplitude, A_i (-)		Decay constant, τ_i (ns)		
Compsition	Diameter (nm)	A_1	A_2	τ_1	τ_2	PLQY (-)
$Cu_{0.38}InS_2$	~ 2.6	1	0.97	34	245	0.23
$Cu_{0.45}InS_2$	~ 2.5	1	1.20	33	226	0.19
$Cu_{1.00}InS_2$	~ 2.9	1	0.93	28	225	0.07
$Cu_{0.13}In_{0.74}Zn_{0.59}S_2$	~ 2.7	1	–	197	–	0.80
$Cu_{0.26}In_{0.80}Zn_{0.72}S_2$	~ 2.6	1	–	198	–	0.68
$Cu_{0.70}In_{0.77}Zn_{0.85}S_2$	~ 2.7	1	–	202	–	0.54

Table 3.3: CIS and CIZS nanocrystal TPL decay parameters

decay form, with a high amplitude long lifetime decay component consistent with previous literature reports for intrinsic emission from CIS NCs. The low amplitude short lifetime component on the other hand suggests attribution to trap related recombination dominated by non-radiative channels. Interestingly, neither PL component exhibits a significant dependence on Cu content despite the strong dependence of the PLQY. This disparity suggests an early branching of excited state populations into partially radiative — i.e. including the short and long components described above — and completely non-radiative decay channels, whose branching ratio is in part dictated by Cu content.

The TPL and PLQY of the corresponding CIZS NCs obtained from partial CE of the CIS precursors was also measured and is presented in Figure 3.12. The PLQY was once again observed to increase with decreasing Cu content, reaching a record value of 80 % at $Cu_{0.13}In_{0.74}Zn_{0.59}S_2$ (Table 3.3). Similarly, the TPL dynamics were seen to be independent of Cu content, but displayed a more prominent mono-exponential form. The marginal reduction in PL decay lifetimes relative to the long CIS component is suggestive of a change in composition and supports successful conversion from a ternary to a quaternary system. The mono-exponential PL decay form is consistent with a reduction of trap related emission attributed to the short decay component in the CIS parents, and is thought to be the cause of the impressive increase in PLQY. It is therefore hypothesised that the Zn incorporation plays a prominent role in trap state passivation, resulting in more efficient intrinsic emission.

3.3.3 Conclusions

The experimental work described in these publications show how cation exchange reactions offer a highly promising new route for synthesis of NCs in material systems which have otherwise proved challenging. The combination of a wide variety of analysis techniques has allowed not only NC composition to be verified but has also shed light on their opto-electronic structure.

Whilst high temporal resolution TPL is often sought in order to understand the dynamics of photo-excited systems, access to long temporal windows can often be lost in this pursuit. For example, the finite length of optical delay lines and their stringent alignment criteria often limit the temporal window of optically resolved TPL schemes such as upconversion. This work demonstrates that flexibility in accessible temporal scales is important, especially for highly efficient emitters such a inorganic semiconductor NCs where long decays dominate.

References

[1] G. Grancini, R. Sai Santosh Kumar, M. Maiuri, J. Fang, W. T. S. Huck, M. J. P. Alcocer, G. Lanzani, G. Cerullo, A. Petrozza, and H. J. Snaith, The Journal of Physical Chemistry Letters **4**, 442 (2013), ISSN 1948-7185, URL `http://pubs.acs.org/doi/abs/10.1021/jz302150q`.

[2] M. Ballottari, M. J. P. Alcocer, C. D'Andrea, D. Viola, T. K. Ahn, A. Petrozza, D. Polli, G. Fleming, G. Cerullo, and R. Bassi, Proceedings of the National Academy of Sciences (submitted) (2014).

[3] H. Li, R. Brescia, R. Krahne, G. Bertoni, M. J. P. Alcocer, C. D'Andrea, F. Scotognella, F. Tassone, M. Zanella, M. De Giorgi, et al., ACS nano **6**, 1637 (2012), ISSN 1936-086X, URL `http://www.ncbi.nlm.nih.gov/pubmed/22283644`.

[4] L. D. Trizio, M. Prato, A. Genovese, A. Casu, M. Povia, R. Simonutti, M. J. P. Alcocer, C. D. Andrea, F. Tassone, and L. Manna, Chemistry of Materials **24**, 2400 (2012), URL `http://dx.doi.org/10.1021/cm301211e`.

[5] G. Yu, J. Gao, J. C. Hummelen, F. Wudl, and A. J. Heeger, Science **270**, 1789 (1995), URL `http://www.sciencemag.org/content/270/5243/1789.abstract`.

[6] G. Dennler, M. C. Scharber, and C. J. Brabec, Advanced Materials **21**, 1323 (2009), ISSN 1521-4095, URL `http://dx.doi.org/10.1002/adma.200801283`.

[7] J. Nelson, *The Physics of Solar Cells*, Series on Properties of Semiconductor Materials (Imperial College Press, 2003), 1st ed., ISBN 9781860943492, URL `http://books.google.it/books?id=s5NN34HLWO8C`.

[8] T. Förster, Discussions of the Faraday Society **27**, 7 (1959).

[9] M. Zavelani-Rossi, G. Cerullo, S. D. Silvestri, L. Gallmann, N. Matuschek, G. Steinmeyer, U. Keller, G. Angelow, V. Scheuer, and T. Tschudi, Opt. Lett. **26**, 1155 (2001), URL `http://ol.osa.org/abstract.cfm?URI=ol-26-15-1155`.

[10] P. H. Raven, R. F. Evert, and S. E. Eichhorn, *Biology of Plants* (W. H. Freeman, 2005), 7th ed., ISBN 0716710072.

[11] K. Song, *Chloroplast (borderless version)-en* (2012), URL `http://commons.wikimedia.org/wiki/File:Chloroplast_(borderless_version)-en.svg`.

[12] Tameeria, *Thylakoid Membrane* (2007), URL `http://en.wikipedia.org/wiki/File:Thylakoid_membrane.png`.

[13] D. S. Goodsell, *Photosystem I* (2014), URL `http://www.rcsb.org/pdb/101/motm.do?momID=22`.

[14] P. Arnoux, T. Morosinotto, G. Saga, R. Bassi, and D. Pignol, Plant Cell **21**, 2034 (2009).

[15] M. Havaux and K. K. Niyogi, Proceedings of the National Academy of Sciences **96**, 8762 (1999).

[16] Yikrazuul, *Violaxanthin Cycle* (2009), URL `http://en.wikipedia.org/wiki/File:Violaxanthin_cycle.png`.

[17] S. Caffarri, R. Kouril, S. Kereïche, E. J. Boekema, and R. Croce, EMBO J **28**, 3052 (2009).

[18] M. Ballottari, L. Dall'Osto, T. Morosinotto, and R. Bassi, J Biol Chem **282**, 8947 (2007).

[19] S. Caffarri, K. Broess, R. Croce, and H. van Amerongen, Biophys J **100**, 2094 (2011).

[20] E. J. Boekema, H. van Roon, F. Calkoen, R. Bassi, and J. P. Dekker, Biochemistry **38**, 2233 (1999).

[21] P. Horton, A. V. Ruban, and M. Wentworth, Philos Trans R Soc Lond B Biol Sci **355**, 1361 (2000).

[22] A. Wehner, S. Storf, P. Jahns, and V. H. Schmid, J Biol Chem **279**, 26823 (2004).

[23] N. Bukhov, S. Govindachary, S. Rajagopal, D. Joly, and R. Carpentier, Planta **218**, 852 (2004), ISSN 0032-0935, URL `http://dx.doi.org/10.1007/s00425-003-1165-6`.

[24] S. Erling Tjus, B. Lindberg Møller, and H. Vibe Scheller, Plant Physiology **116**, 755 (1998), URL `http://www.plantphysiol.org/content/116/2/755.abstract`.

[25] Y. Hui, W. Jie, and R. Carpentier, Photochemistry and Photobiology **72**, 508 (2000), ISSN 1751-1097, URL `http://dx.doi.org/10.1562/0031-8655(2000)0720508DOTPIC2.0.CO2`.

[26] M. Velitchkova, I. Yruela, M. Alfonso, P. J. Alonso, and R. Picorel, Journal of Photochemistry and Photobiology B: Biology **69**, 41 (2003), ISSN 1011-1344, URL `http://www.sciencedirect.com/science/article/pii/S1011134402004049`.

[27] H. Kudoh and K. Sonoike, Planta **215**, 541 (2002), ISSN 0032-0935, URL `http://dx.doi.org/10.1007/s00425-002-0790-9`.

[28] S. Zhang and H. V. Scheller, Plant and Cell Physiology **45**, 1595 (2004), URL `http://pcp.oxfordjournals.org/content/45/11/1595.abstract`.

[29] M.-H. Oh, R. B. Safarova, Y.-J. Eu, I. S. Zulfugarov, J.-H. Kim, H. J. Hwang, C. B. Lee, and C.-H. Lee, Photochemical & Photobiological Sciences **8**, 535 (2009), ISSN 1474-905X, URL `http://dx.doi.org/10.1039/B817808A`.

[30] K. Sonoike, Physiologia Plantarum **142**, 56 (2011), ISSN 1399-3054, URL `http://dx.doi.org/10.1111/j.1399-3054.2010.01437.x`.

[31] J. Amesz and A. J. Hoff, eds., *Biophysical Techniques in Photosynthesis (Advances in Photosynthesis and Respiration)* (Springer, 1996), 1st ed., ISBN 0792336429.

[32] R. Croce and H. Amerongen, Photosynthesis Research **116**, 153 (2013), ISSN 0166-8595, URL `http://dx.doi.org/10.1007/s11120-013-9838-x`.

[33] E. Wientjes, G. T. Oostergetel, S. Jansson, E. J. Boekema, and R. Croce, Journal of Biological Chemistry **284**, 7803 (2009), URL `http://www.jbc.org/content/284/12/7803.abstract`.

[34] R. C. Jennings, G. Zucchelli, and S. Santabarbara, Biochimica et Biophysica Acta (BBA) - Bioenergetics **1827**, 779 (2013), ISSN 0005-2728, URL `http://www.sciencedirect.com/science/article/pii/S0005272813000674`.

[35] E. Wientjes, I. H. M. van Stokkum, H. van Amerongen, and R. Croce, Biophysical Journal **100**, 1372 (2011), ISSN 0006-3495, URL `http://www.sciencedirect.com/science/article/pii/S0006349511001135`.

[36] C. Slavov, M. Ballottari, T. Morosinotto, R. Bassi, and A. R. Holzwarth, Biophysical journal **94**, 3601 (2008), ISSN 1542-0086, URL `http://www.pubmedcentral.nih.gov/articlerender.fcgi?artid=2292393&tool=pmcentrez&rendertype=abstract`.

[37] A. R. Holzwarth, G. Schatz, H. Brock, and E. Bittersmann, *Energy transfer and charge separation kinetics in photosystem I: Part 1: Picosecond transient absorption and fluorescence study of cyanobacterial photosystem I particles* (1993), URL `http://linkinghub.elsevier.com/retrieve/pii/S0006349593815522`.

[38] I. Moya, M. Silvestri, O. Vallon, G. Cinque, and R. Bassi, Biochemistry **40**, 12552 (2001), ISSN 0006-2960, URL `http://dx.doi.org/10.1021/bi010342x`.

[39] T. P. J. Krüger, E. Wientjes, R. Croce, and R. van Grondelle, Proceedings of the National Academy of Sciences (2011), URL `http://www.pnas.org/content/early/2011/07/25/1105411108.abstract`.

[40] V. I. Klimov, ed., *Semiconductor and Metal Nanocrystals: Synthesis and Electronic and Optical Properties (Optical Science and Engineering)* (CRC Press, 2003), 1st ed., ISBN 082474716X.

[41] D. H. Son, S. M. Hughes, Y. Yin, and A. Paul Alivisatos, Science **306**, 1009 (2004), URL `http://www.sciencemag.org/content/306/5698/1009.abstract`.

[42] P. K. Jain, L. Amirav, S. Aloni, and A. P. Alivisatos, Journal of the American Chemical Society **132**, 9997 (2010), ISSN 0002-7863, URL `http://dx.doi.org/10.1021/ja104126u`.

[43] J. Li, T. Zhang, J. Ge, Y. Yin, and W. Zhong, Angewandte Chemie International Edition **48**, 1588 (2009), ISSN 1521-3773, URL `http://dx.doi.org/10.1002/anie.200805710`.

[44] R. D. Robinson, B. Sadtler, D. O. Demchenko, C. K. Erdonmez, L.-W. Wang, and A. P. Alivisatos, Science **317**, 355 (2007), URL `http://www.sciencemag.org/content/317/5836/355.abstract`.

[45] A. F. van Driel, G. Allan, C. Delerue, P. Lodahl, W. L. Vos, and D. Vanmaekelbergh, Physical Review Letters **95**, 236804 (2005), URL `http://link.aps.org/doi/10.1103/PhysRevLett.95.236804`.

[46] A. I. M. Rae, *Quantum Mechanics, Fourth Edition* (Taylor & Francis, 2002), 4th ed., ISBN 0750308397.

[47] S. B. Zhang, S.-H. Wei, A. Zunger, and H. Katayama-Yoshida, Physical Review B **57**, 9642 (1998), URL `http://link.aps.org/doi/10.1103/PhysRevB.57.9642`.

[48] M. Uehara, K. Watanabe, Y. Tajiri, H. Nakamura, and H. Maeda, The Journal of Chemical Physics **129** (2008).

Conclusions

Whilst seemingly diverse in nature at first, it is hoped that the common link between the various investigation presented in this thesis are now clear; the use of transient optical spectroscopy — and in particular transient photoluminescence — to investigate the interactions of various material systems with light. More specifically, all the materials under investigation were to a greater or lesser extent suitable for light harvesting applications, with the possible exception of the highly emissive nanocrystals*. Whilst detailed conclusions are presented in each chapter, a summary of them is now given for convenience.

Design & Development of ps-Resolution Broadband Transient Photoluminescence System

A highly versatile transient photoluminescence system has been constructed with broadband excitation and detection capabilities. Unbroken excitation coverage from 280 nm to 1400 nm was achieved through the use of a tunable commercial Ti:Al_2O_3 oscillator, second and third harmonic systems, and a custom-built frequency doubled optical parametric oscillator. Corresponding unbroken detection coverage from 300 nm to 1400 nm was realised via a dual detector configuration involving streak camera and time correlated single photon counting detection systems. The system was demonstrated to have a maximum temporal resolution of ∼1.9 ps for streak based measurements in the visible spectral region, and a corresponding resolution of ∼100 ps for TCSPC measurements in the NIR spectral region. Flexibility in excitation repetition rate (80 MHz to tens of kHz) was designed into the TPL system so as to allow broad time-scale operation of both detection systems. Whilst not explicitly demonstrated, spatial resolution of TPL down to a few microns can be obtained through via a coupled confocal microscope. Finally, an open source cross-platform software suite (`trpl`) for data visualisation and post-processing in the MATLAB computing environment has been been developed and introduced.

---

* Exploitation of the tunable optical properties of nanocrystals for photovoltaic applications is however a thriving area of research [1–6]

Transient Spectroscopic Investigations of Rubrene Single Crystals

Two related investigations into the less well understood photophysical features of Rubrene single crystal have been presented. In both cases, various specific capabilities of the developed TPL system were exploited to shed new light on existing problems.

An investigation into the origin of a previously observed spurious low-energy PL emission band was presented. This emission was shown to arise from a low-lying state with predictably strong radiative coupling to the ground state yet remarkably weak absorption. Nevertheless, it was shown that aside from population from the higher-lying first singlet state, this low-lying unidentified state could also be populated directly from the ground state. As such previous attributions of this state to transient excited state species such as excimers and self-trapped excitons have been excluded. Unfortunately, no further constructive insight into the true nature of this state was gleaned, although it was hypothesised to arise from a low-density crystalline Rubrene-peroxide layer. Further spatially resolved TPL measurements are planned in order to verify this.

An investigation into the nature of the long-lived photogenerated species observed in Rubrene was subsequently presented. A combination of TA and TPL measurements were used to demonstrate that the long-lived PA band spanning 2.34 eV to 2.45 eV can be attributed to a polaron rather than a triplet exciton population as previously believed. This finding appears to undermine all previous direct spectroscopic observations of triplet excitons in Rubrene crystals, and so calls into question the significance and/or presence of the purported singlet fission and triplet fusion processes in Rubrene single crystals. Given the significance of such a finding, further temperature based transient spectroscopic measurements are planned for confirmation. Furthermore, spin sensitive spectroscopic measurements such as electron paramagnetic resonance spectroscopy could also employed so as to clearly differentiate the two populations.

Broadband Transient Photoluminescence Case Studies

Finally, three case-studies into the various applications of the developed TPL system have been described. These span a disparate set of material systems ranging from organic polymers to inorganic colloidal nanocrystals to photosynthetic biological light harvesting systems.

Firstly, energy transfer processes in a novel ‘dye-doped’ photovoltaic device architecture were investigated through high-temporal resolution TPL. It was shown that the addition of a light harvesting antenna molecule (Spiro-TBT) leads to significantly improved device performance due to broader absorption. Energy absorbed by the antennae was shown to be efficiently transferred to the lower band-gap donor polymer (PCPDTBT) via a non-radiative FRET process.

Secondly, an interdisciplinary investigation into the photo-protection mechanisms regulating photosynthesis in higher plants was presented. Global analysis of bi-dimensional high temporal resolution photoluminescence data allowed a new non-photochemical quenching mechanism in photosystem I to be identified. This mechanism was shown to be mediated by the light-induced accumulation of zeaxanthin. Most interestingly, it was demonstrated that energy dissipation does not occur in the isolated light harvesting photosystem sub-units as expected, but rather only in the complete photosystem super-complex, implying a dissipation mechanism involving a reduction of energy transfer efficiency. This is in marked contrast to the direct outer LHC dissipation mechanisms encountered in the better studied photosystem II counterpart.

Finally, two brief investigations into the promising new cation exchange process for nanocrystal synthesis were presented. In both cases, long time-scale TPL was used as a diagnostic tool to confirm the successful completion of the novel synthetic routes. Full and partial cation exchange schemes were shown to be promising for synthesis of non-toxic and high quality ZnSe/ZnS dot/rod and bare CIZS nanocrystals.

References

[1] R. D. Schaller, J. M. Pietryga, and V. I. Klimov, Nano letters **7**, 3469 (2007), ISSN 1530-6984, URL `http://www.ncbi.nlm.nih.gov/pubmed/17967043`.

[2] S. Taguchi, A. Ueda, T. Tayagaki, K. Matsuda, and Y. Kanemitsu, Physica Status Solidi (C) **738**, 735 (2010), ISSN 18626351, URL `http://doi.wiley.com/10.1002/pssc.200982806`.

[3] J. E. Murphy, M. C. Beard, A. G. Norman, S. P. Ahrenkiel, J. C. Johnson, P. Yu, O. I. Mićić, R. J. Ellingson, and A. J. Nozik, Journal of the American Chemical Society **128**, 3241 (2006), ISSN 0002-7863, URL `http://dx.doi.org/10.1021/ja0574973`.

[4] R. J. Ellingson, M. C. Beard, J. C. Johnson, P. Yu, O. I. Micic, A. J. Nozik, A. Shabaev, and A. L. Efros, Nano letters **5**, 865 (2005), ISSN 1530-6984, URL `http://www.ncbi.nlm.nih.gov/pubmed/15884885`.

[5] W. a. Tisdale, K. J. Williams, B. a. Timp, D. J. Norris, E. S. Aydil, and X.-Y. Zhu, Science **328**, 1543 (2010), ISSN 0036-8075, URL `http://www.sciencemag.org/cgi/doi/10.1126/science.1185509`.

[6] J. J. H. Pijpers, R. Ulbricht, K. J. Tielrooij, A. Osherov, Y. Golan, C. Delerue, G. Allan, and M. Bonn, Nature Physics **5**, 811 (2009), ISSN 1745-2473, URL `http://www.nature.com/doifinder/10.1038/nphys1393`.

Appendix I — Dissemination

Strongly Fluorescent Quaternary CuInZnS Nanocrystals Prepared from $Cu_{1-x}InS_2$ Nanocrystals by Partial Cation Exchange
Luca De Trizio, Mirko Prato, Alessandro Genovese, Alberto Casu, Mauro Povia, Roberto Simonutti, Marcelo J. P. Alcocer, Cosimo DAndrea, Francesco Tassone, Liberato Manna
Chemistry of Materials **24** (12), 2400-2406, DOI:10.1021/cm301211e

Blue-UV-emitting ZnSe (dot)/ZnS (rod) core/shell nanocrystals prepared from CdSe/CdS nanocrystals by sequential cation exchange
Hongbo Li, Rosaria Brescia, Roman Krahne, Giovanni Bertoni, Marcelo J. P. Alcocer, Cosimo DAndrea, Francesco Scotognella, Francesco Tassone, Marco Zanella, Milena De Giorgi, Liberato Manna
ACS Nano **6** (2), 1637-1647, DOI:10.1021/nn204601n

Panchromatic Dye-Doped Polymer Solar Cells: From Femtosecond Energy Relays to Enhanced Photo-Response
Giulia Grancini, R Sai Santosh Kumar, Margherita Maiuri, Junfeng Fang, Wilhelm TS Huck, Marcelo J. P. Alcocer, Guglielmo Lanzani, Giulio Cerullo, Annamaria Petrozza, Henry J Snaith
The Journal of Physical Chemistry Letters **4** (3), 442-447, DOI:10.1021/jz302150q

Electron-Hole Diffusion Lengths Exceeding 1 Micrometer in an Organometal Trihalide Perovskite Absorber
Samuel D Stranks, Giles E Eperon, Giulia Grancini, Christopher Menelaou, Marcelo J. P. Alcocer, Tomas Leijtens, Laura M Herz, Annamaria Petrozza, Henry J Snaith
Science **342** (6156), 341-344, DOI:10.1126/science.1243982

Regulation of Photosystem I Light Harvesting by Zeaxanthin
Matteo Ballottari, Marcelo J. P. Alcocer, Cosimo DAndrea, Daniele Viola, Tae Kyu Ahn, Annamaria Petrozza, Dario Polli, Graham Fleming, Giulio Cerullo and Roberto Bassi
PNAS (*submitted*)

Photo-physics of Rubrene single crystals; from singlet fission to charge generation?

Marcelo J. P. Alcocer, AR Srimath Kandada, Cosimo DAndrea, Daniele Fazzi, Marcello Campione, Adele Sassella, Daniele Brida, Giulio Cerullo, Guglielmo Lanzani, Annamaria Petrozza

Oral Presentation, 11th International Symposium on Functional Pi-Electron Systems (2013)

Photo-physics of Rubrene single crystals; from singlet fission to charge generation?

Marcelo J. P. Alcocer, AR Srimath Kandada, Cosimo DAndrea, Daniele Fazzi, Marcello Campione, Adele Sassella, Daniele Brida, Giulio Cerullo, Guglielmo Lanzani, Annamaria Petrozza

Oral Presentation, 7th International Conference on Materials for Advanced Technologies (2013)

Appendix II — Pulse Parameter Reference

	E_p		
P_{cw}	$\frac{P_{\text{cw}}}{f_{\text{rep}}}$	P_{cw}	
N_p	$\frac{hcN_p}{\lambda}$	$\frac{hcN_p f_{\text{rep}}}{\lambda}$	N_p
$P(t)$	$\int P(t)dt$	$f_{\text{rep}} \int P(t)dt$	$\frac{\lambda}{hc} \int P(t)dt$
$P_{\text{Gauss}}(t) = P_p \, e^{-\left(\frac{2\sqrt{\ln{(2)}}}{t_p}t\right)^2}$	$\sqrt{\frac{\pi}{\ln{(2)}}}\frac{t_p}{2}P_p$	$f_{\text{rep}}\sqrt{\frac{\pi}{\ln{(2)}}}\frac{t_p}{2}P_p$	$\frac{\lambda}{hc}\sqrt{\frac{\pi}{\ln{(2)}}}\frac{t_p}{2}P_p$
$P_{\text{sech}^2}(t) = P_p \, \text{sech}^2\left(\frac{2\ln\left(\sqrt{2}+1\right)t}{t_p}\right)$	$\frac{t_p}{\ln\left(\sqrt{2}+1\right)}P_p$	$f_{\text{rep}}\frac{t_p}{\ln\left(\sqrt{2}+1\right)}P_p$	$\frac{\lambda}{hc}\frac{t_p}{\ln\left(\sqrt{2}+1\right)}P_p$
$P_{\text{square}}(t) = \begin{cases} P_p & , -\frac{t_p}{2} < t < \frac{t_p}{2} \\ 0 & , \text{otherwise} \end{cases}$	$t_p P_p$	$f_{\text{rep}} t_p P_p$	$\frac{\lambda}{hc} t_p P_p$

Table 4: Relationships between various optical pulse parameters. The column label is a function of the row label as indicated by the entry (e.g. $E_p(N_p) = \frac{hcN_p}{\lambda}$). The pulse parameters are; pulse energy, E_p, CW power, P_{cw}, number of photons, N_p, pulse temporal form, $P(t)$. Explicit expression for Gaussian, sech^2 and square pulse forms are given